universität wien

MASTERARBEIT / MASTER'S THESIS

Titel der Masterarbeit / Title of the Master's Thesis

„Upper mantle structure beneath wider Vienna Basin from array analysis of surface waves“

verfasst von / submitted by

Galina Simeonova, BSc

angestrebter akademischer Grad / in partial fulfilment of the requirements for the degree of

Master of Science (MSc)

Wien, 2021 / Vienna 2021

Studienkennzahl lt. Studienblatt / degree programme code as it appears on the student record sheet:	UA 066 680
Studienrichtung lt. Studienblatt / degree programme as it appears on the student record sheet:	Joint-Masterstudium Physics of the Earth (Geophysics)
Betreut von / Supervisor:	Mgr. Petr Kolínský, PhD.

COMENIUS UNIVERSITY IN BRATISLAVA
FACULTY OF MATHEMATICS, PHYSICS AND INFORMATICS

UPPER MANTLE STRUCTURE BENEATH WIDER VIENNA BASIN FROM ARRAY ANALYSIS OF SURFACE WAVES

DIPLOMA THESIS

Study program:	Physics of the Earth
Department:	Department of Astronomy, Physics of the Earth and Meteorology
Supervisor:	Mgr. Petr Kolínský, PhD.

2021 **Galina Simeonova, BSc.**

Comenius University in Bratislava
Faculty of Mathematics, Physics and Informatics

24495023

THESIS ASSIGNMENT

Name and Surname:	Galina Simeonova
Study programme:	Physics of the Earth (Single degree study, magisterský (MSc.) II. deg., full time form)
Field of Study:	Physics
Type of Thesis:	Diploma Thesis
Language of Thesis:	English
Secondary language:	Slovak

Title: Upper mantle structure beneath wider Vienna basin from array analysis of surface waves

Annotation: The AlpArray project is a dense broadband seismic network which allows the study of deep structures using surface wave analysis. The studied area is the wider Vienna Basin which lies in the Alpine–Carpathian–Pannonian junction with major fault systems spanning the region. Using an array approach, we measure phase velocities of surface waves. The approach is a combination of the two-station method with an array beamforming. Using the phase correlation of the two-station method helps with determining the time difference between any two stations in a chosen array. In addition, by the array beamforming method we can obtain the magnitude and direction of the phase-velocity vector. Dispersion curves are then inverted for depth, and shear-wave velocity models are obtained.

Aim: The thesis deals with the analysis of surface waves and measuring their phase velocity dispersion curves using array approach. Inverting the dispersion curves for depth, the aim is to obtain distribution of shear wave velocities in the upper mantle beneath the region of the wider Vienna basin. Potentially, this might lead to resolving geological structures in the region.

Literature:

Novotný, O., 1999: Seismic surface waves, Lecture notes for post-graduate studies , Instituto de F ´ısica, Instituto de Geociˆencias, Salvador, Bahia (textbook)

Kolínský, P., 2010: Surface wave analysis and inversion – application to the Bohemian Massif, PhD thesis, Department of Geophysics, Faculty of Mathematics and Physics, Charles University, Prague (PhD thesis)

Kolínský, P., Valenta, J. and Málek, J., 2014: Velocity model of the Hronov-Poříčí Fault Zone from Rayleigh wave dispersion, Journal of Seismology, 18, 617-635

S Schippkus, D Zigone, G Bokelmann, the AlpArray Working Group, Ambient-noise tomography of the wider Vienna Basin region, Geophysical Journal International , Volume 215, Issue 1, 1 October 2018, Pages 102–117

Petr Kolínský, Götz Bokelmann, the AlpArray Working Group, Arrival angles of teleseismic fundamental mode Rayleigh waves across the AlpArray, Geophysical Journal International, Volume 218, Issue 1, July 2019, Pages 115–144

Kolínský, P., Schneider, F. M., & Bokelmann, G. (2020). Surface wave diffraction pattern recorded on AlpArray: Cameroon volcanic line case study. Journal of Geophysical Research: Solid Earth , 125, e2019JB019102

Comenius University in Bratislava
Faculty of Mathematics, Physics and Informatics

N. Cotte, H. A. Pedersen, M. Campillo, V. Farra, Y. Cansi, Off-great-circle propagation of intermediate-period surface waves observed on a dense array in the French Alps, Geophysical Journal International , Volume 142, Issue 3, September 2000, Pages 825–840

Keywords: Surface waves; phase velocity dispersion curve; array method; beamforming; upper mantle

Supervisor: Dr. Petr Kolínsky
Department: FMFI.KAFZM - Department of Astronomy, Physics of the Earth and Meteorology
Head of department: doc. RNDr. Zdenko Machala, PhD.

Assigned: 25.08.2020

Approved: 16.04.2021 Univ.-Prof. Dr. Götz Bokelmann
Guarantor of Study Programme

.....
Student

.....
Supervisor

Univerzita Komenského v Bratislave
Fakulta matematiky, fyziky a informatiky

ZADANIE ZÁVEREČNEJ PRÁCE

Meno a priezvisko študenta: Galina Simeonova
Študijný program: Physics of the Earth (Jednoodborové štúdium, magisterský (MSc.) II. st., denná forma)
Študijný odbor: fyzika
Typ záverečnej práce: diplomová
Jazyk záverečnej práce: anglický
Sekundárny jazyk: slovenský

Názov: Upper mantle structure beneath wider Vienna basin from array analysis of surface waves
Stavba vrchného plášťa pod širšou viedenskou panvou z array analýzy povrchových vĺn.

Anotácia: Projekt AlpArray je hustá širokospektrálna seizmická sieť, ktorá umožňuje štúdium hlbokých štruktúr s využitím analýzy povrchových vĺn. Študovaná plocha je širšia viedenská panva, ktorá leží na Alpsko-Karpatsko-Panónskom kontakte, v oblasti, kde sa vetvia veľké zlomové systémy. Použitím array prístupu meriame fázové rýchlosti povrchových vĺn. Tento prístup je kombináciou dvojstaničnej metódy a array beamforming (poľa formovania lúča). Použitie fázovej korelácie dvojstaničnej metódy pomáha určiť časový rozdiel medzi ľubovolnými dvoma stanicami vo zvolenom array poli. Použitím array beamforming metódy môžeme navyše získať veľkosť a smer vektora fázovej rýchlosti. Disperzné krivky sa potom transformujú pre hĺbku a získame modely rýchlosti strižných vĺn.

Cieľ: Práca sa zaoberá analýzou povrchových vĺn a meraním disperzných kriviek ich fázových rýchlostí použitím array prístupu. Cieľom je získať rozloženie rýchlosti strižných vĺn vo vrchnom plášti pod oblasťou širšej viedenskej panvy transformovaním disperzných kriviek pre hĺbku. Toto môže potenciálne viesť k objasneniu geologických štruktúr v oblasti.

Literatúra:
Novotný, O., 1999: Seismic surface waves, Lecture notes for post-graduate studies, Instituto de F ´ısica, Instituto de Geociˆencias, Salvador, Bahia (textbook)
Kolínský, P., 2010: Surface wave analysis and inversion – application to the Bohemian Massif, PhD thesis, Department of Geophysics, Faculty of Mathematics and Physics, Charles University, Prague (PhD thesis)
Kolínský, P., Valenta, J. and Málek, J., 2014: Velocity model of the Hronov-Poříčí Fault Zone from Rayleigh wave dispersion, Journal of Seismology, 18, 617-635
S Schippkus, D Zigone, G Bokelmann, the AlpArray Working Group, Ambient-noise tomography of the wider Vienna Basin region, Geophysical Journal International , Volume 215, Issue 1, 1 October 2018, Pages 102–117
Petr Kolínský, Götz Bokelmann, the AlpArray Working Group, Arrival angles of teleseismic fundamental mode Rayleigh waves across the AlpArray, Geophysical Journal International, Volume 218, Issue 1, July 2019, Pages 115–144

Kolínský, P., Schneider, F. M., & Bokelmann, G. (2020). Surface wave diffraction pattern recorded on AlpArray: Cameroon volcanic line case study. Journal of Geophysical Research: Solid Earth , 125, e2019JB019102
N. Cotte, H. A. Pedersen, M. Campillo, V. Farra, Y. Cansi, Off-great-circle propagation of intermediate-period surface waves observed on a dense array in the French Alps, Geophysical Journal International, Volume 142, Issue 3, September 2000, Pages 825–840

Kľúčové slová: Povrchové vlny, disperzná krivka fázových rýchlostí, array metóda, beamforming, vrchný plášť

Vedúci: Dr. Petr Kolínsky
Katedra: FMFI.KAFZM - Katedra astronómie, fyziky Zeme a meteorológie
Vedúci katedry: doc. RNDr. Zdenko Machala, PhD.

Spôsob sprístupnenia elektronickej verzie práce:
bez obmedzenia

Dátum zadania: 25.08.2020

Dátum schválenia: 16.04.2021

Univ.-Prof. Dr. Götz Bokelmann
garant študijného programu

.....
študent

.....
vedúci práce

Abstract

The thesis deals with the analysis of surface waves and measuring their phase velocity dispersion curves using an array approach. The investigated area - the wider Vienna Basin, lies in the Alpine-Carpathian-Pannonian junction in central Europe. Data collected from the AlpArray project was used for conducting the study. The AlpArray Seismic Network was a dense broadband network which allowed for the study of deep structures using surface wave analysis.

An array approach was used for determining the phase velocity dispersion curves of Rayleigh wave fundamental mode. The technique is a combination of the classical two-station method and beamforming. Correlation of the waveforms, as in the two-station method, is used to determine the propagation time of the fundamental mode between pairs of stations in a chosen subarray. By applying a linear regression to the measurements, the absolute value and direction of the slowness vector is obtained. For each subarray, all measured phase velocity dispersion curves are merged. Merged dispersion curves, each corresponding to individual subarray, are then inverted for depth. As a result, 1D shear-velocity model is obtained for each subarray. A compilation of these 1D models provides a quasi 3D model of the upper mantle beneath the studied area. This allows to distinguish the different tectonic units in the region of the wider Vienna Basin. The results are discussed and compared to previous studies carried in the area.

Abstrakt

Práca sa zaoberá analýzou povrchových vĺn a meraním disperzných kriviek ich fázových rýchlostí používajúc array prístup. Skúmané územie – Viedenská kotlina s priľahlým okolím, leží na Alpsko-Karpatsko-Panónskom pomedzí v strednej Európe. V štúdii boli použité dáta zozbierané v rámci projektu AlpArray. Seizmická sieť AlpArray bola hustá širokopásmová sieť, ktorá umožnila štúdiu hĺbkových štruktúr používajúc analýzu povrchových vĺn.

Array prístup bol použitý na určovanie disperzných kriviek fázových rýchlostí základného módu Rayleighových vĺn. Táto technika je kombináciou klasickej dvojstanicovej metódy a metódy beamformingu. Korelácia vĺn, podobne ako v prípade dvojstanicových metód, je použitá na určenie času šírenia základného módu medzi dvojicami staníc vo vybranom subarrayi. Aplikovaním lineárnej regresie na namerané dáta sa získa veľkosť a smer slowness vektora. Pre každý subarray sa zlúčia namerané disperzné krivky fázových rýchlostí. Zlúčené disperzné krivky, každá zodpovedajúca jednému subarrayu, sú potom prevedené na hĺbkové závislosti. Výsledkom sú 1D modely rýchlosti S vĺn pre každý subarray. Spojením týchto 1D modelov vzniká kvázi-3D model vrchného plášťa pod skúmaným územím. Toto umožňuje rozpoznať rozličné tektonické jednotky v širšom regióne Viedenskej kotliny. Výsledky sú prediskutované a porovnané s predchádzajúcimi štúdiami vykonanými v tejto oblasti.

Zusammenfassung

Die Arbeit beschäftigt sich mit der Analyse von Oberflächenwellen und der Messung ihrer Phasengeschwindigkeitsdispersionskurven mit einem Array-Ansatz. Das untersuchte Gebiet - die Wiener-Becken-Gegend, liegt im Übergang zwischen Alpen, Karpaten und Pannonischem Becken in Mitteleuropa. Für die Durchführung der Studie wurden Daten aus dem AlpArray-Projekt verwendet. Das seismische AlpArray-Netzwerk war ein dichtes Breitbandnetz, das die Untersuchung tiefer Strukturen mittels Oberflächenwellenanalyse ermöglichte.

Ein Array-Ansatz wurde verwendet, um die Phasengeschwindigkeitsdispersionskurven der Rayleighwellen-Grundmode zu bestimmen. Die Technik ist eine Kombination aus klassischer Zwei-Stations-Methode und Beamforming. Korrelation von Wellenformen, wird verwendet, wie beim Zwei-Stationen-Verfahren, um die Ausbreitungszeit der Grundmode zwischen Stationspaaren in einem ausgewählten Unterarray zu bestimmen. Durch Anwendung einer linearen Regression auf die Messungen erhält man Absolutwert und Richtung des Langsamkeitsvektors. Für jedes Subarray werden alle gemessenen Phasengeschwindigkeitsdispersionskurven zusammengeführt. Die Dispersionskurven, die jeweils einem einzelnen Subarray entsprechen, werden dann hinsichtlich der Tiefe invertiert. Als Ergebnis ergibt sich ein 1D-Schergeschwindigkeitsmodell für jedes Unterarray. Eine Zusammenstellung dieser 1D-Modelle liefert ein quasi-3D-Modell des oberen Mantels unter dem Untersuchungsgebiet. Dies ermöglicht es, die verschiedenen tektonischen Einheiten in der Region der Wiener-Becken-Gegend zu unterscheiden. Die Ergebnisse werden diskutiert und mit früheren Studien in der Region verglichen.

Contents

Acknowledgments

With special thanks to my supervisor Dr. Petr Kolínský for his guidance and support during this research. Further, I would like to thank the rest of the research team at the Department of Meteorology and Geophysics, Vienna for their collaboration and help. I would also like to acknowledge the members of the AlpArray Seismic project for letting me be a part of the project.
On a personal level, I would like to express my gratitude for my family and friends whose support and encouragement has been invaluable throughout this study. Many thanks to my dear friend who helped me improve my programming skills.

Declaration

I declare that this thesis has been composed solely by myself and that it has not been submitted in any previous application for a degree. Except where states otherwise by reference, the work presented is entirely my own.

Chapter 1

Introduction

Seismic waves are a useful tool for studying the structure of the Earth. Two main types exist - body and surface waves. Body waves propagate through the interior of the planet. Therefore, they provide information about the deep internal structure of the Earth. In addition, body waves can be either P or S waves. P-waves cause compression when traveling thought the body of the planet. They propagate faster, therefore, usually they are the first waves recorded on a seismogram. S-waves are characterized by shear movement of the medium they pass through. This study deals with the second main type of waves - surface waves. I will give a brief overview of theory and research history together with discussing the recent advances in the field. Then I will more focus on the research development in the Alpine area where the investigated region of the study is located.

1.1 Surface waves

Surface waves provide information about the uppermost structure of the planet. In the past they were considered as the "large" waves recorded on a seismogram as their amplitude exceeds multiple times the amplitude of body waves. Surface waves are a result of interfering body waves. To emerge, they require a free surface over which they propagate.

One type of surface waves and the focus of my study - Rayleigh waves, were first predicted by Rayleigh 1885 rather than observed. They propagate along a free surface above a homogeneous halfspace. Rayleigh waves result from interference of compressional P and vertically polarized shear waves. Therefore, on a 3-component earthquake record, they appear on the vertical and radial components. They cause elliptical particle motion and their amplitude decreases with depth. Their velocity is more dependent on the shear waves and is slower in comparison to shear waves.

In 1900, Oldham 1900 observed portion of the "large" waves also on the transverse component of a seismogram which was not predicted by Rayleigh 1885. However, eleven years later, all the pieces were put together by Love 1911. He explained the emergence of the transverse wave motion observed by Oldham by considering layers with different properties (density, wave propagation velocity) overlaying a halfspace. This type of waves are today called after him - Love waves. Love 1911 hypothesized a layer of "crust" which is significantly different from the layer beneath it. Furthermore, he discussed the main property of surface waves - dispersion, for both Rayleigh and Love waves, as well as group and phase velocity. Love waves are a result from constructive interference between horizontally polarized shear waves trapped in a layer. Their amplitude also exponentially decreases with depth. Love waves are not the focus of this study. However, a brief introduction was necessary for completing the theory. Their analysis will be a subject for future studies, see section 6.2.

Dispersion is the main property of Rayleigh waves and is caused by heterogeneity in the vertical direction of Earth's interior. It results, first, in waves having different group and phase velocity. Please note that if surface waves were not dispersive, those two velocities would be equivalent. Second, they are period dependent. The energy, represented by the envelope of

the signal, travels with a group velocity. Phases of wavepackets of different periods move with their own phase velocity. The dependence of wave propagation on period (frequency) is given by the dispersion curve.

Group velocity dispersion curves are said to contain 1-D information about the structure between a source (earthquake) and a receiver (seismic station). On the other hand, phase velocity dispersion curves could provide more localized structural information as they can be measured between two stations. The main tool for analyzing dispersive signals is frequency-time analysis. It is a technique used for representing a signal both in time and in frequency domains.

Most surface wave studies are based on analysis of the fundamental mode. However, higher modes can be used for studying the greater depths of the planet as they penetrate way deeper under the surface. Higher modes propagate faster than the fundamental. Their dispersion curves are also steeper, meaning velocities increase more abruptly with longer periods.

Seismic sources release different amount of energy when an earthquake occurs. Therefore, the period ranges that can be analyzed is highly dependent on the epicentral parameters (magnitude, depth, source mechanics etc). Events recorded at teleseismic distances (thousands of kilometers) make it easier to analyze the fundamental mode of surface waves. This way, body waves have enough time to interfere, higher frequencies are attenuated and the fundamental mode can evolve and get separated from other wavegroups. However, regional earthquakes can also be used. The records might be dominated by high frequency waves, nevertheless, if a proper technique for analysis is used, the dispersion of the Rayleigh waves can be extracted. As noted, frequency-time analysis is the main tool for analyzing dispersive signals. This study is also based on a technique using frequency-time representation of records.

Most methods used for analyzing surface waves assume great-circle propagation. However, for many years arrival angle deviations have been observed when measuring phase velocity dispersion curves. An arrival angle deviation is the difference between the true angle and the geometrical great-circle backazimuth. When plotted on a map those deviations may appear as interference pattern over the region.

The phase velocities are systematically deviated as well. They do not increase monotonically with period, but appear to be wobbled over the whole period range. This is, however, in contradiction with the theory. Modeled dispersion curves which only take the structure into account are always smooth and monotonic.

Studies have shown the interference pattern of arrival angles over different regions (Foster et al. 2014; Pedersen et al. 2015; Kolínský et al. 2019). Kolínský et al. 2020b showed that the diffraction pattern appears after the wavefield has passed a velocity anomaly before it arrived at the station. The measured local phase velocity is not the structural velocity but rather the dynamic. The structural velocity would reflect the velocity distribution below the investigated region. The dynamic velocity includes the complexity of the wavefield which was gathered along the propagation path in addition to the structural. Kolínský et al. 2020a show that the wobbles emerge due to interference of the wavefield after it has been diffracted at a heterogeneity. They model phase velocity dispersion curves and the arrival angle deviations taking into account changes in both the global and regional velocities.

My study revolves around analysis of Rayleigh wave fundamental mode. More precisely, I measure the above described wobbled phase velocity dispersion curves and present a method which highly suppresses these interference effects. The goal is to obtain a smoother dispersion curve which is closer to the structural and easily invertable. The technique is based on simple averaging over many measurements.

1.2 Techniques for surface wave structural studies

In the past, before having dense deployment of seismic networks, surface waves were analyzed using single-station methods. They serve best for group velocity measurements, though phase velocity dispersion curves can also be obtained. However, nowadays, single-station phase velocity measurements are only of historical significance since they cannot fully deduce the properties of surface waves. Hence, they are not that suitable for structural studies. Moreover, there are more precise measurement techniques for two stations or arrays.

Single-station methods were then substituted by two-station methods. They are useful for determining the phase velocity dispersion curves. A wave is recorded on a two-station pair aligned with the earthquake's great-circle path. The waveforms are then correlated and the phase velocity is obtained. However, from two stations the slowness vector cannot be obtained. At least three stations are needed to determine the backazimuth. Two-station methods are highly used together with tomographic studies.

For obtaining not only the phase velocity values but also the direction of propagation, a tripartite method comes in hand. It is a generalization of the two-station method and a predecessor of array measurements. However, the method is not widely used.

An array is a set of stations that have common properties, they record simultaneously in time and the data is then processed together. Arrays may have different geometry, number of stations and aperture according to the purpose of study. In this study, array measurements are used for calculating phase velocity dispersion curves of surface waves.

Beamforming is one of the common techniques how to process the data recorded within an array. The main idea is to find a signal which would explain the measured time records at all stations. The method is based on brute-force attack. Many beams with different slowness vectors are tried (velocity and backazimuth). For each beam the records are shifted in time and summed up. The best solution is the one which produces the most coherent signal.

Beamforming also requires calculating an array transfer function. It estimates the resolution of the slowness-vector components that can be resolved using a particular array design. Maupin 2011 used beamforming of Rayleigh waves to obtain a shear-wave velocity model for southern Norway. The current study, however, is based on another technique, which does not require signal detection. See next chapters for details.

Many studies apply array analysis for studying surface waves. Cotte et al. 2000 used one technique to calculate phase velocity dispersion curves for both Love and Rayleigh waves. Six arrays composed of only three stations were used. They measured the time delays between stations using a moving time window in three frequency bands. The slowness vector was then estimated by linear regression. Pedersen et al. 2003 proposed a similar technique using Wiener filtering with inversion for the slowness vector using L1 norm. The method was then used by Lyu et al. 2017. They used 2 sets of arrays with different aperture (100 and 50km). The dispersion curves were inverted for depth resulting in 1-D models mapping the structure beneath the Western Alps.

Array measurements can be also used to map smaller, local regions. Kolínský et al. 2014 used a single array to obtain 1-D model of a fault zone located in the Bohemian Massif. Their data set included only 7 events recorded at 4 stations. Cotte et al. 2002 inverted phase velocity dispersion curves to obtain 1-D models in the Sorgenfrei-Tornquist Zone in Northern Europe. Their array measurement is similar to the one presented in this study. It is based on cross-correlating signals of different periods between stations. However, they use smaller

array size to better map the three different tectonic zones in the area.

Information about Earth's crust and upper mantle is mostly obtained through surface wave tomographic studies. Tomography is usually used together with a two-station method. Although, one can calculate also group velocity dispersion curves between station and a source.

In case we use phase velocity measurements for the tomography, interstation path velocities are calculated for each station pair and each period. The investigated region is then divided into blocks and phase velocity maps are calculated. The idea is that each block is crossed by (ideally) many rays coming from different directions. This allows to convert the 1-D velocity information into 2-D providing lateral distribution of phase velocities. Finally, an inversion is calculated to determine the shear and possibly also P-wave velocity variation with depth.

In comparison to different array techniques, tomography does not require dense station coverage of the investigated region. It only requires dense ray coverage which is more dependent on the data set rather than station distribution.

Tomography can be used on regional and global scale. However, array methods are a more useful technique to study small regions. Even with arrays of small aperture, phase velocity measurements can be obtained for long wavelengths. While the two-station method used with tomographic studies does not allow for too short interstation distances. Another advantage of array techniques is that they do not need precise epicentral information, meaning origin time and epicentral location. However, the two-station method requires each station pair to be aligned with the great-circle path. Hence, the source location must be known. Moreover, arrays do not require the tomography-inversion step. The phase velocity is directly measured.

1.3 Vienna Basin

The Vienna Basin is one of the most seismic active regions in Austria. It is located in the Alpine-Carpathian-Pannonian (ALCAPA) junction. The region of the "wider" Vienna Basin includes not only the ALCAPA unit, but the Bohemian Massif as well (northwest direction). The main faults are the Mur-Mürz-Line, Salzach-Ennstal-Mariazell-Puchberg Fault (SEMP), the Diendorf Fault, Alpine Front and the Vienna Basin transfer fault system.

Previous studies in the region have investigated the Alpine region and the Vienna Basin extensively (Bokelmann et al. 2013; Behm et al. 2016; Zhao et al. 2016; Hua et al. 2017). Kissling 1993 reviewed various studies using different techniques for mapping the lithosphere beneath the Alpine region. Despite the large number of studies, the only reliable information they extracted was about the crust-mantle boundary (Moho discontinuity) and only under the Western, Central and parts of the Southern Alps. Qorbani et al. 2020 investigated the crustal structure beneath the Southern and Eastern Alps using ambient noise tomography. The seismic anisotropy of the Eastern Alps was a subject of study by Qorbani et al. 2015. Their results point to two anisotropic layers at lithospheric depths beneath the Eastern Alps. The deeper layer they attribute to a detached slab of European origin, where the upper layer is explained by asthenospheric flow above the slab. Lippitsch et al. 2003 image 3 high-velocity anomalies across profiles crossing the Western, Central and Eastern Alps. At depth of 100km in the Central Alps they suggest a subducted European slab. In the Western Alps they attribute the velocity anomaly to detached slab of European origin. However, they suggest that the anomaly in the Eastern Alps is subjected to a subducted Adriatic slab. Kissling et al. 2006 look at different teleseismic tomographic models conducted in the Alpine region and discuss the opposing subduction regimes in the region. Further slab scenarios in the Alpine

region are analyzed by Kästle et al. 2020.

Tomographic studies usually image large regions. In such cases the complexity of the wider Vienna Basin cannot be properly resolved (Piromallo et al. 2003; Kästle et al. 2018; El-Sharkawy et al. 2020; Schivardi et al. 2011).

The more local area around the Vienna Basin is also a subject of studying. Hetényi et al. 2009 took part in the Carpathian Basin Project to study the mantle transition zone using receiver functions in the region around the Pannonian Basin. Szanyi et al. 2013 used ambient noise to study the the Pannonian Basin and it's surroundings. They analyzed group velocity dispersion curves in 6 period ranges and compared the change in absolute values between two periods. They showed that the velocities slightly change between the Eastern Alps and Western Carpathians, whereas in the Pannonian Basin they increase significantly with depth. Schippkus et al. 2018 studied the upper crustal structure in the wider Vienna Basin through ambient noise tomography of Rayleigh waves. In their study the Vienna Basin together with the Little Hungarian Plain appear as low-velocity anomalies while the Bohemian Massif is imaged as a high-velocity structure. Similar results were obtained by Szanyi et al. 2021 who investigated the ALCAPA region using the same approach.

Different anisotropy studies were conducted in the region. Schippkus et al. 2020 studied the stress field and deformation in the wider Vienna Basin. The deformation of the upper mantle in the ALCAPA region was studied by Qorbani et al. 2016 via SK(K)S splitting measurements. Further, SKS measurements were used by Petrescu et al. 2020b and Petrescu et al. 2020a to observe the anisotropy in the upper mantle. The former study focused on eastern and central Europe. In the latter, they extended to the greater Alpine region.

1.4 AlpArray project

AlpArray was a multinational research project aiming to better study the Alps-Apennines-Carpathians-Dinarides orogenic system. The AlpArray Seismic Network was built in the region between 41°N-50°N and 2°E-19°E in central Europe. The precise region was defined as 250 km distance from a smoothed 800 m contour line around the Alps (Hetényi et al. 2018). It was officially running between January 2016 and December 2019. The large-scale seismological network was deployed with contributions from 61 institutions from 17 countries to advance the knowledge of the lithosphere and asthenosphere of the Alps and the neighboring mountain belts. It consisted of over 600 three-component broadband stations - 352 permanent and 276 temporary, including 30 ocean-bottom seismometers deployed in the Ligurian Sea. Figure 1 shows the station distribution of the AlpArray Seismic Network. The mean station spacing was 30-40 km, see Hetényi et al. 2018, which represented a finer spatial distribution than in the case of USArray. The high spatial density and uniform coverage allowed for the application of various seismic techniques to investigate different depth ranges within the Earth - from shallow crust to mantle transition zone. One non-traditional approach would be Soergel et al. 2019 where the authors use ambient noise correlations to extract coda-Q across the AlpArray.

The temporary seismic network was designed to complement existing permanent seismic stations across the AlpArray region. The station installation started as early as mid 2015 and by beginning of 2017 all stations were deployed and operating. Each temporary station had a unique name, composed of 5 characters - starting with an "A" for AlpArray, followed by three digits and ending with an "A". Occasionally, a station's location had to be changed due to high noise levels or some other external factor. In case the site relocation was bigger than

10m, the last "A" was replaced by subsequent letters (B, C etc.).

A seismic station consisted of one (broadband) sensor connected to a digitizer. Generally, various types of sensors with different characteristics were deployed. However, the minimum sampling rate requirement for each sensor was 100 samples per second. Additionally, each station comprised a GPS, a router for telemetry and a battery. Fuchs et al. 2015, 2016 provide additional information about installation and performance of AlpArray Austria. The recorded seismic data together with the sensor's metadata were distributed through the European Integrated Data Archive (EIDA), a service of ORFEUS, and shared with the collaborating AlpArray institutes.

The wider Vienna Basin is located within the AlpArray region between 41°N-50°N and 14°E-19°E (see black rectangle in Figure 1). The region included 44 temporary AlpArray stations and 19 permanent stations of the Austrian Seismic Network, Czech Regional Seismic Network, Hungarian National Seismological Network and the National Network of Seismic Stations of Slovakia. The dense spatial sampling (∼40 km) provided a homogeneous coverage of the area. Most temporary stations in the region were installed as early as mid 2015 and were still operating by the time the study was carried out. This provided a longer recording time than the overall AlpArray temporary deployment and was suitable for conducting the pilot study of the array measurements.

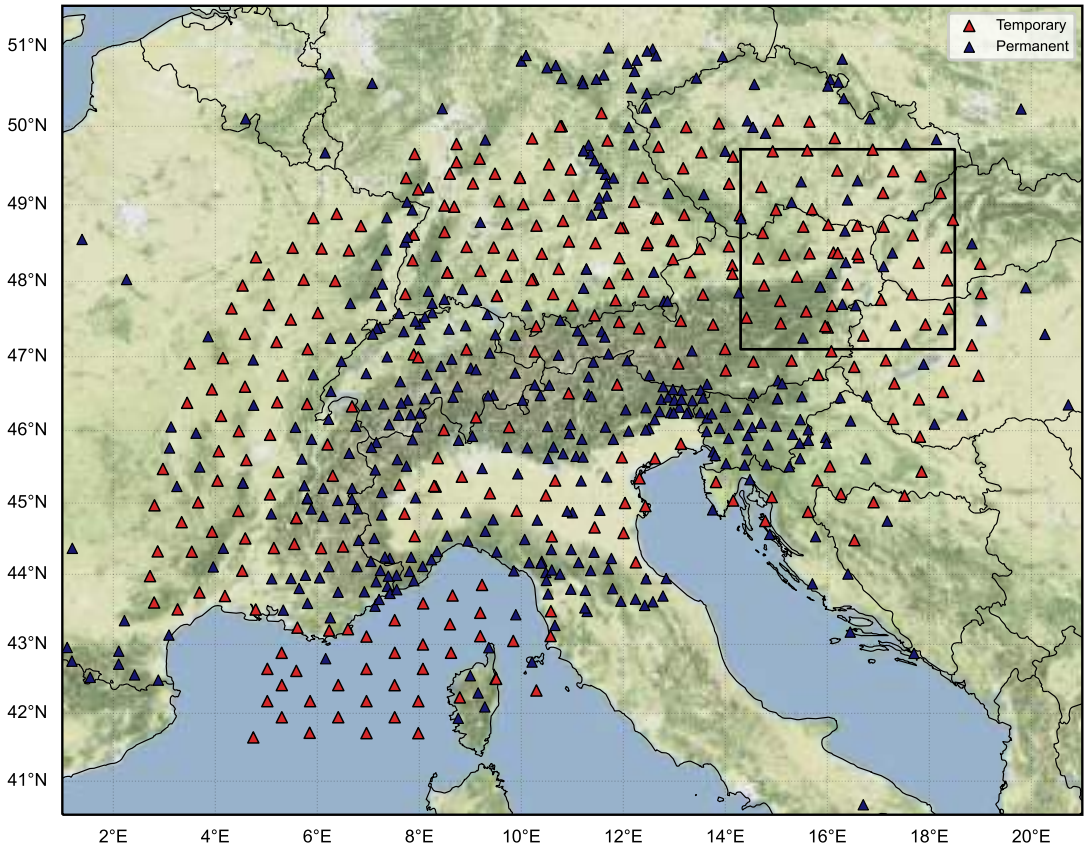

Figure 1. Map of temporary (red triangles) and permanent (blue triangles) seismic stations of the AlpArray network across Europe. Black rectangle shows the approximate location of the wider Vienna Basin (study region).

1.5 My thesis

My work is focused on measuring phase velocity dispersion curves of Rayleigh wave fundamental mode. Though an old technique, the array approach used in my study hasn't been applied in the sense of mapping the lateral distribution of velocities over a local region. I adapted the concept of "floating" subarrays, where each station of my region forms a subarray and a quasi 3-D map of the area is obtained. Furthermore, a technique was developed to investigate whether the wobble effects in the phase velocity dispersion curves could be suppressed. The goal was to test whether upper mantle structures in the wider Vienna Basin could be resolved. In the region several tectonic units meet and while the area has been actively studied by different techniques, it hasn't been investigated by surface waves with such a dense station distribution attempting to reach upper mantle depths.

Chapter 2

Methodology

The following sections provide the individual steps of processing carried throughout the study. At this stage, the stations covering the region of the wider Vienna Basin were already selected. Moreover, the desired set of earthquakes was as well completed. It is important to mention that the quality of the data was checked at each processing step. In case of strange behavior of one station or high complexity of an earthquake, either was removed (see following sections for more details). At first, pre-processing of the raw seismic records was carried out. This is an important step when dealing with surface waves as it helps homogenize the data among different stations. For every earthquake the fundamental mode wavegroup was then extracted at each station. Next, the phase velocity dispersion curves were calculated using an array approach. After processing all earthquakes, a set of phase velocity dispersion curves was obtained per subarray. A merging technique using averaging was then applied, to create one dispersion curve at every subarray. As a final step, each averaged dispersion curve was inverted for depth. This resulted in a set of 1-D shear-wave velocity models mapping the structure below individual subarrays. Together the 1-D models provide a quasi 3-D structural representation beneath the wider Vienna Basin.

2.1 Pre-processing

The procedure of pre-processing started by downloading the metadata for each station from the European Integrated Data Archive (EIDA). Those xml-files provide important information, e.g., station name, respective network code, geographical coordinates, sampling rate etc. Most importantly, they include sensor specifications for each of the 3 channels, namely the poles and zeros of the transfer function. As the station list remained constant throughout the study, this step was executed once. Nevertheless, the metadata files were used when pre-processing each single earthquake.

The earthquake data was collected from EIDA. For each event, characterized by date and time of occurrence, a set of station files was downloaded. Generally, different number of stations was obtained for different earthquakes due to various reasons, e.g., a station was not operating properly at the time the earthquake occurred, the telemetry connection was poor etc. The files format is MiniSEED which is a version of SEED (Standard for the Exchange of Earthquake Data) containing only waveforms. For each day of the year a station data file includes 24-hour record for each of the 3 sensor components - 1 vertical and 2 horizontal.

The 2 steps described above only deal with collecting the station data and metadata. Next, I present the substantial pre-processing done station by station for one individual earthquake. The procedure was then repeated and applied to the full list of events.

First, I needed to pick the correct time window of the earthquake and cut it from the 1-day recordings. Therefore, I roughly estimated the time at which the surface wave group of the particular earthquake would be recorded at the stations in the wider Vienna Basin. For the calculation I needed the approximate epicentral distance (from epicenter to investigated region), the origin-time of the event and some prior knowledge about Rayleigh wave group

velocities. It is known that Rayleigh waves travel at around 3-4 km/s with short periods ($<$ 20s) being slower. However, a bigger velocity window was used - between 2.5 and 6 km/s, which ensured sufficient length of the records necessary for the follow-up processing. Having all of this information, I could calculate the starting minute of the window together with its length in seconds. As the data set included regional-to-teleseismic events from different locations, the time windows varied from earthquake to earthquake. Nevertheless, the procedure of calculation was kept the same.

Once the proper time window was selected and before any further processing was done, the first quality checks were performed. As the study is based on the analysis of Rayleigh waves, technically only the vertical component was relevant. Nevertheless, the checks were applied to the records of all 3 channels. This was done with the intent of expanding the study in the future by analyzing Love waves, see section 6.2. Having the data already prepared would speed-up the overall process.

In case only the horizontals had an issue, e.g., the record was zero or entirely missing, the vertical component was still used and the station was kept for further processing. The amplitudes of the records of each channel were compared to one another. If one was significantly different relative to the other two, the station was marked for further investigation.

Records of all 3 channels were scanned for gaps and overlaps. Not more than 54 gaps with maximum length of 3 seconds in each record were allowed. In case the requirement was not fulfilled the station was dropped. Otherwise, the gaps together with the overlaps were corrected by merging the split ends. Sometimes such gaps happened to be at the beginning or end of the record. Only in case the vertical channel was corrupted by such gaps, the station was rejected. Finally, the records were bandpass-filtered between 1-300 seconds.

Next step of the pre-processing was resampling. Generally, stations could have different sampling rates (at least 100 samples per second). As my study deals with sample-by-sample correlation in a later stage, homogeneity of the data among all stations had to be achieved. Therefore, records at all stations were sampled down to 20sps. By this manner a balance between resolution and computational expenses was achieved.

The final steps were removing the instrument's transfer function and rotating the two horizontal components to radial and transverse (coordinate system of the source). The latter would be crucial only when working with horizontally polarized Love waves. Nevertheless, the rotation was performed to support future studies (section 6.2).

Each instrument is characterized by a transfer function which gives its frequency response. This means that any sensor introduces a frequency dependent amplitude modulation and phase shift to the recorded signal. By removing the response function, the true ground motion is obtained. Correcting the signals was an important step for obtaining reliable results when measuring the phase velocity dispersion curves later, as in general, the stations used were equipped with different sensors.

Finally, the earthquake records were previewed and investigated further. An example of a ready-for-processing event is shown in Figure 2.

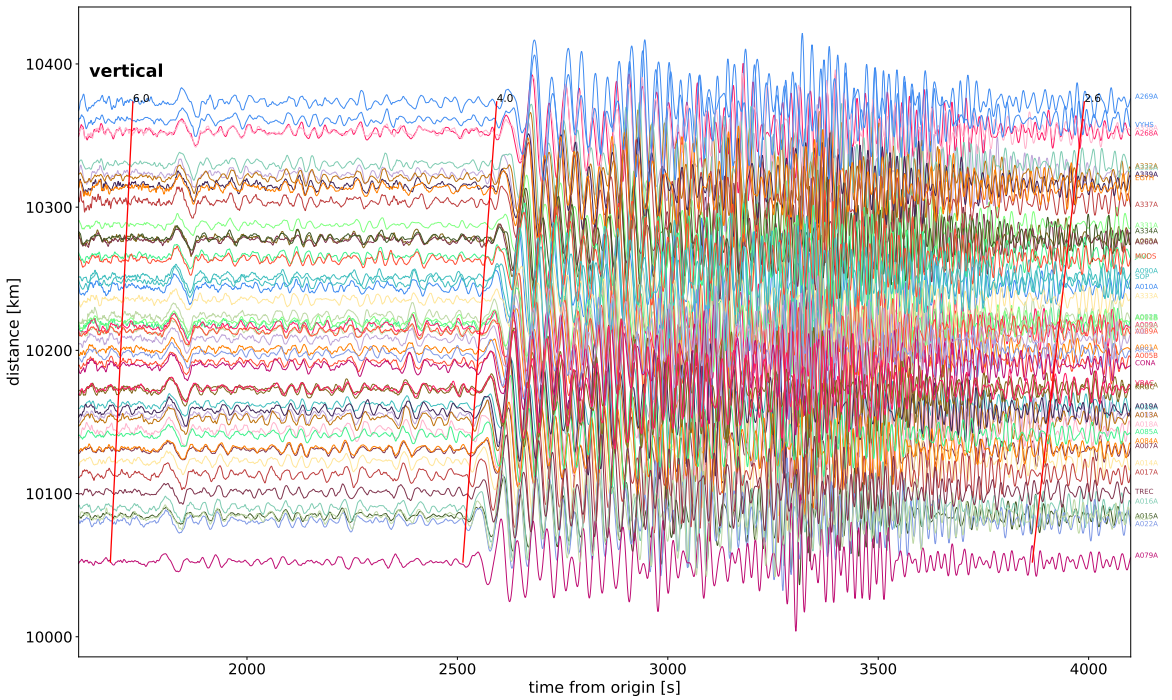

Figure 2. Vertical component of seismic records after pre-processing. Teleseismic earthquake with magnitude 8.2 is displayed. The records are shown with respect to time and distance from origin. The wavegroup of highest amplitude, arriving at velocity of 4 km/s (red line) correspond to the dispersive surface waves.

2.2 Fundamental mode selection

After having all vertical components of an earthquake record at all available stations pre-processed, I could proceed to the next step - selecting the fundamental mode of Rayleigh waves and measuring its group velocity dispersion curve.

Dispersion curves give the relationship of propagation time of a wavegroup of particular period to that period. In order to extract this information from a time record, a technique for analysis in both time and frequency domains simultaneously is necessary. Using frequency-time analysis is a general approach to investigating dispersive surface wave signals. There are different methods using frequency-time representation of a record. My study is based on a "multiple filtering" technique. The method was tested on synthetic seismograms by Kolínský et al. 2011.

Multiple filtering is performed in the frequency domain. Therefore, the Fourier transform (FT) of a time record was first computed. A complex-valued spectrum with both positive and negative frequencies was obtained. Further, the negative frequencies were neglected as they do not provide any additional information. The spectrum could be then filtered. One by one filters with different central frequencies were applied to the positive part of the spectrum. For better visualization, I refer the reader to Figure 3. The 2x4 panel shows the procedure of multiple filtering. On the left, the normalized spectrum of the record is shown by gray line. The 4 plots depict filters with 4 different central frequencies - dashed lines. As a result, a set of spectra was obtained - black solid lines in the figure.

The filters used were of Gaussian shape, each characterized by a central frequency. The maximum number of available filters per earthquake was 150. Their width was not constant but rather changing with frequency - the higher the central frequency, the broader the filter in the frequency domain. In general, the filters were adapted to the properties of each earthquake individually. The number of Gaussian filters used varied from earthquake to earthquake. However, for one event, they were kept the same among all stations. Typically, not more than 80-100 of them were used per event.

It is well known that Gaussian functions provide the best resolution possible in both time and frequency domains when one deals with FT. The frequency-time uncertainty is a general property of the FT. It is a limitation of the resolution which can be obtained in the two domains simultaneously - a well localized time signal, results in a broader spectrum in the frequency domain.

Generally, the prevailing frequency of the spectra did not match the central frequency of the corresponding filter. The reason behind being the application of symmetric Gaussian filters to an asymmetric spectrum. To attain the frequency of each spectra, the instantaneous frequency using the analytical signal was calculated.

After the spectrum has been filtered, the set of spectra could be transferred back to the time domain using the inverse Fourier transform. The dashed gray lines on the right of Figure 3, show the resultant quasi-harmonic time signals corresponding to each spectra. Their envelopes were calculated again using the analytical signal.

Filtering only the positive part of the spectrum, gave the opportunity to use the analytical signal of the quasi-harmonic components corresponding to the fundamental mode. The analytical signal is a complex time signal. If one takes its real part, the original record is obtained. The imaginary part corresponds to its Hilbert transform. It is a convenient tool for calculating the envelope and instantaneous phase/frequency.

Once the harmonic components for each period were retrieved, the group velocity dispersion curve could be calculated. For visualization and better understanding of the procedure see Figure 4. The time signals obtained after filtering are given by dashed gray lines together with their envelopes (solid gray). By selecting the maximum of the envelope at each wavegroup and going along the period range, a smooth curve linking the arrival times - the dispersion curve, can be traced.

The procedure for selecting the proper wavegroup of the fundamental mode was based on a criteria of continuity in time rather than criteria of maximum amplitude. Generally, when looking at shorter periods, Figure 4, one can see that more than one wavegroup is present. Usually, the strongest signal (of highest amplitude) at short periods does not correspond to the fundamental mode but rather to body wave phases or even higher modes. For long periods, however, the fundamental mode carries the most energy. Therefore, the procedure of picking the points on the dispersion curve starts at long periods by selecting the time of the highest amplitude corresponding to the fundamental mode. When proceeding to shorter waves, the local maximum of the new signal is selected in such a way that it is the closest in time to the prior one regardless of its amplitude. Finally, by making use of the relationship between epicentral distance and the arrival time of the wavegroups, the dispersive group velocity was calculated.

At last, the quasi-harmonic signals and their envelopes were truncated to 4 wave-periods around each maximum of the envelope of each filtered wavegroup. This step was performed to assure that the signals contained only the dispersive fundamental mode and no other wavegroups, see short periods in Figure 4. The undesired part of each signal was filled with zeros.

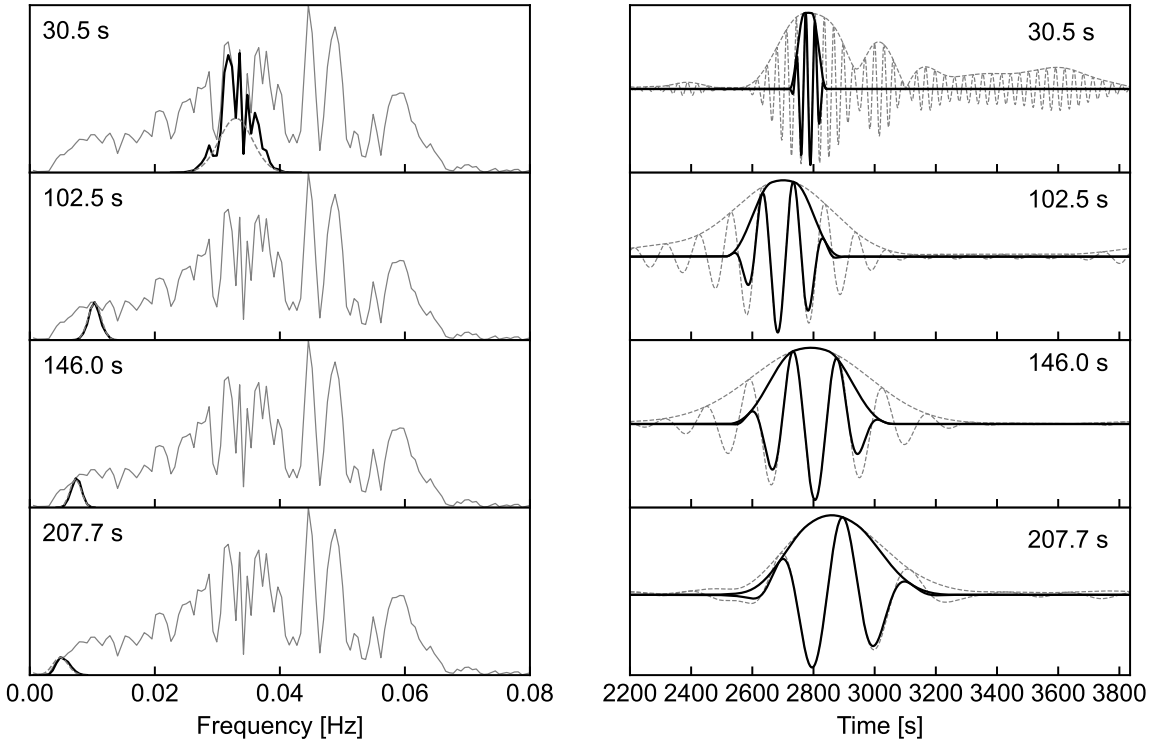

Figure 3. Visualization of multiple filtering technique used in the study. On the left, the procedure of filtering is shown for 4 different periods. The spectrum (gray solid line) is weighted by Gaussian functions with different central frequencies (dashed lines). The width of the filters broadens for higher frequencies. The obtained set of spectra (black solid lines) are then transferred back to the time domain. The right panel shows the quasi-harmonic signals in the time domain (dashed gray lines). The black solid lines depict the truncated signals.

For each period, the amplitude was kept the same for 0.8x the period around the maximum. Going to lower and higher times, the amplitude was smoothed to zero by a cosine window with length of 1.6x the period. The black solid lines in Figure 3 and Figure 4 show the tapered quasi-monochromatic harmonic signals for each period.

Lastly, I would like to briefly discuss the overall process of extracting the proper fundamental mode wavegroup by using the SVAL software. For each earthquake, one station record (Z component) was processed manually, at first. The time window, period range and filtration parameters were adjusted, then all other stations were processed automatically. Figure 2 was of great help when selecting the time window for each event as it visually shows the times of the surface wavegroup.

The time window was always picked longer than necessary and the record edges were smoothed out to avoid artifacts when computing the FT. The analyzed period range also differed from event to event as it depends on epicentral parameters. For controlling the width of the filters, a parameter linearly dependent on the central period, was used. As already mentioned not more than 100 out of 150 filters were necessary for filtering one earthquake. When processing the same event, they were kept the same among stations, more precisely, their shape and central periods. However, they differed from earthquake to earthquake.

Once the proper parameters were found for the station, all other station records were

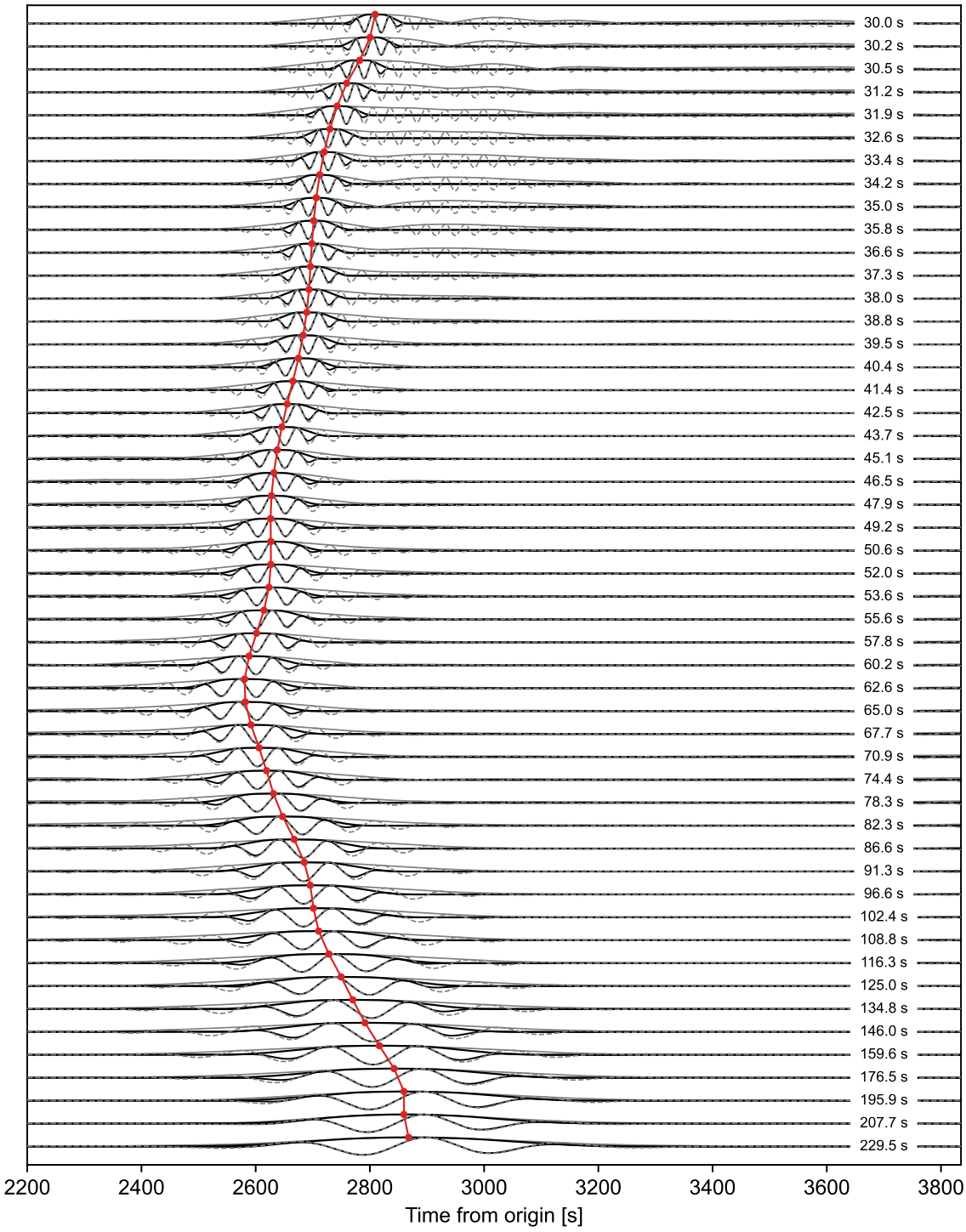

Figure 4. Procedure of calculating the group velocity dispersion curve of the fundamental mode. The set of quasi-harmonic components of different periods obtained after filtration is shown by gray dashed lines. Envelopes drawn by gray solid line. By picking the maximum of the envelope (red dots) of each wavegroup and going along the period range, a smooth curve can be drawn - the dispersion curve, depicted by red solid line. Black lines depict the truncated quasi-harmonic components and their envelopes.

processed automatically. In some cases, re-adjustments were necessary, usually it was the filtration parameter. The stations, for which the fundamental mode was not selected correctly, were then checked manually. Parameters were reset accordingly and all stations were processed again together. The procedure went on until the proper waveforms of the fundamental mode were extracted from all station records. Of course, sometimes records were noisy and biasing the measurement. In some cases, only one station was removed, in other the event was disregarded completely.

One final remark to be made is that the group velocity dispersion curves of the fundamental mode were not used for further processing. In the next step - measuring the phase velocity dispersion curves, only the quasi-monochromatic harmonic components were necessary.

2.3 Phase velocity measurement

The phase velocity measurement was based on an array approach described and used by Kolínský et al. 2014. It combines cross-correlations of previously obtained quasi-monochromatic signals and linear regression for obtaining the slowness vector.

A seismic array is a set of stations with common properties that record signals simultaneously in time and the data is then processed together. The stations comprising the array are generally in a close geographical proximity. A dense seismic network like AlpArray allows to adapt the idea of "floating" subarrays over a region of investigation (Kolínský et al. 2019). In an area densely covered by seismic stations, any station can become a central of an array. By moving over the whole region, many subarrays are formed if, of course, they satisfy some initially implied criteria. See below for details.

In the study, each subarray was characterized by a central station. Neighboring stations were searched for in a radius of 80 km from the central. Additionally, stations closer than 20 km were dropped. The aperture was therefore 160 km in diameter. A central station formed an array only if it found at least 5 neighbors. Therefore, the minimum array size was 6. Some stations at the edges of the investigated region did not fulfill the criteria mentioned above and never formed an array.

The first part of the phase velocity measurement was signal cross-correlation between a subarray central station and each of its neighbors. For the calculation the truncated fundamental mode components were used. Cross-correlation was computed for each station pair and for each period.

The main idea was to obtain time differences between stations in a subarray corresponding to the phase propagation from station to station. At first, let's consider a wave with period of 70s arriving at two stations only. For better understanding, I refer the reader to Figure 5. The black waveform corresponds to the central station of the array. The red, which arrived later in time at its station, was shifted sample by sample with respect to the black and correlation was computed at each step. The correlation window was 35s in both positive and negative time direction. The maximum correlation shown on the right of Figure 5, corresponds to shift in time by 10.5s. This means that 10.5s after the 70s wave was recorded at the central station, it hit its neighbor. Therefore, the time shift is positive with respect to the central. Afterwards, another neighboring station was selected and the procedure was repeated. A set of time differences with respect to the central station were obtained. Those represent the propagation time of the phase of particular period within the array.

As the correlation window is 35 seconds, potentially issues with cycle skipping might

appear when waves of shorter periods are correlated. In such case, more than one correlation maximum might appear. To avoid wrong calculations, a procedure of continuity in time is applied. The idea is very similar to what was discussed in the previous section when selecting the correct wavegroup corresponding to the fundamental mode. The time delays between station-pairs are calculated starting at long periods going towards shorter period by period. In case of two correlation maximums there will be 2 time delay measurements. The one closer in time to the previous wavegroup is then selected.

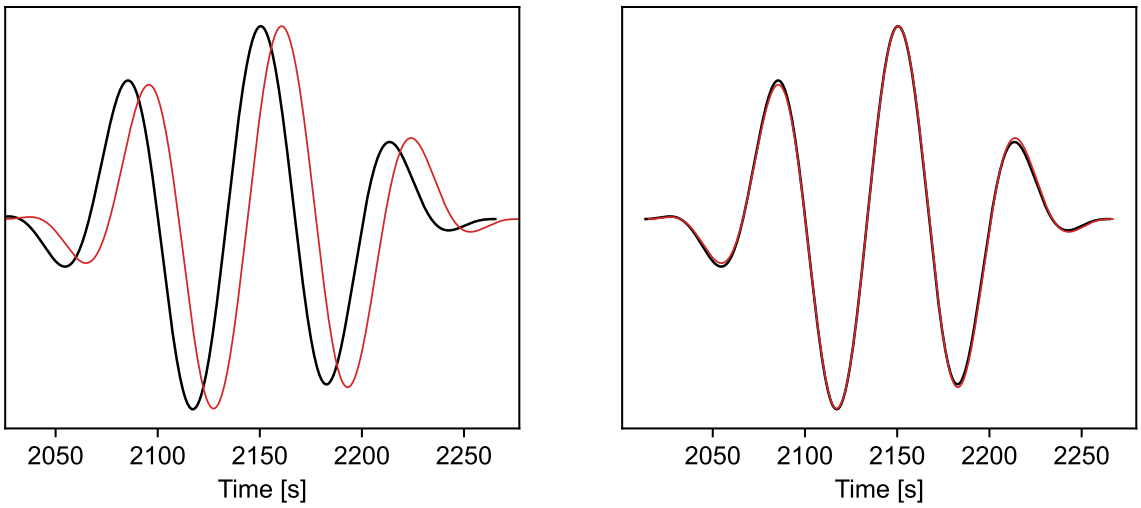

Figure 5. Cross-correlation procedure showed for 2 stations in a subarray. Black line represents a 70 s quasi-harmonic component. The red waveform was shifted sample by sample and correlation was computed at each step. The right panel only demonstrated the maximum correlation for a shift of the red component by 10.5 s "back in time".

Now, the slowness vector could be calculated. The procedure is based on linear regression. For better understanding the method, I refer the reader to Figure 6. The figure shows the results obtained for a 70s wave coming from an earthquake close to Kamchatka. A008A is the central station of the array and it has 14 neighbors. Important to notice is that the coordinate system is centered at A008A. On the horizontal plane, the subarray design is presented in Cartesian coordinates marking the distance relative to A008A. On the vertical, the corresponding time differences are shown.

A plane wave is fitted through those time measurements, see left on Figure 6, and the slowness-vector components were obtained. On the right, the figure shows a view along the regression plane. The x and y-components of the slowness vector were calculated from the slope of the intersection of the x-time plane and y-time plane, respectively. The yellow and red lines in the figure represent exactly those. The directional component of the slowness vector, the arrival angle, was determined by taking the $\arctan(s_y/s_x)$ - magenta line.

The true arrival angle was calculated to be 16.4° measured from North (geometrical great-circle backazimuth is 21.8° from North). By using the inverse relation between slowness and velocity, the absolute value of the velocity could be calculated.

Next, the procedure was performed for the whole period range and a phase velocity dispersion curve was obtained for the central station A008A.

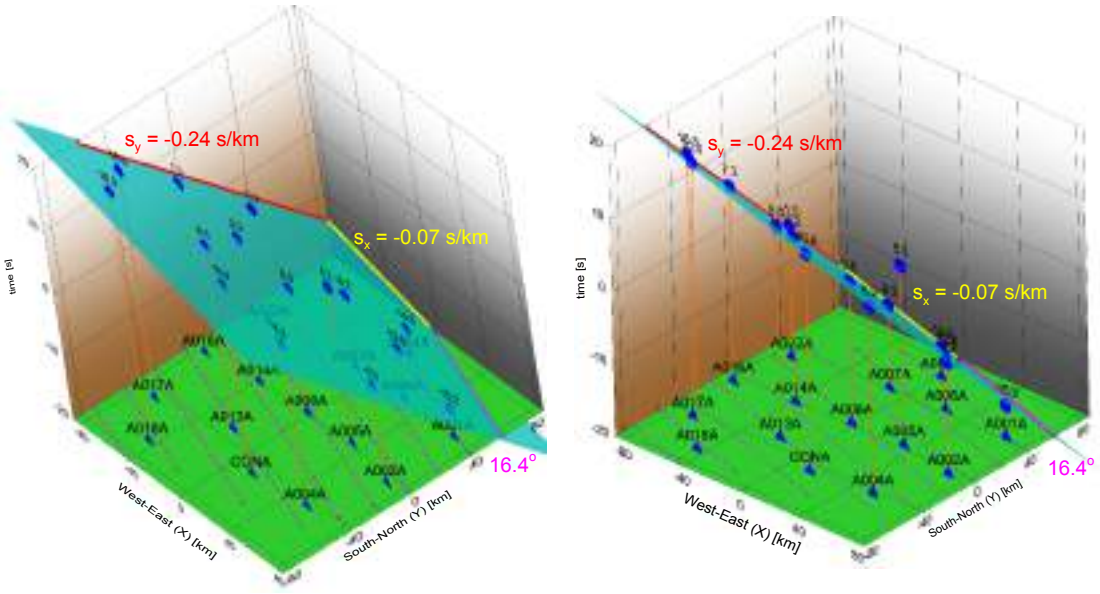

Figure 6. Procedure of obtaining the slowness-vector components by linear regression from one subarray. The central station of the subarray is A008A and it has 14 neighboring stations. The example shows a 70s wave propagating from the Kamchatka earthquake along the subarray. The vertical time-axis displays the time differences between central and any other station calculated by cross-correlation. The horizontal plane is given in Cartesian coordinates, mapping the station distribution. The origin of the coordinate system is centered at A008A. A plane wave is fitted to the time measurements and the slowness vector is obtained.

Theoretically, the phase velocity dispersion curve should contain 1-D information beneath the array. However, from one earthquake, still the dynamic velocity is measured; it is not possible to obtain the structural velocity as the dispersion curve is still very wobbled, see Kolínský et al. 2020a. On the other hand, combining more earthquakes at each subarray can significantly reduce the wobble effects. See next sections for details.

At last, the phase velocity dispersion curves for all other subarrays were calculated. Therefore, for one event, a set of dispersion curves mapping the region was obtained.

Together with the slowness vector, time residuals for each period and station were calculated - the difference between the measured time and the one predicted by the linear regression. They helped to evaluate the quality of the fitted data. Each neighboring station in one subarray for each period was characterized by a residuum. Therefore, many other residuals could be calculated. For example, if averaging the residuals over all neighboring stations at one period, a new value was obtained evaluating the overall performance at that particular period. On the other hand, one could average over the whole period range at one neighboring station and get a sense of how well the station performed.

For this study, I mostly took advantage of the second scenario. Looking at individual stations in one subarray, helped me further identify poor data quality. For example, if one looks on the right of Figure 6, it is visible that station A005A is an outlier and it will produce high residuals. This points to the phase of the waveforms at this station being distorted. The cross-correlation did not give correct results. Station A005A was then disregarded from the final calculation. Please note that by removing one station and running the calculation again,

the components of the slowness vector change and point to more accurate results.

2.4 Merging

As mentioned in the previous section, the measured phase velocity dispersion curves include information about the dynamic velocity of the incoming wavefield together with the structural velocity beneath the station they correspond to. This affects the results obtained by inversion as they would not fully reflect the structure beneath each station. Therefore, in attempt to reduce the effect of the wobbles, phase velocity dispersion curves from different locations were merged together.

For all stations that were central of a subarray, I obtained one averaged dispersion curve. The phase velocity dispersion curves were generally processed in different period ranges with the overall range spanning periods from 11s to 238s. Additionally, due to different data availability, the number of dispersion curves obtained for each station differs. The merging procedure was based on simple weighted average of all measurements over a period range for each station individually. Please note that the procedure was executed period by period.

Let's consider all measured phase velocity dispersion curves obtained only for one station and go through the merging procedure. 3 parameters were used to build the constrains for merging - cut-off derivative, minimum number of events and cut-off angle. Their values were not fixed, but could be altered.

Due to wrong measurements, some dispersion curves had high velocity jumps at the short and long period ends. To restrict the potential bias when averaging, the "smoothness" of each curve was first evaluated. The calculation started at in the middle of the period range. Moving period by period to both ends of the curve, the velocity derivative with respect to the period is calculated. In case the difference in velocity between two consecutive periods exceeded the preset cut-off derivative value, the rest of the period range was not used starting with the point which created the high jump.

Additionally, the number of measurements at each period were checked, meaning, how many velocity measurements were available at this period. Merging could be performed only if at every period this number exceeded the preset minimum number of events. The two parameters restricted the overall period range of the merged curve. Generally, not many earthquakes were processed at very short or very long periods. However, the middle range of periods was well covered.

The procedure of merging was based on averaging over all measurement points at each period separately. To each velocity value, a weight was assigned. Here the cut-off angle parameter played it's important role. Generally, a high velocity wobble, would produce a high arrival angle deviation in absolute value. Therefore, the relation was used to smooth out the curves while merging. For each velocity measurement at a particular period, the value of the corresponding arrival angle deviation was checked. In case it's value was not in the range of $\pm$ the preset cut-off angle, the measurement was not taken into account when merging. Otherwise, a weight was assigned to it.

Generally, the weight decreased linearly the higher the value of the arrival angle deviation. That is for an angle deviation value of 0°, the weight assigned to the velocity measurement was maximum 1. From 0° to the cut-off angle, the weight was reduced. Please note that the arrival angle deviation could be negative. Therefore, when assigning the weights, the absolute value of the angle was taken.

Additionally, at each period the weighted standard deviation was estimated. The error calculation helped by providing a range of uncertainty. Finally, one phase velocity dispersion curve was obtained for the subarray. The procedure was repeated for all subarrays available. A set of smoother phase velocity dispersion curves was obtained, each corresponding to a subarray. This way a quasi 3-D phase velocity model of the region under investigation was obtained. The curves together with their uncertainties were then set for inversion.

At this stage, the last data quality checks were performed. The individual phase velocity dispersion curves corresponding to each subarray together with its merged curve were previewed. It was noticed that some of the measured dispersion curves were shifted either to too high or too low velocities. They did not match the overall behavior of the rest of the measurements. Thus, they were manually removed. I would like to point out that not more than 5 curves were removed considering all phase velocity dispersion curves on all subarrays. This represents fraction of a percent of the total amount of data. Thus, no bias was introduced after the elimination. See next chapter for data statistics.

2.5 Inversion for depth

For the inversion of the phase velocity dispersion curves at each subarray two procedures were used. The inverse problem was solved by the isometric method (Málek et al. 2007) and the forward - by the modified Thomson-Haskell matrix method (Proskuryakova et al. 1981). The inversion procedure has been tested on synthetics by Kolínský et al. 2011. Moreover, it has recently been used by Belinić et al. 2021. In fact, the same scheme was used here, but the number of runs was increased.

Dispersion curves were computed for a 1-D layered model above a halfspace. Each layer together with the halfspace had the following parameters - v_s, v_p/v_s ratio and density.

Depths up to 410 km were stratified by 25 layers. This depth is known as the beginning of the upper mantle transition zone. The space beneath was considered as halfspace. The number of layers as well as their thickness was kept constant. However, with depth the relative thickness of each layer gradually increased. This was done to reflect the decrease in resolution capability of surface waves with depth.

Rayleigh waves are predominantly dependent on shear-wave velocities. Therefore, only v_s velocities were searched for. The v_p/v_s ratio together with the density at each layer was set by the ak135 density model. Shear-wave velocities were inverted for the halfspace as well. The procedure was kept the same as in each layer.

By setting a reasonable starting model, computational time could be saved. The phase velocity dispersion curves over all subarrays were first averaged. One mean curve for the whole region was obtained. By inverting it, a starting model was determined. However, the inversion does not depend on it. The only reason for conducting this step was to obtain a model which is only closer to the final one.

The phase velocity dispersion curves at each station were inverted 100 times. Additionally, each run consisted of several thousand of iterations. A single iteration performed the following - a new model was set, a dispersion curve was computed and a misfit was calculated. The misfit function gave the distance between the modeled and measured dispersion curves. The inversion method is based on keeping this distance minimal at each iteration. However, one dispersion curve can be obtained by many models with slightly varying misfit.

At each iteration, a structural model was computed by adding random perturbations to

the previous one. However, the misfit function of the modeled dispersion curve corresponding to the new method was always compared to the previous misfits. At each iteration, it was checked whether the new dispersion curve was an improvement compared to the previous, in a misfit sense. The method always tries to systematically go to better fits.

The standard deviations of the merged phase velocity dispersion curves were also taken into account. They constrained the range in which the modeled dispersion curves could deviate from the merged. This means that if the merged dispersion curve has high errors in some period range, the modeled curves will also span a larger range of velocities.

Each model was characterized not only by a misfit, but additionally by a complexity too. The complexity gives the average of absolute values of all velocity steps between layers and is normalized by the total number of layers. In other words, it tracks how smooth the overall velocity distribution is. In this study, the product of the two is used, see next chapters.

The final model was calculated as an average of the 100 individual models, therefore, its standard deviation could also be determined. Generally, the final model might not have the lowest misfit. However, the complexity parameter was usually the smallest.

2.6 Software

Different type of software were used throughout the study, see Table 1 for a full list. The first four - downloading and exporting scripts, DistAz.exe and ChramRot.exe, were used for the initial pre-processing of the data. The latter programs were used to connect the earthquake location and origin time with the data recorded at the stations in the region. When seismic stations record earthquakes or any seismic vibrations, they do not reflect any information about the source. Therefore, it is necessary to calculate the distance and time between the source and the stations. Once the pre-processing was finished, the records were visualized by the "visual inspection" script.

The main processing was carried out by SVAL - frequency-time analysis, ArrayCorr - phase velocity measurement and MerPha - merging all measured phase velocity dispersion curves at each subarray. Different plotting scripts were developed for previewed the data. They served as additional quality check of the calculations. Once the quality was verified, the inversion for depth could be carried out. Again SVAL performed the long and heavy job of inversion. Finally, the results, which are discussed later in the thesis, were plotted and interpreted.

Furthermore, new functions were added or the already existing ones were modified to better match the purpose of the study. For example, as the work is based on Rayleigh waves, the exporting script was modified to keep the vertical components of records even in case any of the horizontals had an issue. Therefore, the volume of the data increased even not significantly.

However, most corrections and adaptations were done to the merging software. Different ideas were tested before implementing the 3 new final constraining parameters (cut-off derivative, minimum number of events and cut-off angle). It was an iterative process - investigating at each step whether the function performed correctly or if it at all made physical sense. While working with each software, many files were output allowing to keep track of the measurements at each point of processing.

The programs SVAL and ArrayCorr have a graphical, interactive component, see Figure 7 and Figure 8. Figure 7 shows three windows of the SVAL software. On the left, a small colorful window is to be seen. This is the starting window of the program. One needs to select

the type of file that stores the pre-processed records. In case of three-component records, one needs to specify which component is to be used. The maximum number of samples is also adjusted. This step is performed mainly to allocate the necessary memory in the computer.

In Figure 7 the window on the left shows the main window in SVAL. On the left, the adjustable parameters are to be seen. The length of the window in seconds from the origin needs to be selected together with period range and alpha parameter.

On the right, there are two panels. On the lower one is the raw time record. Above it, the filtered 70s quasi-monochromatic component of the fundamental mode can be seen. By red the truncated envelope is plotted. In fact, any filtered signal can be selected and previewed. On the lower left panel, is the group velocity dispersion curve in the period range 15-240s.

SVAL is used not only for selecting the fundamental mode of Rayleigh waves, but also performs the shear-wave velocity inversion for depth. The inactive window on the right plots the P, S and density models while the inversion runs. The parameters for the inversion can be set using the blue panel. Below it one can find a window which provides text information about the process of calculation in both frequency-time analysis and inversion mode.

Finally, the third window on the low left corner is the spectral domain window. It is used to observe the record in the frequency domain. The spectrum is depicted by yellow. Additionally, each Gaussian filter together with its spectra can be plotted.

The second screenshot, Figure 8, presents the GUI of ArrayCorr. The blue panel on the left displays all parameters. The period range needs to be selected again. Sometimes the fundamental mode was processed in one period range, but it was shortened for ArrayCorr. The time window of the correlation needs to be selected. Additionally, the array design constrains can be altered - the minimum and maximum distance (subarray aperture), the minimum number of neighboring stations.

The central panel, shows a Cartesian map of the array with central station CONA. the arrival angle for each period is plotted by color. On the left of this panel, is a "information board". While the measurement is running, the program prints different information. This is very useful for tracking the progress of the calculation. The final measured phase velocity dispersion curve in the period range 30-230s is plotted by red on the panel below.

Finally, on the right, one can see the quasi-monochromatic signals as each period displayed together for all stations. Those are the signals that are then shifted samples by samples with respect to the central station to obtain the time differences.

As one can observe, many parameters can be altered. The processing at each step is visualized when using any of the software, which gives confidence and control over the analysis.

Finally, I would like to emphasize that all scripts used for plotting the results were prepared specifically for the thesis. However, their purpose was not only to preview the obtained data, they were used as a quality check tool as well. They were of great help especially when modifications to the software were performed.

software/scripts used	objective
downloading script	downloading instrumental data and metadata
exporting script	export downloaded data to a local machine
DistAz.exe	calculating distance and backazimuth to earthquake
ChamRot.exe	rotation of components, calculating time information
visual inspection script	previewing data after initial processing
SVAL.exe	frequency-time analysis - extracting the fundamental mode
ArrayCorr.exe	arary measurement
MerPha.exe	merging of phase velocity dispersion curves
data preview script	previewing the phase velocity measurements
SVAL.exe	inversion for depth
data preview script	previewing the final results

Table 1. List of software and scripts used throughout the study.

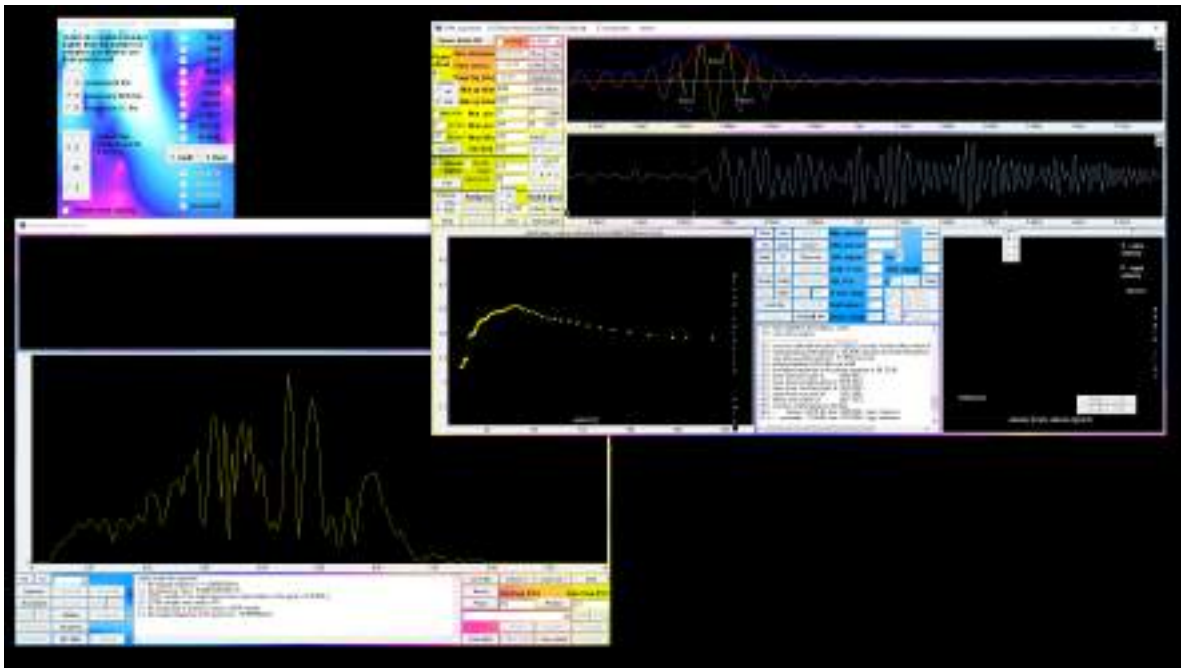

Figure 7. Screenshot from SVAL showing three different windows. The colorful window in the upper left corner is the first window to be seen once the program is started. The type of file used can be selected, as well as the length of the time window in maximum number of samples. The window on the right is the main window. It shows the different adjustable parameters on the left. On the right two panels one can see the raw record (second panel) and a 70s wavefrom after filtration (first panel). On the lower left, the group velocity dispersion curve of one records is shown in the 15-240s period range. As SVAL is used both for filtering the fundamental mode as well as inversion, the inversion window can be found on the right to the group velocity dispersion curve. The third window shows the record in the frequency domain. One has the option to preview all Gaussian filters as well as corresponding spectra. For more information, please check the text above.

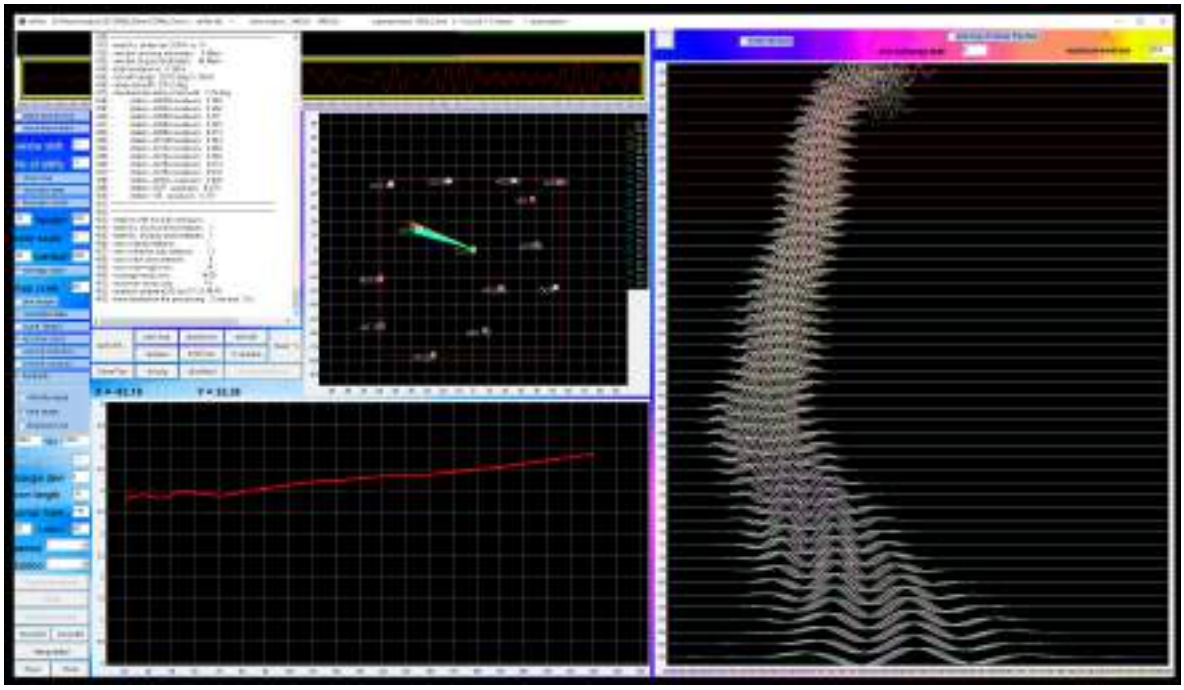

Figure 8. Screenshot from ArrayCorr. The blue panel on the left displays all parameters that can be selected. The program provides continuous information about the steps of calculation, as can be seen on the window. A geographical map is plotted for the current array that is being processed. The final phase velocity dispersion curve is plotted by red line. The window on the right shows the quasi-monochromatic signals for each period and at each station. Those signals are then shifted samples by samples for each period to obtain the time differences between the central station and its neighbors. The text above provides more details.

Chapter 3

Data

3.1 Stations

The first step of a research project after settling for an investigation region is to construct a station list which would provide an optimal coverage of the geographic area. In this section I present the stations used in the study as well as general statistics of earthquake data collected and used per station.

The initial set included a total of 63 stations from which 19 were permanent and 44 temporary. However, while processing the data, it was noticed that one permanent station did not perform well at long periods (T $>$ 100s) and had to be removed. Additionally, the list included 2 permanent stations in great geographical proximity of one another ($\sim$200 m). The idea behind this was to continuously use only one of the two stations and in case of a noisy record or missing data for a particular event, it would have been substituted by its backup neighbor. However, this was not the case and the second station was not used. Figure 9 shows the spatial distribution of the final 61 stations in the region of the wider Vienna Basin - 44 AlpArray temporary (red triangles) and 17 permanent stations (blue triangles).

As already mentioned in section 1.4 there were 4 A/B station pairs - the geographical location of station 'A' was changed due to external factors. The station at the new site obtained a name ending with 'B'. The A/B pairs never recorded simultaneously, they were substitute of one another. My final list of 61 stations includes all 8 of them (4 pairs of 2). Therefore, the maximum number of stations that could record one event was 57.

The diagram in Figure 10 reflects the amount of earthquake data available and used at 3 of the processing steps per station. The exact numbers are listed in the three very last columns in Table 2 along with station network code and instrument type. The 4 stations ending with 'X' are not physical but rather summarize the numbers for the A/B pairs. Blue color bar in Figure 10 shows the number of events initially downloaded and pre-processed at each station. The total number of earthquakes was 36 (black horizontal line). The temporary stations in Hungary (A260A, A261A, A268A, A268A) were deployed in the beginning of 2016. Therefore, for the first couple of events, they did not provide any records. On the other hand, station A009A was removed prior to the planned date which resulted in having way less data as it is evident from the histogram. The permanent stations ALLA, STAC, UNNA and WINA were deployed much later in time, which resulted in having small portion of events recorded ($<$ 8%). The same applies to stations RONA and VIE, however, they still provided more than 50 %. Lastly, stations A012A and A090A did not operate for short amount of time and I did not obtain data in the time window of the earthquakes. Occasionally, stations had a telemetry issue and no data was sent which again resulted in records missing. Nevertheless, for most stations more than 90% of the initial data set was available.

The green color bar reflects the number of earthquakes for which the fundamental mode of Rayleigh waves was successfully selected and the phase velocity dispersion curve could be calculated. At some stations, e.g. A012A, A017A, VYHS and others, more often there was a long noise component present in the records which biased the group velocity measurement

(low SNR). Thus, the event recorded at that station had to be disregarded. This is reflected by the difference in height between the blue and green color bars.

Finally, the red color bar depicts the stations which formed a subarray for which the phase velocity dispersion curves were calculated. As one can observe from Figure 9, stations A025A, A079A, A261A, A269A and VYHS are at the edge of the investigated region and do not have 5 or more neighbors in radius of 20 to 80 km (subarray criteria). Therefore, they never formed a subarray on their own. On the other hand, stations like A338A, MOA, EGYH and some others, had exactly 5 neighbors. In case one of the neighbors was missing for a particular event, the subarray also dropped off for that event.

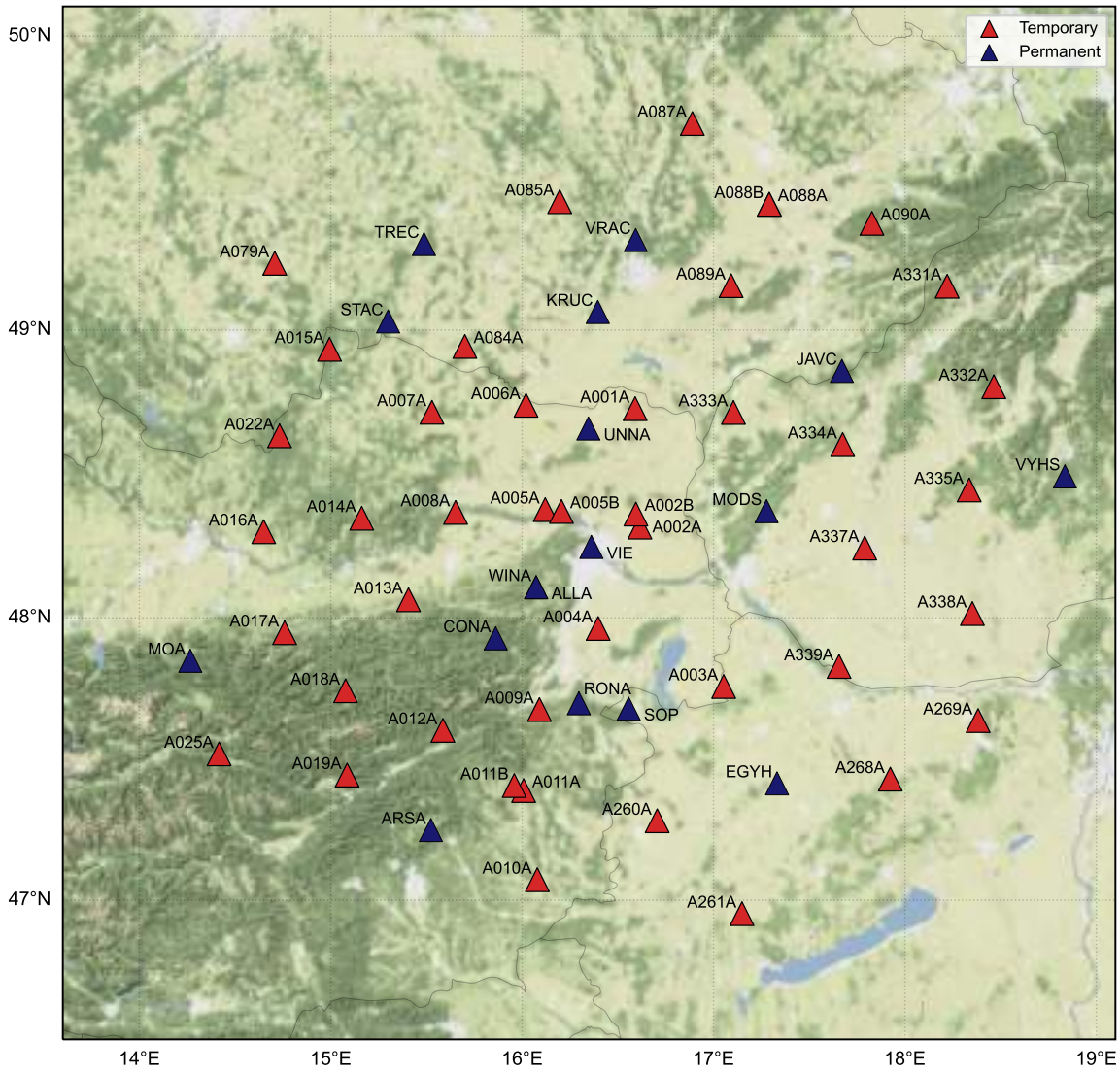

Figure 9. Map of temporary (red triangles) and permanent (blue triangles) seismic stations in the wider Vienna Basin.

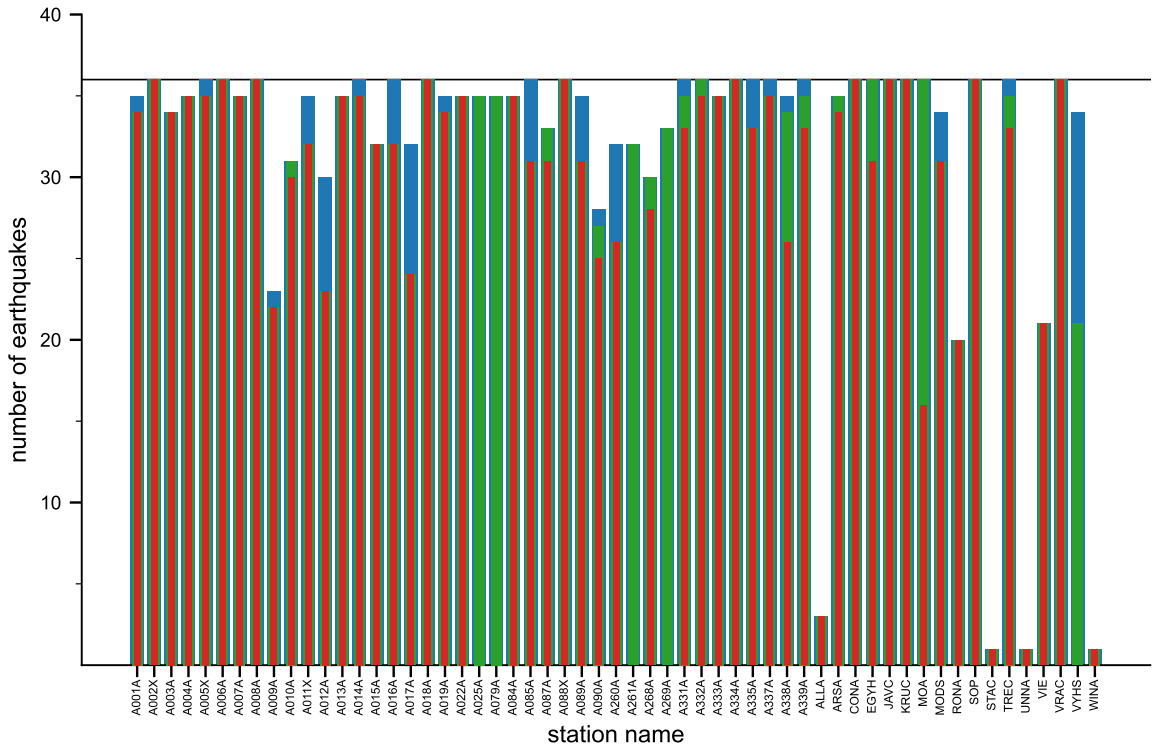

Figure 10. Histogram of the number of earthquakes recorded at each station. Blue color bars show the amount of data initially downloaded, green - number of earthquakes used for the array measurement, red - number of subarrays. The total number of earthquakes is 36. Temporary stations ending with 'X' are fictitious reflecting the A/B pairs together.

station name	network code	sensor type (corner period)	dwnldd	used	subarr
A001A	Z3	Reftek151 (60s)	35	34	34
A002X:			36	36	36
-A002A	Z3	Reftek151 (60s)	6	6	6
-A002B			30	30	30
A003A	Z3	Reftek151 (60s)	34	34	34
A004A	Z3	Reftek151 (60s)	35	35	35
A005X:			36	35	35
-A005A	Z3	Reftek151 (60s)	5	4	4
-A005B			31	31	31
A006A	Z3	Reftek151 (60s)	36	36	36
A007A	Z3	Reftek151 (60s)	35	35	35
A008A	Z3	Reftek151 (60s)	36	36	36
A009A	Z3	Reftek151 (60s)	23	22	22
A010A	Z3	Reftek151 (60s)	31	31	30
A011X:			35	32	32
-A011A	Z3	Reftek151 (60s)	5	4	4
-A011B			30	28	28
A012A	Z3	Reftek151 (60s)	30	23	23
A013A	Z3	Reftek151 (60s)	35	35	35
A014A	Z3	Reftek151 (60s)	36	35	35
A015A	Z3	Trillium (240s)	32	32	32
A016A	Z3	Reftek151 (60s)	36	32	32
A017A	Z3	Reftek151 (60s)	32	24	24
A018A	Z3	Reftek151 (60s)	36	36	36
A019A	Z3	Reftek151 (60s)	35	34	34
A022A	Z3	Trillium (240s)	35	35	35
A025A	Z3	Trillium (240s)	35	35	-
A079A	Z3	STS-2 (120s)	35	35	-
A084A	Z3	STS-2 (120s)	35	35	35
A085A	Z3	STS-2 (120s)	36	31	31
A087A	Z3	STS-2 (120s)	33	33	31
A088X:			36	36	36
-A088A	Z3	STS-2 (120s)	13	13	13
-A088B			23	23	23
A089A	Z3	STS-2 (120s)	35	31	31
A090A	Z3	CMG-40T (30s)	28	27	25
A260A	Z3	CMG-3T (120s)	32	26	26
A261A	Z3	CMG-3T (120s)	32	32	-
A268A	Z3	CMG-3T (120s)	30	30	28
A269A	Z3	CMG-3T (120s)	33	33	-
A331A	Z3	Reftek151 (60s)	36	35	33
A332A	Z3	Reftek151 (60s)	36	36	35
A333A	Z3	Reftek151 (60s)	35	35	35
A334A	Z3	Reftek151 (60s)	36	36	36
A335A	Z3	Reftek151 (60s)	36	33	33
A337A	Z3	Reftek151 (60s)	36	35	35
A338A	Z3	Reftek151 (60s)	35	34	26
A339A	Z3	Reftek151 (60s)	36	35	33
ALLA	XX	STS-2 (120s)	3	3	3
ARSA	OE	STS-2 (120s)	35	35	34
CONA	OE	STS-2 (120s)	36	36	36
EGYH	HU	CMG-3T (120s)	36	36	31
JAVC	CZ	STS-2 (120s)	36	36	36
KRUC	CZ	STS-2 (120s)	36	36	36
MOA	OE	STS-2 (120s)	36	36	16
MODS	SK	STS-2 (120s)	34	31	31
RONA	OE	STS-2.5 (120s)	20	20	20
SOP	HU	STS-2 (120s)	36	36	36
STAC	CZ	MBB-1 (40s)	1	1	1
TREC	CZ	CMG-3T (120s)	36	35	33
UNNA	OE	STS-2.5 (120s)	1	1	1
VIE	OE	CMG-3T (120s)	21	21	21
VRAC	CZ	CMG-3T (120s)	36	36	36
VYHS	SK	CMG-3T (120s)	34	21	-
WINA	OE	STS-2.5 (120s)	1	1	1

Table 2. Temporary and permanent seismic stations used in the study along with their network code and sensor type. Number of earthquakes downloaded (dwnldd) and used per station as well as number of earthquakes for which a station formed a subarray is shown. The total number of earthquakes is 36. Underlined stations are fictitious representing A/B pairs together. See section 2.4 for details.

3.2 Earthquakes

Once I settled for the initial set of stations, I needed to construct a list of earthquakes appropriate for the study. The USGS Earthquake Catalog was the engine I used for searching events from all over the world. The procedure started by listing all earthquakes with magnitudes bigger than 7 in the years between beginning of 2016 and end of 2019. In case of multiple events from the same location, the one with the highest magnitude was kept, all others were excluded. The raw records were previewed and those with poor surface wave amplitudes were disregarded. At this stage the earthquake list consisted of around 30 teleseismic events both of shallow and intermediate depths (up to 200 km).

Next, more shallow events (focal depth $<$ 15km) with magnitudes bigger than 6.5 were added and again previewed. 5 events made it to the list - 2 regional from Greece, one from Japan as well as 2 events from rare South azimuths, resulting in a total of 35 earthquakes. As already mentioned, most of the temporary AlpArray stations in the investigated region were deployed by autumn 2015 and continued recording after the official end of the project (April 2019). Therefore, I could extend my list further and search for events from the end of 2015 and beginning of 2020. 2 additional events with M $>$ 7 were found and the list was completed. The total number of earthquakes was 37.

While calculating the group velocity dispersion curves, one event had to be removed due to it's complexity. Therefore, the final data set included 36 regional-to-teleseismic events with magnitudes $>$ 6.5 and various hypocentral depths - from shallow to intermediate. Figure 11 shows a map of the event locations (pink crosses) and the overall azimuthal coverage. Pink solid lines depict the great-circle paths pointing to a station in the center of the wider Vienna Basin (blue triangle).

Figure 12 shows the number of stations that recorded each earthquake. As mentioned in the previous section, the maximum number of stations of the total 61 that could simultaneously record one event was 57 due to the 4 A/B pairs. The horizontal axis in the bar chart corresponds to the events listed in Table 3 ordered ascending in time - from 2015 to 2020. The table provides additional information on location, origin date and time as well as epicentral parameters (magnitude and focal depth) of each earthquake.

The blue color bar in the histogram represents the number of stations that were initially downloaded. To be precise, it reflects the number of raw records downloaded and pre-processed. On average, earthquakes were recorded by almost 90% of the stations (blue horizontal line). It is visible that the first and very last event provided significantly less data. The reason behind is that the investigated region was not fully covered with temporary AlpArray stations yet or they were already removed, respectively. However, 70% of the stations were functional and provided data, therefore, the earthquake was kept further. As already mentioned, the temporary AlpArray stations in Hungary were deployed a bit later than other stations in the investigated region, therefore, the less numbers for the very first earthquakes.

Next, I would like to point to the green color bar within the blue. It shows for how many of the pre-processed stations the fundamental mode of Rayleigh waves was successfully picked per earthquake. The most common reason why a station record was excluded for a particular event was poor SNR. Certain stations were occasionally noisy probably due to external factors in the site of deployment or maybe weather conditions. However, not more than 10% of the initially pre-processed stations were excluded from the measurement.

Lastly, the red color bar depicts the number of subaarays formed for each earthquake event.

Generally, 5 stations never could form a subarray - due to their location they never met the criteria (check previous sections for details). Additionally, there were stations that fulfilled only the minimum requirements. In case, one of their neighbors was absent, it resulted in overall less subarrays for that one event. The exact numbers presented in the histogram can be found in Table 3 under columns 'dwnldd', 'used' and 'subarr'.

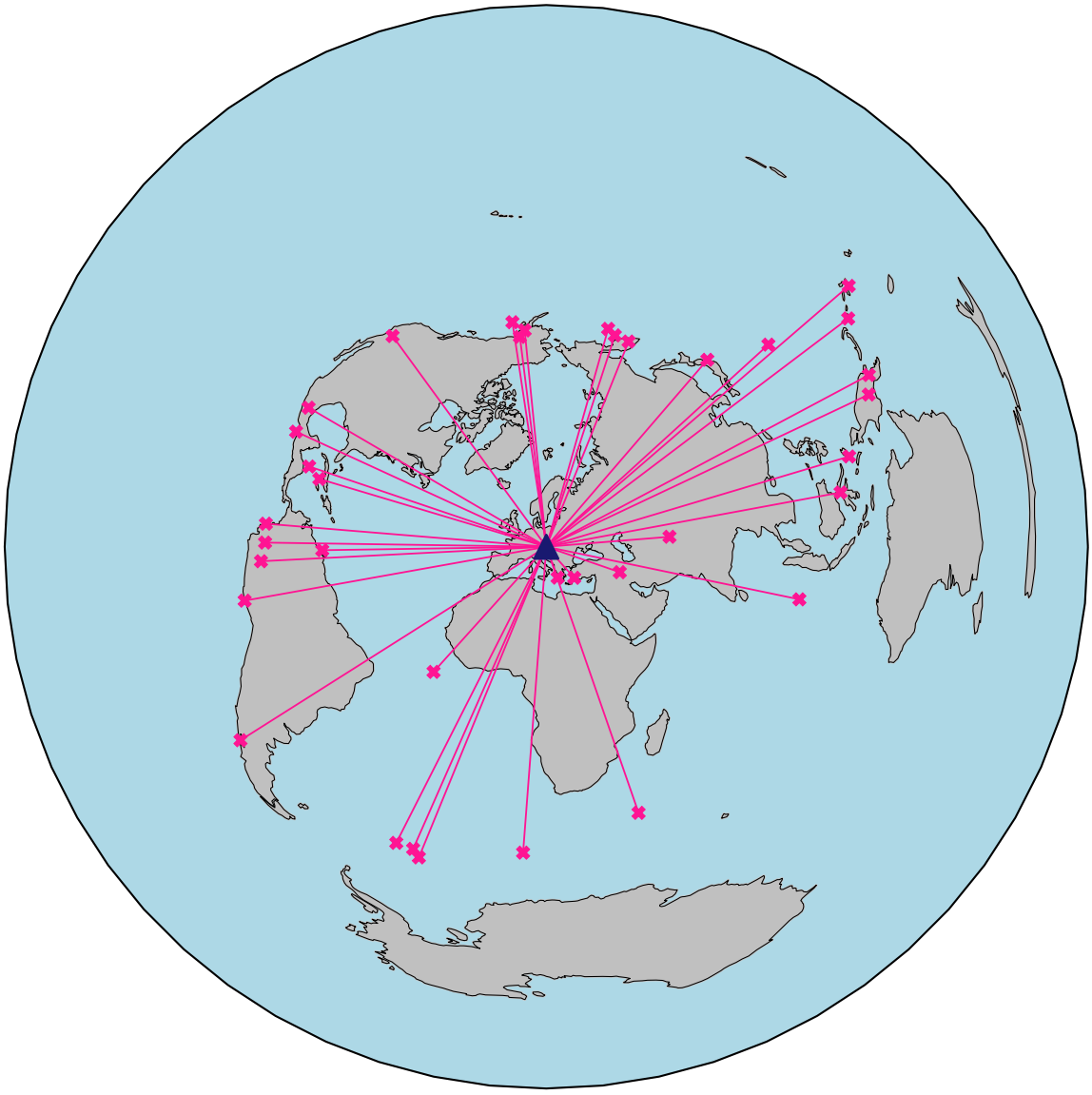

Figure 11. Map of earthquakes used in the study. Dark blue triangle marks the location of station CONA, approximately in the middle of the investigated region. Pink lines show great-circle paths. Details about epicentral parameters of each event can be found in Table 3.

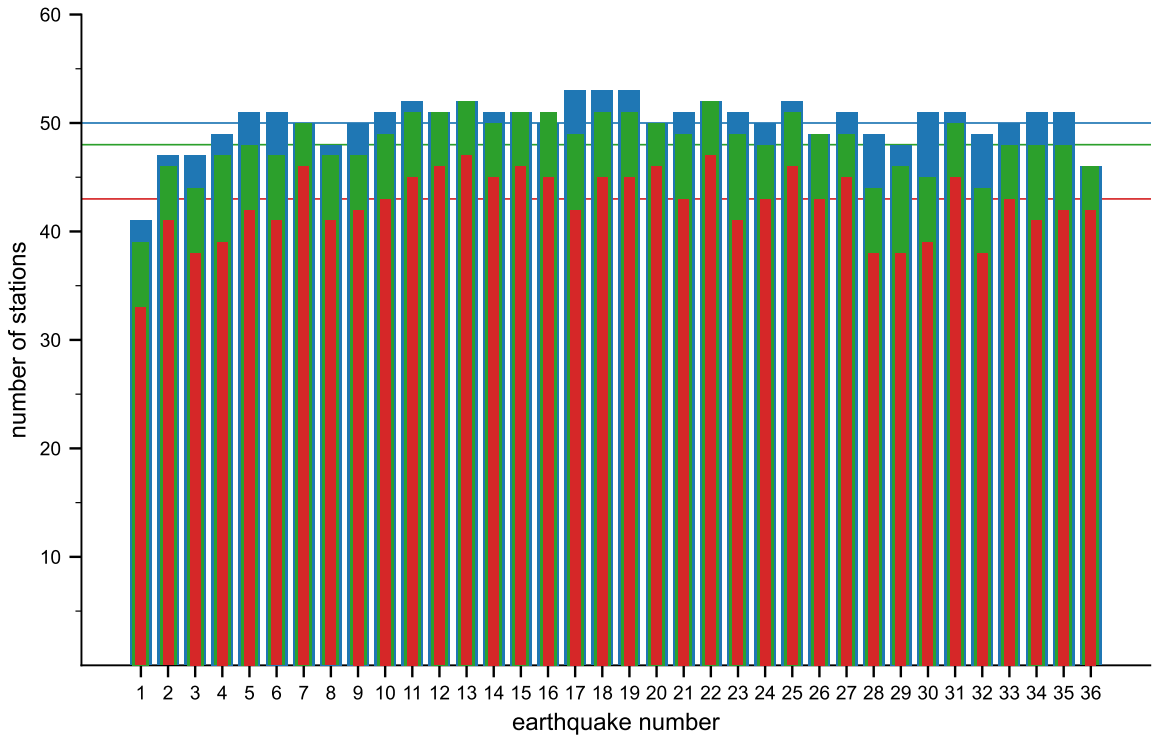

Figure 12. Histogram of the data presented in Table 2. Blue color bars reflect the number of stations downloaded, green - number of stations used for the array measurement, red - amount of stations forming a subarray per earthquake. Horizontal lines shows the average for each case respectively. The total number of stations is 57.

	location	date (yyyy-mm-dd)	origin time	M	depth (km)	dwnldd	used	subarr	period range (sec)	figure
1	Afghanistan	2015-10-26	09:09:43	7.5	231	41	39	33	42-160	Figure A.1
2	Alaska	2016-01-24	10:30:30	7.1	126	47	46	41	27-105	Figure A.2
3	Kamchatka	2016-01-30	03:25:12	7.2	177	47	44	38	35-177	Figure A.3
4	Sumatra	2016-03-02	12:49:48	7.8	24	49	47	39	55-226	Figure A.4
5	Ecuador	2016-04-16	23:58:37	7.8	21	51	48	42	28-190	Figure A.5
6	South Atlantic	2016-05-28	09:47:00	7.2	78	51	47	41	32-177	Figure A.6
7	Mariana	2016-07-29	21:18:25	7.7	196	50	50	46	44-226	Figure A.7
8	South Atlantic	2016-08-19	07:32:23	7.4	10	48	47	41	18-226	Figure A.8
9	Ascension	2016-08-29	04:29:58	7.1	10	50	47	42	26-210	Figure A.9
10	Japan	2016-11-21	20:59:49	6.9	9	51	49	43	30-149	Figure A.10
11	Solomon	2016-12-08	17:38:46	7.8	40	52	51	45	40-190	Figure A.11
12	Chile	2016-12-25	14:22:27	7.6	38	51	51	46	31-186	Figure A.12
13	Papua	2017-01-22	04:30:23	7.9	135	52	52	47	44-190	Figure A.13
14	Komandorskiye	2017-07-17	23:34:14	7.7	10	51	50	45	31-238	Figure A.14
15	Kos	2017-07-20	22:31:11	6.6	7	51	51	46	12-62	Figure A.15
16	Mexico	2017-09-08	04:49:19	8.2	47	50	50	45	29-232	Figure 2
17	Mexico	2017-09-19	18:14:38	7.1	48	53	49	42	33-232	Figure A.16
18	Bouvet	2017-10-10	18:53:28	6.7	9	53	51	45	36-156	Figure A.17
19	Iraq	2017-11-12	18:18:17	7.3	19	53	51	45	25-110	Figure A.18
20	Honduras	2018-01-10	02:51:33	7.5	19	50	50	46	17-200	Figure A.19
21	Peru	2018-01-14	09:18:46	7.1	39	51	49	43	61-195	Figure A.20
22	Alaska	2018-01-23	09:31:41	7.9	14	52	52	47	21-200	Figure A.21
23	Papua	2018-02-25	17:44:44	7.5	25	51	49	41	69-210	Figure A.22
24	Venezuela	2018-08-21	21:31:48	7.3	147	50	48	43	32-177	Figure A.23
25	Indonesia	2018-09-28	10:02:45	7.5	20	52	51	46	27-160	Figure A.24
26	Greece	2018-10-25	22:54:53	6.8	14	49	49	43	12-62	Figure A.25
27	Alaska	2018-11-30	17:29:29	7.1	47	51	49	45	29-84	Figure A.26
28	South Atlantic	2018-12-11	02:26:29	7.1	133	49	44	38	44-138	Figure A.27
29	Komandorskiye	2018-12-20	17:01:55	7.3	17	48	46	38	36-116	Figure A.28
30	Prince Edward	2019-01-22	19:01:44	6.7	13	51	45	39	38-135	Figure A.29
31	Ecuador	2019-02-22	10:17:24	7.5	145	51	50	45	34-156	Figure A.30
32	Papua	2019-05-06	21:19:38	7.1	146	49	44	38	56-177	Figure A.31
33	Peru	2019-05-26	07:41:15	8.0	123	50	48	43	37-210	Figure A.32
34	California	2019-07-06	03:19:53	7.1	8	51	48	41	33-195	Figure A.33
35	Indonesia	2019-07-14	09:10:52	7.2	19	51	48	42	42-160	Figure A.34
36	Jamaica	2020-01-28	19:10:25	7.7	15	46	46	42	32-186	Figure A.35

Table 3. Earthquakes used in the study including date, origin time, magnitude and depth. The number of downloaded (dwnldd) and used stations for each earthquake is listed. Number of subarrays as well as analyzed period range are shown.

Chapter 4

Results

In the following paragraphs, I will present and discuss my results. The chapter is divided into two parts. First, the merged phase velocity dispersion curves corresponding to each subarray are discussed. Even before inverting for depth and obtaining the 1-D shear-wave velocity models, some trends were observed. Different ways of looking at the dispersion curves are shown, including phase velocity maps at different periods. Second part focuses purely on the results after the inversion. 1-D structural models corresponding to the subarrays are examined. Additionally, shear-wave velocity maps at different depths are presented.

4.1 Phase velocity dispersion curves

The following parameters were used to restrict the merging of different earthquakes for all subarrays. The allowed derivative of the velocity with respect to period was 0.09 km/s/s. Periods for which the derivative was higher, were eliminated. A minimum of 4 events at each period were used. This way the period range was further restricted. Finally, the cut-off angle was set to 15°. If the arrival angel deviation corresponding to a phase velocity value was bigger than ± 15°, the measurement was not used for merging. The total amount of subaarays was 52. However, 4 of them had phase velocity dispersion curves for only 4 earthquakes. Therefore, a merged curve was not calculated.

Let's start by looking at Figure 13. Two different subarrays are shown - station CONA located in the Alps and station A339A in the Little Hungarian Plain. Figures for the other 46 subarrays can be found in the Appendix of the thesis (section A.2). Phase velocity dispersion curves corresponding to different earthquakes are shown by color on the first panel. The color assigned to each earthquake is preserved for all subarrays.

By looking at the first panel of each subarray, one can clearly see the abrupt velocity jumps at short periods. For the phase velocity measurement to be so scattered, the fundamental mode selection at those periods must have been wrong. Either the wrong wavegroup has been selected, or the phases were distorted. At periods as short as 30s different wavegroups arrive. Usually, their amplitude exceeds the amplitude of the fundamental mode. Therefore, it is not straight-forward to select the proper wavegroup corresponding to the fundamental mode. However, by applying the derivative criterion, the jumps were cleared. Panel 4 of the same figure shows the clean period range of the measured dispersion curves used for merging.

On panel 2, the arrival angle deviations are shown. That is the difference between the measured arrival angle and the theoretical great-circle backazimuth of each event. For long periods, as expected, most deviations are around 0. However, short periods are scattered to greater values. At the same time, the arrival angle deviations are usually in the range of ±15°. This shows that the restriction set by the cut-off angle is reasonable and reflects the observed data.

The third panel shows the residuals for each event. They were calculated by averaging the residuum over all neighboring stations at each period separately. One can observe that they somewhat match the pattern of the phase velocity wobbles. They include important,

inseparable information. First, they give an estimate about how well the correlation performed. Second they include information of the wavefront curvature. If the wavefront was not a plane wave, what the assumption was, some neighboring stations would produce systematically lower or higher residuals.

Finally, the merged dispersion curves at the two subarrays can be seen by black dots on panel 4. The standard deviation at each period is plotted as well. By looking at the merged and measured curves, one can clearly see that the wobbles are highly suppressed over the period range.

I would like to point the reader to the two wobbled dispersion curves at subarray A339A - darker green (70s and 130s) and red (around 100s). They do not have high arrival angle deviations at the corresponding periods. This means that the weight that will be assigned to the velocity value will be high. Therefore, the velocity measurement will be highly taken into account. This of course, biases the merged curve. It influences not only the velocity at those periods, but also produces higher standard deviations. Nevertheless, when looking at the merged curves, the overall effect of wobbles is strongly reduced. The same holds for the light green dispersion curve at CONA with a wobble around 100s. I would say that even if not always perfect, the merging produces reliable results.

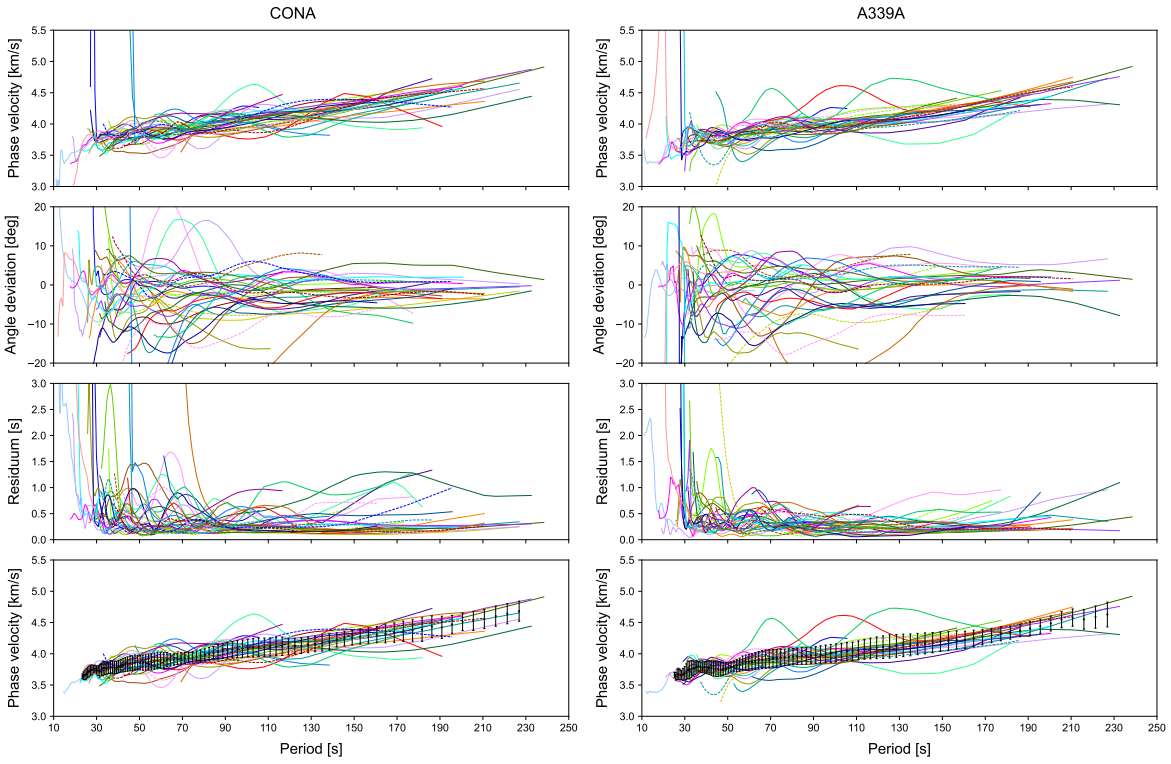

Figure 13. Measured phase velocity dispersion curves from different earthquakes at 2 subarrays (first panel). The arrival angle with respect to the period as well as the residuum are shown. The residuum was calculated as an average of the residuals for all neighboring stations at every period. Last panel shows the dispersion curves after the derivative criterion was applied while merging. The solid black line corresponds to the averaged phase velocity dispersion curves at each subarray. Their standard deviation is shown at each period.

To give the reader a better feeling of the overall merging procedure I will discuss some

statistics. Figure 14 will serve as a supporter for explaining. The histograms provide information for the overall period range of all 48 subarrays. On the left, the number of subarrays is shown. Let's look at the shortest period of 23s. Merged dispersion curves of only 4 subarrys start at such short periods. However, the dispersion curves were merged for all subarrays at least in the 30-200s range. 93 % of all curves continue to even longer periods. Having such broad period range allowed for inverting to greater depths.

On the right side of the figure, the number of measurements is presented. This number includes the number of phase velocity points from all measured dispersion curves from all subarrays. Let's consider the period of 23s again. As mentioned, merged dispersion curves of 4 subarrays start at this period. The minimum criteria of events was 4. Therefore, at least 16 measurement points should be reflected in the figure. In fact, they are 17. This implies that for one of the subarrays there were 5 velocity points found.

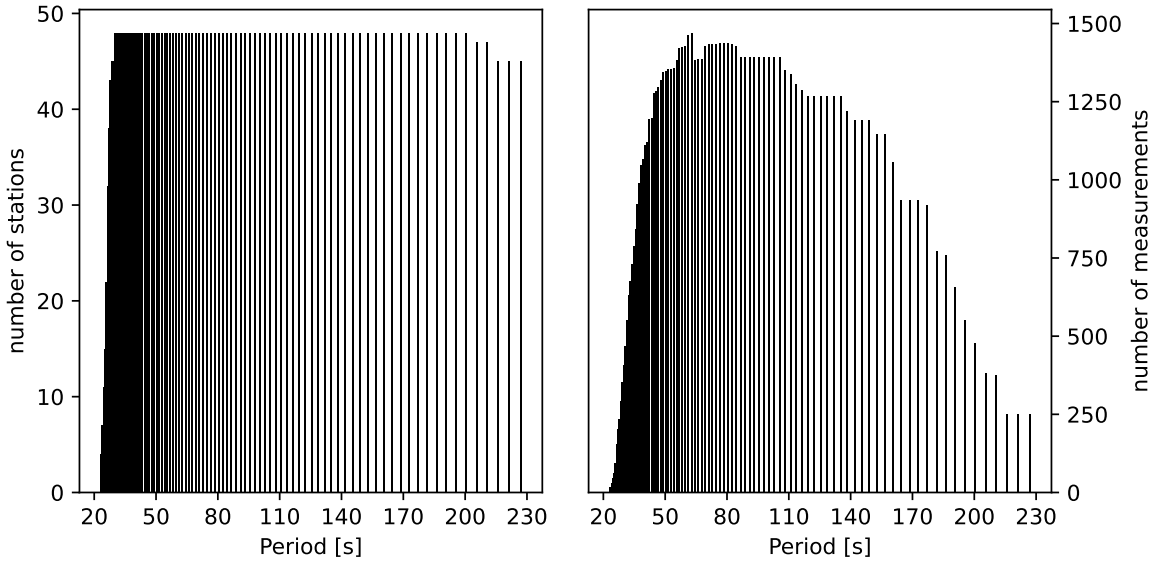

Figure 14. Histograms of the full period range for all subarrays. Panel on the left shows the number of subarrays including each particular period. On the right, the number of measurements used at every period is shown.

To observe whether there was any pattern in the velocity distribution in the whole region, phase velocity maps were plotted. I refer the reader to Figure 15. Each panel shows the relative change in velocity in the region of waves with different periods. Please note that the period is not trivially connected to any depth. Surface waves of different periods are sensitive to all depths. Although, it is true that shorter periods are more sensitive to the shallower parts (crust) and longer periods to deeper parts (upper mantle), no conclusion can be made about the structure of the region. However, the velocity maps do show differences from region to region. For example, at 30s period, a blue fast patch can be clearly seen. One might say that it corresponds to the Bohemian Massif. As well as the low velocities in the Little Hungarian Plain seem to be observed. However, all velocity maps show that the subarrays in northeast have relatively low velocities when compared to other regions. This does not necessary reflect the topology on the surface.

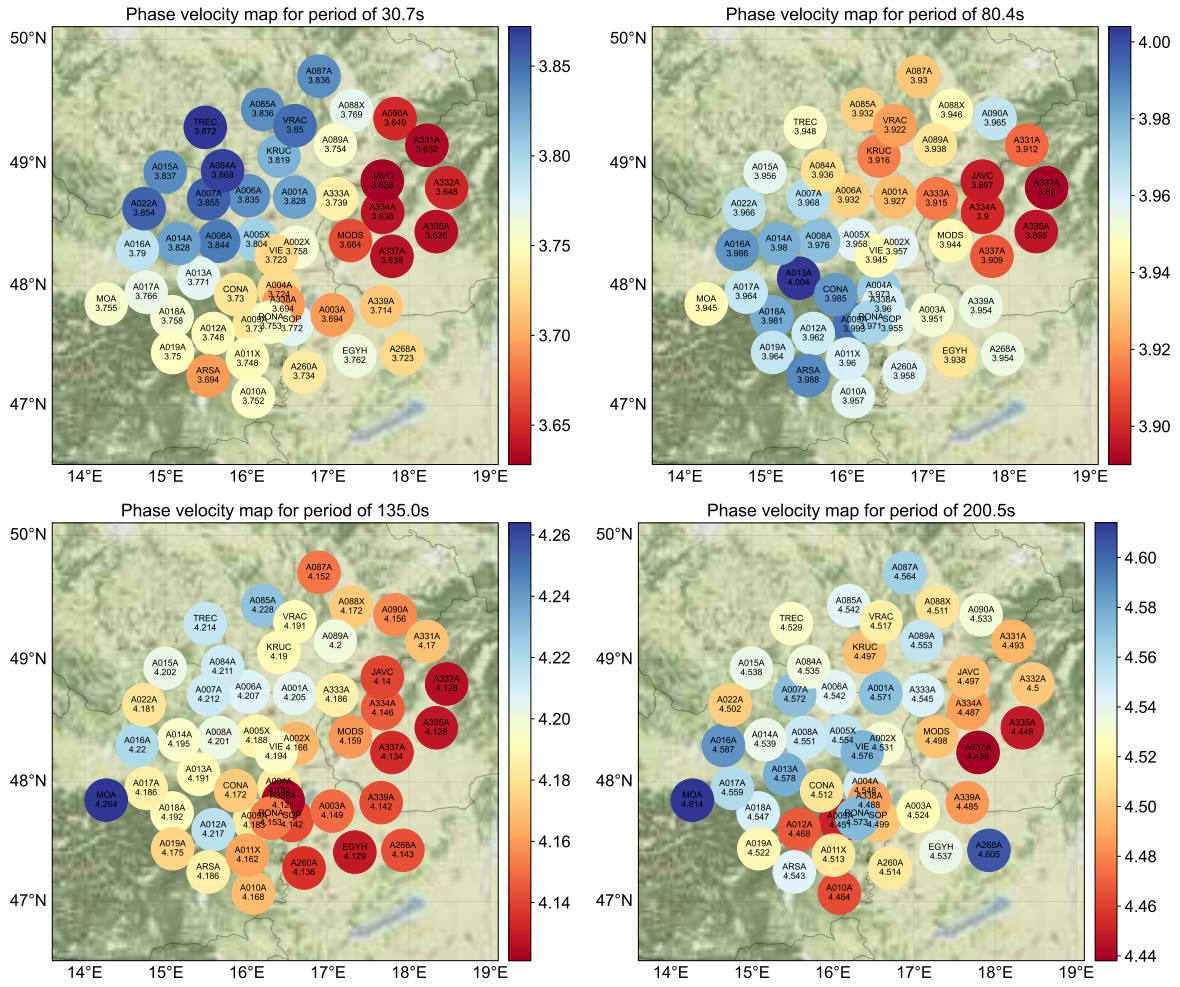

Figure 15. Phase velocity maps at 4 periods. The color scale reflects the relative change in velocity at each period.

All those observations triggered the idea of assigning the merged dispersion curves to a tectonic unit. There are five main units in the investigated region. By looking at a map, reflecting the surface topography, each stations was put in a category, see Figure 16. The Vienna Basin is the central unit (yellow color in Figure 16). To the northwest is the Bohemian Massif (orange dots), southwest - the Eastern Alps (purple dots). The Carpathians, depicted by green dots, are located northeast from the Vienna Basin and finally, by blue is the Little Hungarian Plain. The idea was to simply review the dispsersion curves and see whether there is any pattern spanning the whole period range.

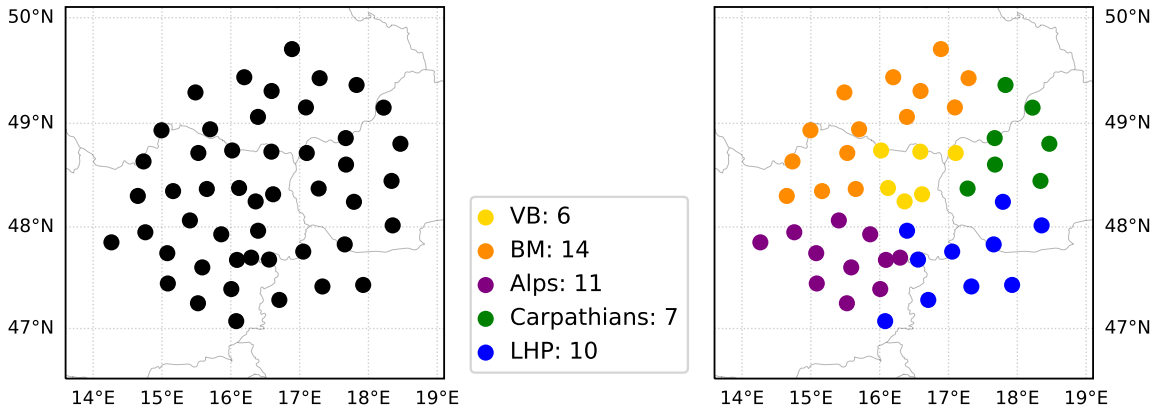

Figure 16. Map showing the assignment of tectonic units to each subarray in the investigated region.

Figure 17 shows the results. A clear separation can be seen for shorter periods. Up to 70s waves propagate the fastest in the Bohemian Massif (orange curves). What was also observed from the phase velocity maps is the low velocity in the region of the Carpathians (green). For longer waves up to 150-170s one can still distinguish between the units. However, for even longer periods not much can be observed.

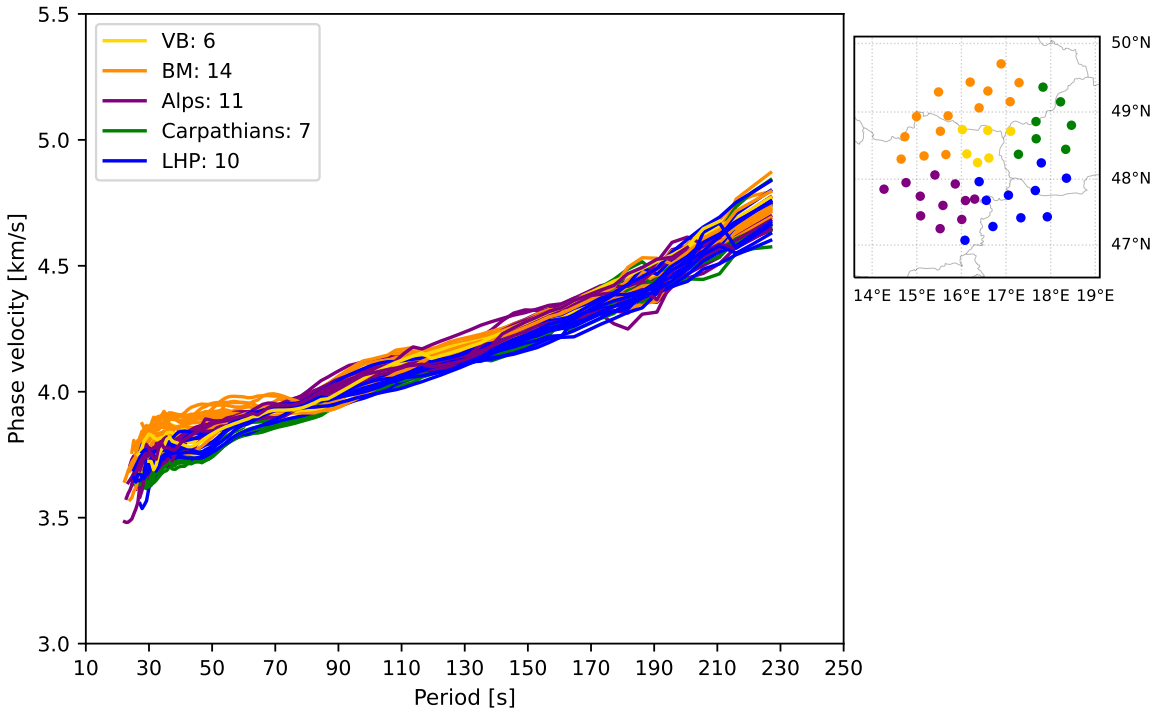

Figure 17. Merged phase velocity dispersion curves separated by color representing one of the 5 tectonic units.

4.2 Shear-wave velocity at depth

The results of the inversion for the 2 subarrays - CONA and A339A, are shown in Figure 18. Each figure consists of 4 panels. On the left, there is a geographical map of the wider Vienna Basin showing the subarray distribution. The current subarray is depicted by the circle with red circumference. All neighboring subarrays are plotted with the color of the tectonic unit they belong to. Please note that some stations were reassigned after looking at all 1-D velocity models. This will be discussed later in the text.

Next to the map, a misfit-complexity plot can be found. Each 1-D model is characterized by one parameter - the product of misfit and complexity. Misfit is the difference between the modeled and measured dispersion curve. Generally, the misfit of the final model is not the lowest. However, the complexity usually is. The complexity measures the "smoothness" of each model. A model which has big velocity jumps in absolute value between layers would produce high complexity. Finally, the product of the two is shown by yellow-to-blue colors in the figure. Looking at the relationship between misfit and complexity, one can conclude that usually, the final model (red dot) has both the lowest complexity and the lowest product of complexity and misfit.

On the right panel, all 100 computed models are shown. The ones with the lowest product are shown on top by yellow color. The final model, calculated by averaging all models, is shown by red color. The error bars mark the standard deviation in each layer. To each model, the corresponding forward-calculated dispersion curve is shown on the left bottom panel. Again, all curves are plotted with colors according to their product value. On top, the merged curve to each subarray is plotted. The dispersion curve corresponding to the final mean model can be seen by red color.

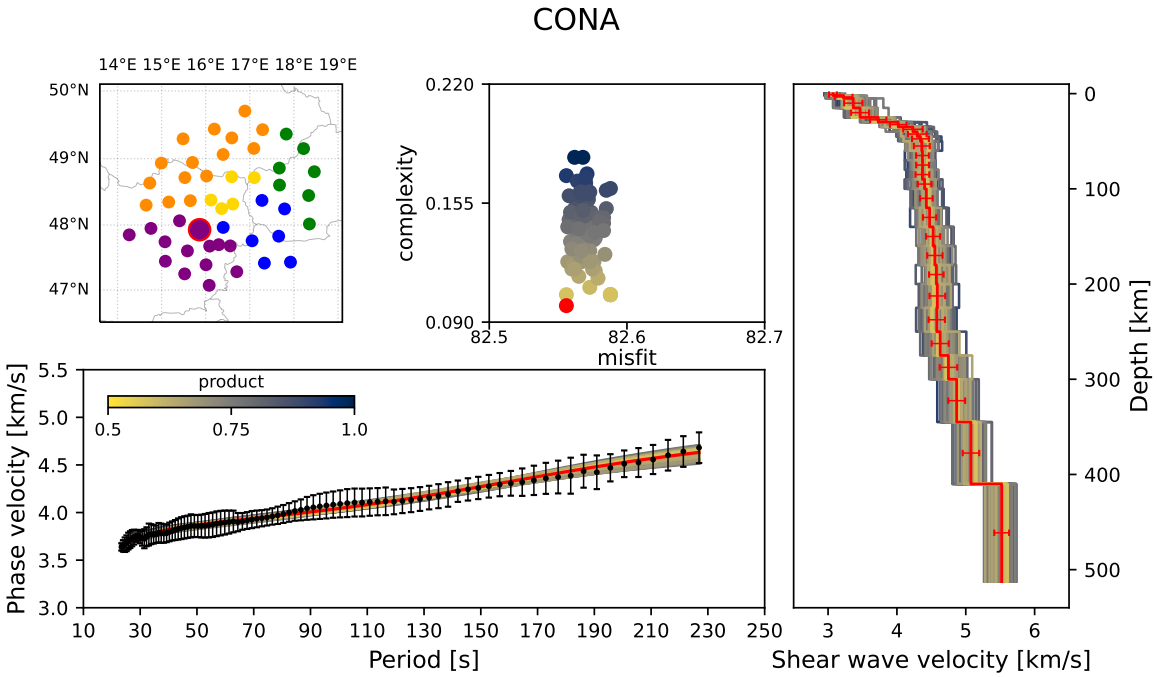

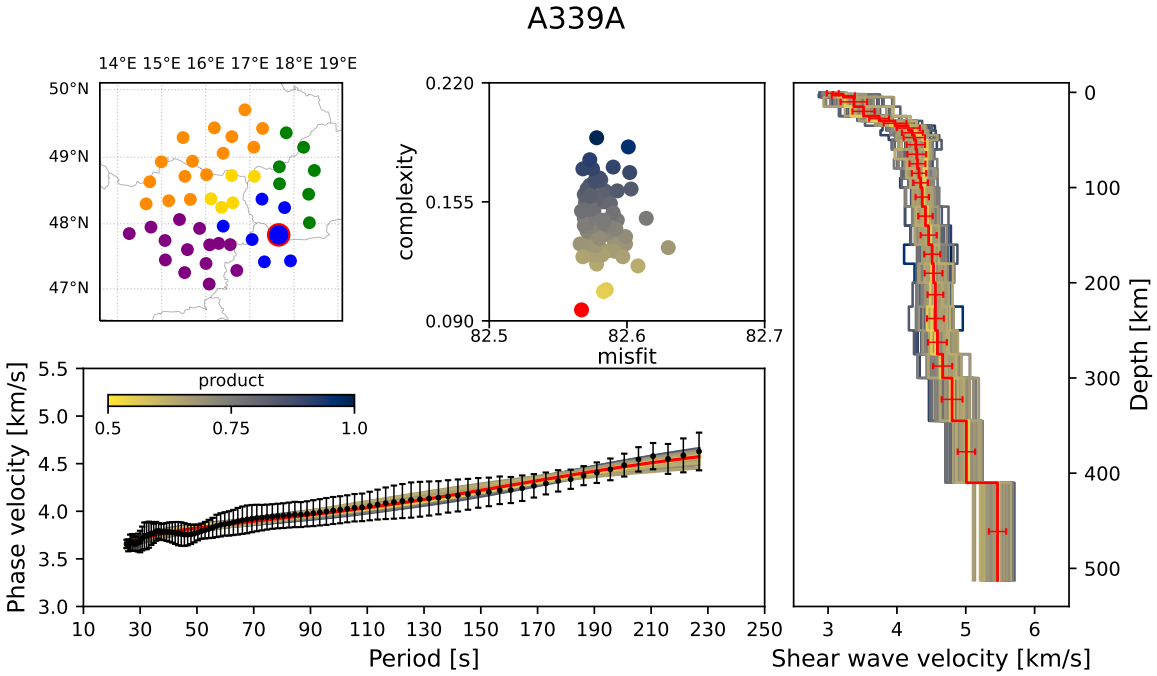

Figure 18. Inversion results for subarrays CONA and A339A previously shown in Figure 13. On the geographical map the location of the subarray is depicted by the circle with red circumference. On the right all 100 1-D models are plotted. They are plotted by color from highest to lowest complexity-misfit product. The red line corresponds to the final mean 1-D structural model and it's standard deviation. Bottom left panel shows the merged dispersion with standard deviation by black dots. In the background one can find the 100 modeled dispersion curves each corresponding to its model. They are as well plotted by color. The dispersion curve corresponding to the final structural model is shown by red color.

Now I would like to discuss the reasoning behind reassigning some subarrays to a new tectonic unit. Once all 1-D shear-wave velocity models were previewed, it was noticed that some did not match the tectonic unit they belonged to. Instead of looking at the topography on the surface, the subarrays were judged by their velocity distribution in the upper mantle layers - starting at around 50km down to 300km.

A total of 6 subarrays were reassigned to neighboring tectonic units. From the Little Hungarian Plain region three were moved to the Eastern Alps and one to the Carpathians. One subarray in the Vienna Basin was assigned to the Bohemian Massif and one from the Carpathians to the Little Hungarian plain. One can conclude and confirm the fact that the topography on the surface does not necessarily reflect the deeper structure beneath a subarray. Moreover, is was observed that 2 subarrays did not match any of the surrounding tectonic units. This implies that in greater depths they reach different units.

Let's compare the two subarrays in Figure 18. By looking on the right panel, one can see that all 1-D structural models for A339A are generally shifted to lower shear wave velocities. However, the overall shape of the mean models seems to be very similar. What is expected and also observed, is that the shear-wave velocity gradually increases with depth.

The next figures show shear-wave velocity maps at different depths (Figure 19). The maps start at very low crust depth to the halfspace below 410 km. The color scale is fixed to each layer and reflects the velocity deviation with respect to the mean in percentage. The

same maps with the color scale fixed for all depths are presented in section A.4 of the thesis' Appendix. There the gradual increase of velocity with depth can be observed.

Surface waves of periods up to 30-35s are mostly sensitive to the crustal structure. As the dispersion curves used for the inversion did not extend to such low periods, the interpretation of the crustal velocities is not reliable. Moreover, please note that the first layer of depths 0-2km is rather constrained and does not reflect the real data.

If one looks at the maps starting at depth below 2km, some patterns can be observed. The Bohemian Massif, located to the northwest of Vienna Basin, appears to be the fastest in the depths between 15-50km relative to its surrounding units. Some low velocity patches can be seen in the southwest and northeast.

At depths greater than 50km, the Alpine region and the Bohemian Massif show high relative velocities. Even at these depths, the Carpathians still appear to be slow. The high and low velocity zones are separated by the Vienna Basin where the shear-wave velocity is intermediate.

Looking at the layer of 70-80km, northeast edge, station A090A does not match any of it's neighbors. It is faster than the stations in the Carpathians, but it is also slower compared to the Bohemian Massif. This behavior can be tracked down to depths up to 100km.

Interesting to observe is subarray ARSA, located southwest in the Alps at the edge of the investigated region. Starting at depth of 80 km, it is quite visible that the velocity is significantly higher than the surrounding area. This is a prominent observation up to 160km depth. However, the behavior continues until the halfspace.

Going deeper, around 180km, there are two stations relatively faster (MOA) and slower (A087A) compared to their surroundings. This is highly pronounced up to 300km for MOA and to a bit shallower depth for A087A.

The velocity distribution is not too reliable at depths below 250km as the sensitivity of surface waves decreases. However, around 300km down to the halfspace the region between the Carpathians and the Little Hungarian Plain seems to be relatively slow compared to the Vienna Basin.

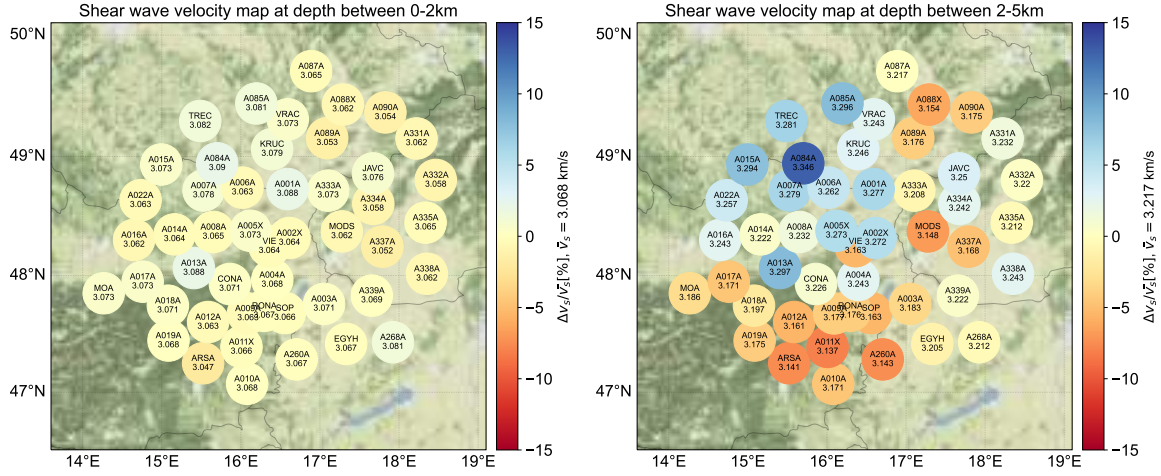

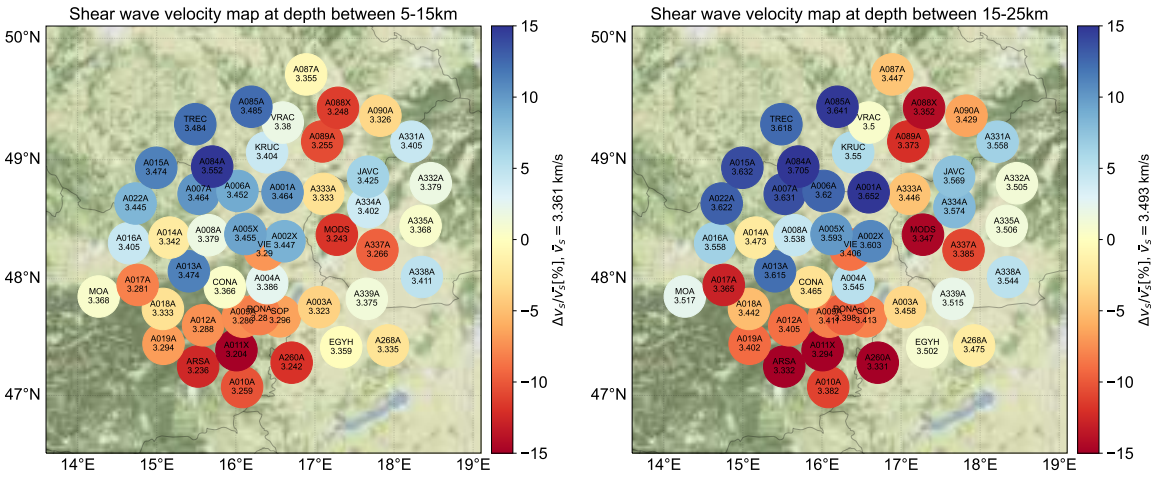
Shear wave velocity map at depth between 5-15km
Shear wave velocity map at depth between 15-25km
50°N
49°N
48°N
47°N
14°E
15°E
16°E
17°E
18°E
19°E
15
10
5
0
−5
−10
−15
$\Delta v_S/\bar{v}_S$[%], $\bar{v}_S$ = 3.361 km/s
$\Delta v_S/\bar{v}_S$[%], $\bar{v}_S$ = 3.493 km/s

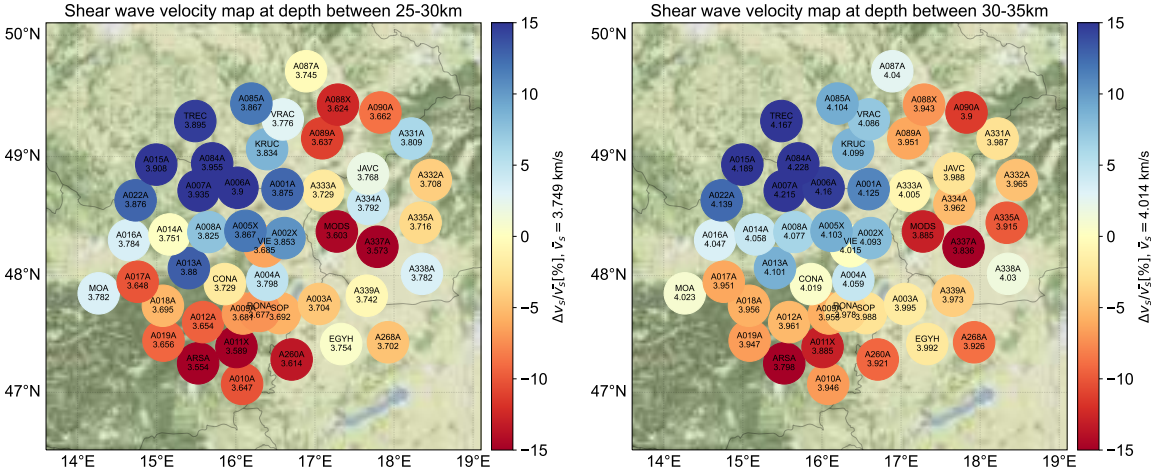
Shear wave velocity map at depth between 25-30km
Shear wave velocity map at depth between 30-35km
50°N
49°N
48°N
47°N
14°E
15°E
16°E
17°E
18°E
19°E
15
10
5
0
−5
−10
−15
$\Delta v_S/\bar{v}_S$[%], $\bar{v}_S$ = 3.749 km/s
$\Delta v_S/\bar{v}_S$[%], $\bar{v}_S$ = 4.014 km/s

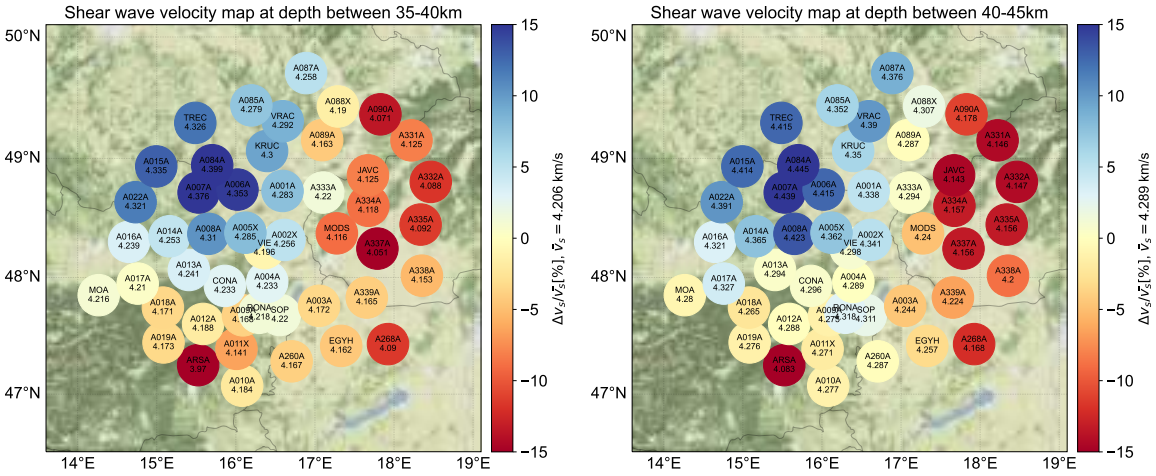
Shear wave velocity map at depth between 35-40km
Shear wave velocity map at depth between 40-45km
50°N
49°N
48°N
47°N
14°E
15°E
16°E
17°E
18°E
19°E
15
10
5
0
−5
−10
−15
$\Delta v_S/\bar{v}_S$[%], $\bar{v}_S$ = 4.206 km/s
$\Delta v_S/\bar{v}_S$[%], $\bar{v}_S$ = 4.289 km/s

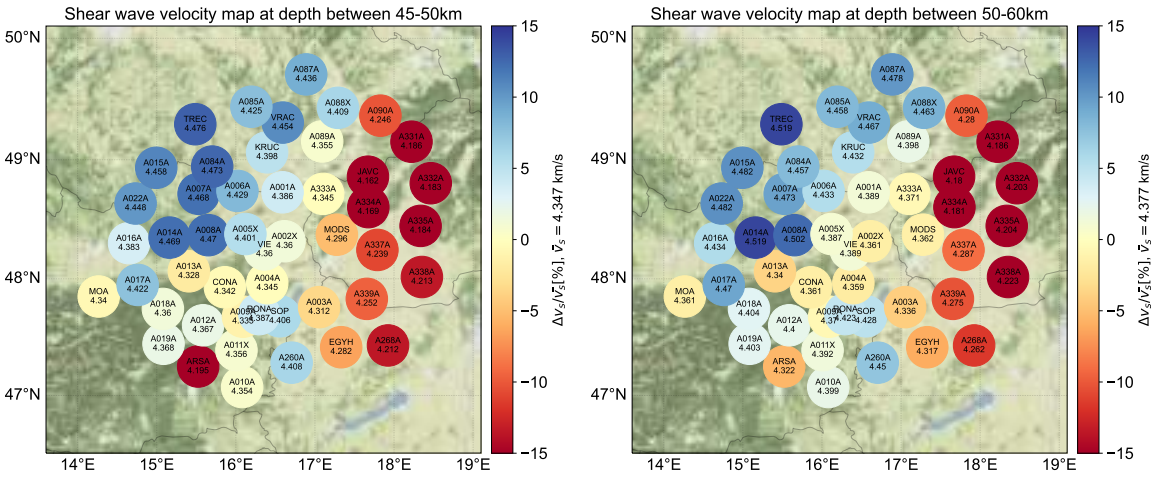
Shear wave velocity map at depth between 45-50km
Shear wave velocity map at depth between 50-60km
50°N
49°N
48°N
47°N
14°E
15°E
16°E
17°E
18°E
19°E
15
10
5
0
−5
−10
−15
$\Delta v_S/\bar{v}_S$[%], $\bar{v}_S$ = 4.347 km/s
$\Delta v_S/\bar{v}_S$[%], $\bar{v}_S$ = 4.377 km/s

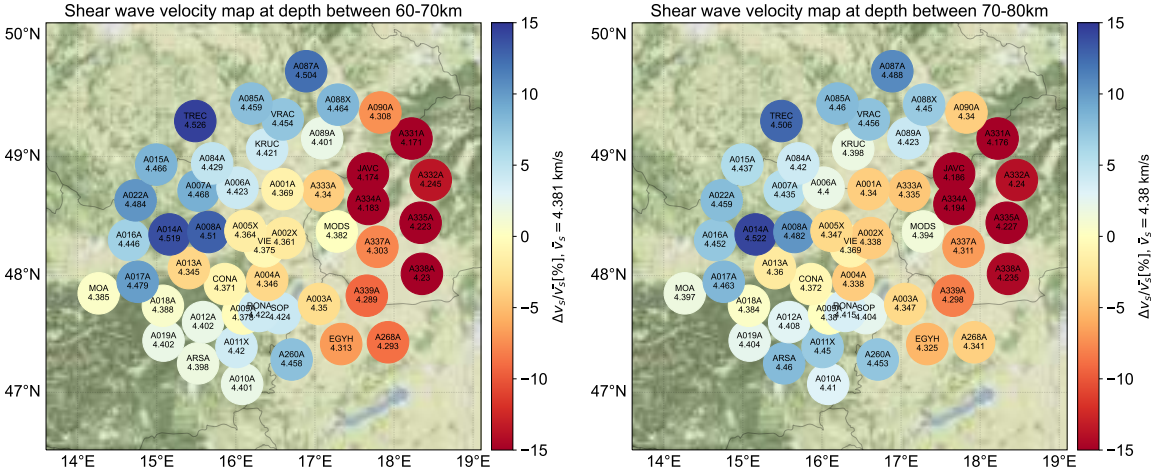
Shear wave velocity map at depth between 60-70km
Shear wave velocity map at depth between 70-80km
50°N
49°N
48°N
47°N
14°E
15°E
16°E
17°E
18°E
19°E
15
10
5
0
−5
−10
−15
$\Delta v_S/\bar{v}_S$[%], $\bar{v}_S$ = 4.381 km/s
$\Delta v_S/\bar{v}_S$[%], $\bar{v}_S$ = 4.38 km/s

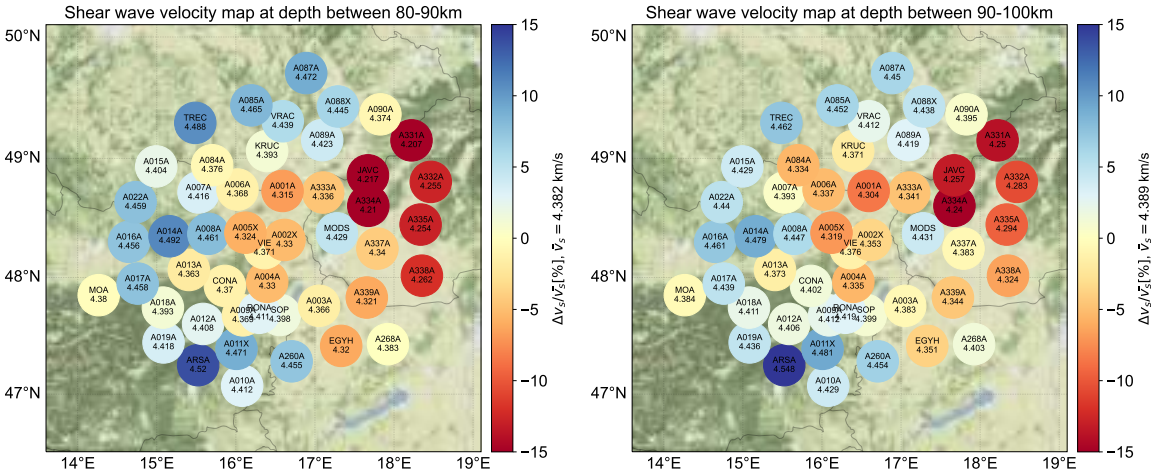
Shear wave velocity map at depth between 80-90km
Shear wave velocity map at depth between 90-100km
50°N
49°N
48°N
47°N
14°E
15°E
16°E
17°E
18°E
19°E
15
10
5
0
−5
−10
−15
$\Delta v_S/\bar{v}_S$[%], $\bar{v}_S$ = 4.382 km/s
$\Delta v_S/\bar{v}_S$[%], $\bar{v}_S$ = 4.389 km/s

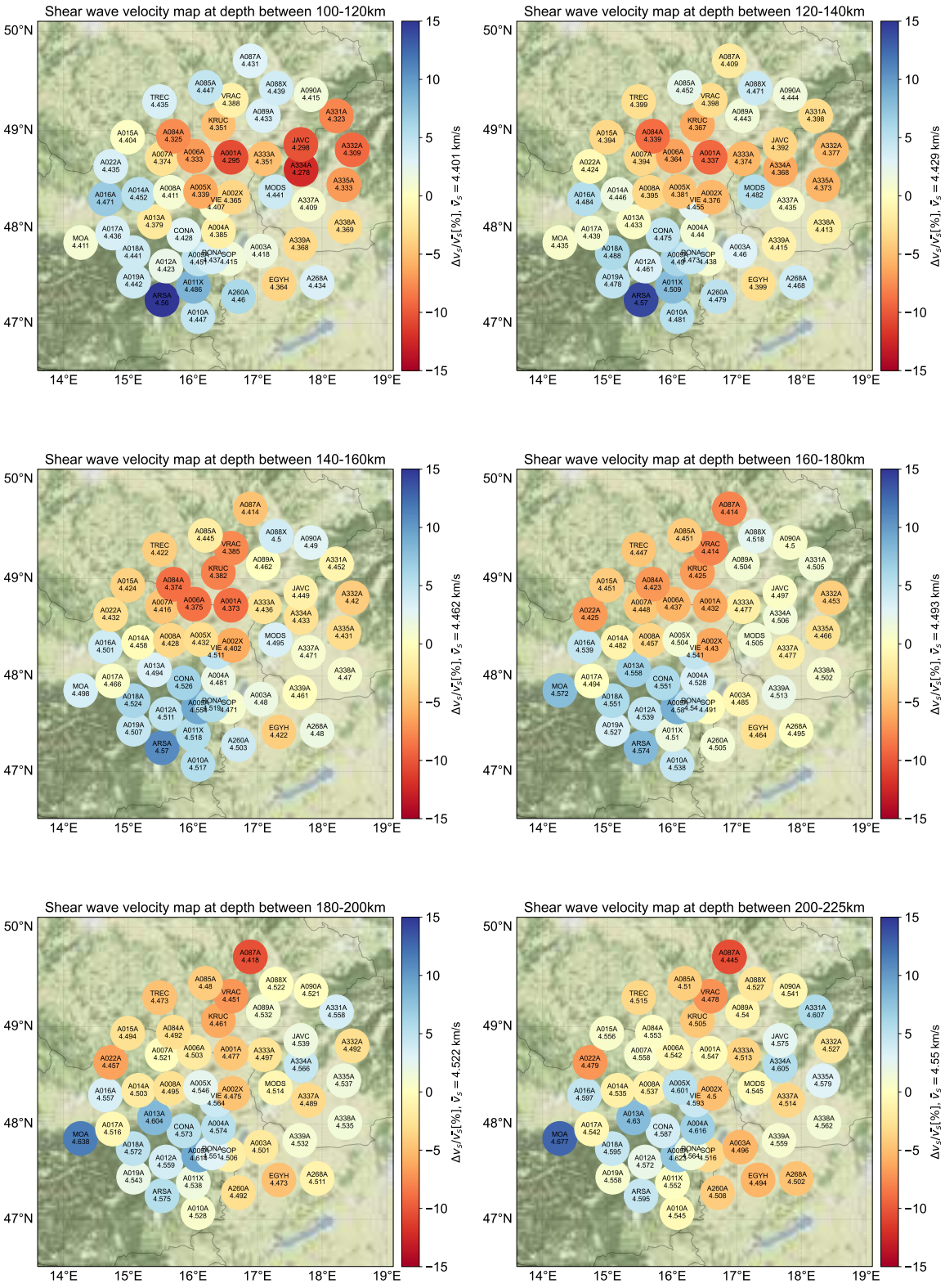
Shear wave velocity map at depth between 100-120km
Shear wave velocity map at depth between 120-140km
Shear wave velocity map at depth between 140-160km
Shear wave velocity map at depth between 160-180km
Shear wave velocity map at depth between 180-200km
Shear wave velocity map at depth between 200-225km
50°N
49°N
48°N
47°N
14°E
15°E
16°E
17°E
18°E
19°E
15
10
5
0
−5
−10
−15
$\Delta v_S/v_S$[%], $\bar{v}_S$ = 4.401 km/s
$\Delta v_S/v_S$[%], $\bar{v}_S$ = 4.429 km/s
$\Delta v_S/v_S$[%], $\bar{v}_S$ = 4.462 km/s
$\Delta v_S/v_S$[%], $\bar{v}_S$ = 4.493 km/s
$\Delta v_S/v_S$[%], $\bar{v}_S$ = 4.522 km/s
$\Delta v_S/v_S$[%], $\bar{v}_S$ = 4.55 km/s

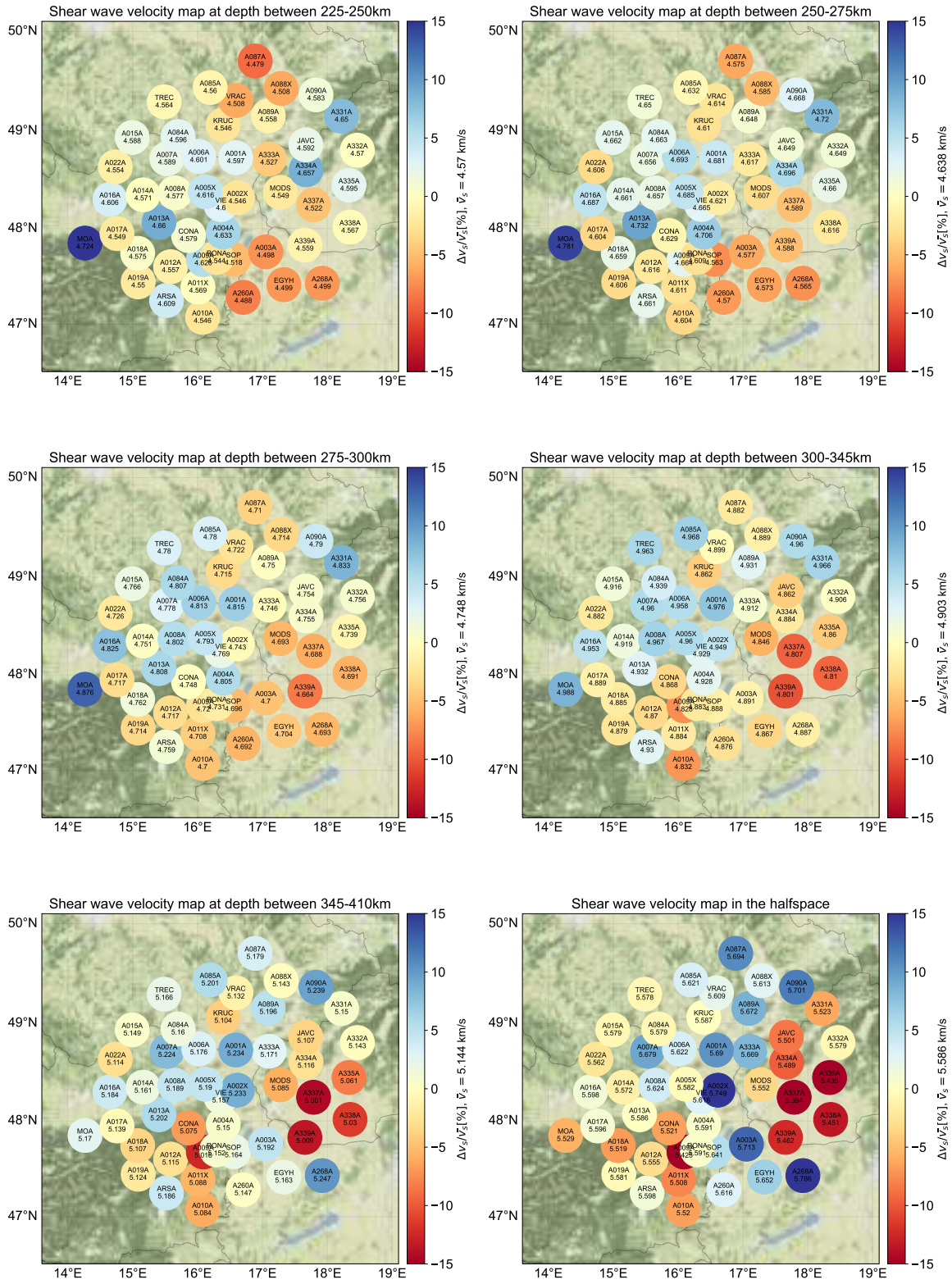

Figure 19. Shear-wave velocity maps plotted layer by layer over the geographical map of the wider Vienna Basin region. The scale is fixed for each layer. It reflects the velocity deviation at each subarray relative to the mean and is in percentage.

Chapter 5

Discussion

In the first section of this chapter, I would like to introduce the reader to my own observations and analysis of the obtained results. The 1-D shear-velocity models are discussed in depth. Next, the resolution of the current array-based study is compared to tomographic studies previously conducted in the wider Vienna Basin. Finally, I will compare my results to results obtained by other studies and see whether some of the observations can be attributed to distinct structures.

5.1 My results

It was observed that the 1-D structural models for all subarrays differed highly above 250km. Therefore, a zoom in those depths is presented in Figure 20. As already explained, each subarray was assigned to one of the 5 tectonic units located in the region of the wider Vienna Basin - Vienna Basin (yellow), Bohemian Massif (orange), Eastern Alps (violet), Carpathians (green) and the Little Hungarian Plain (blue). The 1-D models over the total depth range are shown in the last panel of Figure 21.

The most significant differences between the models are in the uppermost mantle between 50 and 100km, see Figure 20. One can clearly distinguish between 5 different tectonic units. The Carpathians are clearly way slower than the other tectonic units. This was also observed while looking at the merged phase velocity dispersion curves at periods below 70s (Figure 17). The Bohemian Massif and the Eastern Alps have the highest velocities in this depth range between 50 and 100km.

In the crust, there is not such prominent difference between the models. However, there is one subarray in the Alps for which velocity is relative slow compared to the others. Similarly, one subarray in the Bohemian Massif is significantly faster.

For depths below 100 km, one can still see some pattern. Especially visible is one model for a subarray in the Alps which differs significantly from all other tectonic units. Around 150-200km the Bohemial Massif becomes slower and the Alps dominate the higher velocities. Further below 225km no separation of the units can be done. This points to a relatively homogeneous layer. At this depths one can say that the waves are already trapped purely in the asthenosphere.

Now we can look at different tectonic units and compare the models to one another. Therefore, let's look at Figure 21 which shows each unit with it's respective color. The last panel shows all of them together.

Looking at crustal depths, all units have steep gradients, meaning shear-wave velocity changes significantly with depth. However, there is no striking difference in the velocity distribution.

Looking at the models for subarrays in the Vienna Basin, a low-velocity zone is to be seen between 50 and 100km. A similar zone is observed in the Bohemian Massif. However, right below the Moho the velocity is high. The low-velocity zone is deeper and extends to

almost 200km depth. Vienna Basin and the Bohemian Massif are the only regions with such low-velocity anomaly.

The shear-wave velocity under the Alps does not change abruptly between the Moho and 250km. However, the gradient gets steeper below and a distinct step in velocity can be observed at 410km. This represents the upper boundary of the mantle transition zone.

The Carpathians show a steep gradient at all depths. Just like in the Alps, there is a distinct change in velocity at the 410-boundary. Interesting to see is the model for one subarray which at depths between 50 and 100km is significantly faster than the rest. The reason behind might be that the subarray reaches some other different unit.

The models of the Little Hungarian Plain and the Alps appear to be very similar. However, the shear-wave velocity in the Little Hungarian Plain is generally lower above 300km. Deeper they appear comparable.

By looking at all models - individual or all together, one can conclude that they are clearly distinguishable. The array method in combination with the inversion is capable to resolve different tectonic units. Subarrays belonging to the same tectonic region appear to have very similar structural models. Exception is one subarray in the Carpathians which might be reaching some other tectonic unit.

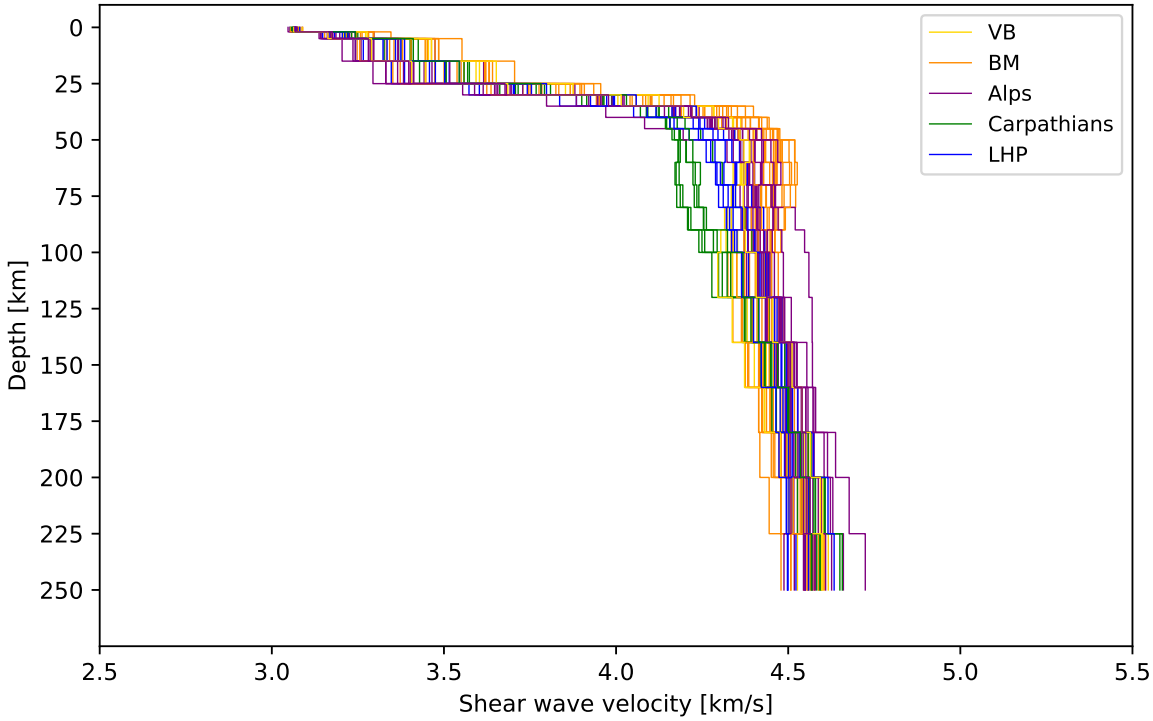

Figure 20. All 1-D shear-wave velocity models in depths up to 250km. Colors reflect the different tectonic units.

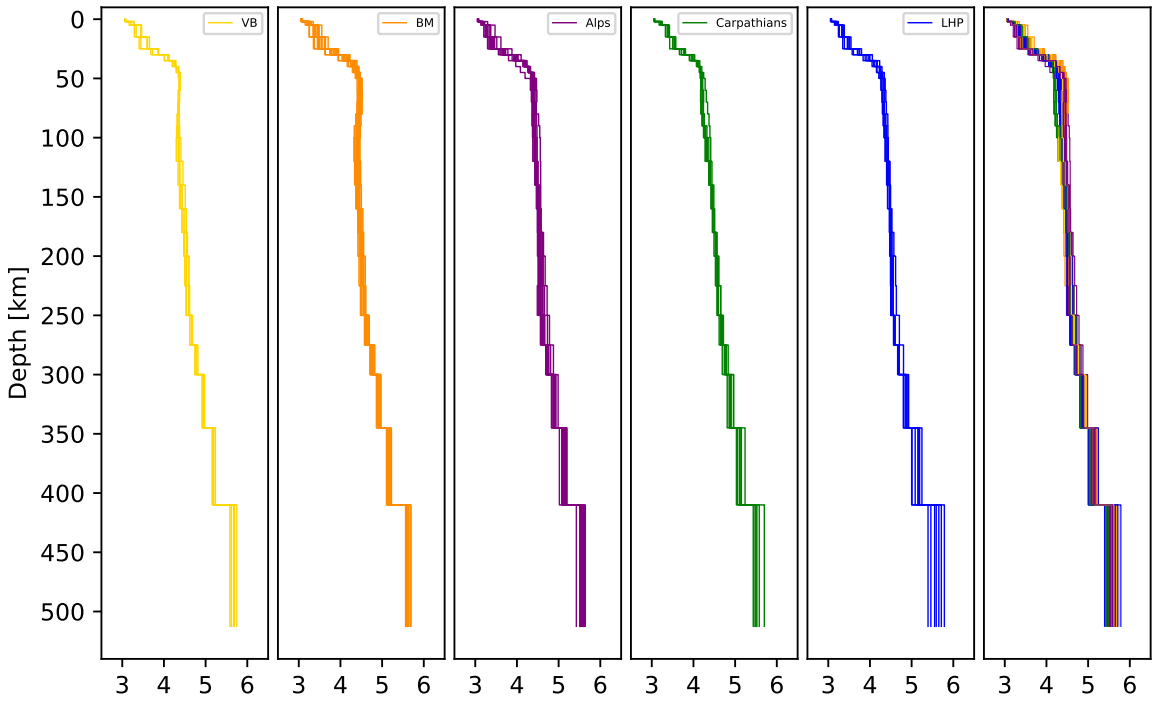

Figure 21. 1-D shear-wave velocity models with depth at subarrays corresponding to one of the five tectonic units in the studied region - Vienna Basin (BV; yellow), Bohemian Massif (BM; orange), Eastern Alps (violet), Carpathians (green) and Little Hungarian Plain (LHP; blue). Last panel displays all 1-D models together.

5.2 Resolution comparison

I would like to start by pointing out that I did not perform a proper resolution testing. The array method, in the sense that I have used it, is relatively new and I have not yet established a technique how to evaluate its resolution capability. However, the lateral resolution would be constrained by the aperture of the subarrays and the distance between each one of them.

It is true that the phase velocity measurement for an individual subarray is averaged over a region with diameter of 160km. However, the individual subarrays are around 50km away from one another. In fact, the regions over which the measurements are averaged overlap to great extend.

To further elaborate here, I would refer the reader to the shear-wave velocity maps discussed earlier, Figure 19. Let's look at subarray ARSA at depth around 100-120km. The velocity at this depth is relatively high compared to its neighbors. First, the subarray has an aperture of around 160km. However, it's four neighbors are at a distance around 50km. This means that towards the inside of the region, the five subarrays would "see" the same structure. This implies that the high velocity under ARSA is more towards southwest rather than northeast. Moreover, I would suspect that an anomaly with size around 100 km can be potentially resolved. Of course, those are only speculations and I do not claim any accuracy.

The vertical resolution depends more on the period range of the phase velocity dispersion curves than on the array design. As noted, short period surface waves feel the more shallow

depths and longer waves are more sensitive to deeper layers. The period range of the phase velocities in my study did not extend to very short periods, therefore, the shear-velocity at crustal depths would not be very reliable. The same applies to greater depths. Therefore, I focus mostly on the upper mantle.

Dando et al. 2011 calculated a teleseismic body-wave tomography to image the Carpathian-Pannonian region in the Central Alps. They estimated the resolution capability of their model both for P and S-waves using checkerboard tests. The results show that an anomaly with size of 100 km in lateral direction would be "seen" by the shear waves propagation. However, vertically the velocity anomalies are rather smeared. The resolution is rather high for the size of their region and is comparable with the approximated resolution of my array method.

Kästle et al. 2020 discuss both body wave and surface wave tomographic studies of the upper mantle in the Alpine subduction zone. All studies include my region of investigation. The resolution of the different models is not discussed in depth. However, by looking at the results, it is clearly visible that small heterogenities in the Vienna Basin cannot be properly resolved. The velocity over the whole region appears smeared and relatively constant.

5.3 Results comparison

El-Sharkawy et al. 2020 calculated a Rayleigh wave tomography for the Alpine-Mediterranean region. They obtained 3-D shear-velocity maps down to 300km depth. The region they image is quite broad and small local complexities would not be resolved. However, some similarities with my study were prominent. They image a high-velocity extension from the Dinarides towards the Eastern Alps. This coincides with the southwest edge of my region. El-Sharkawy et al. 2020 suggest an Adriatic slab beneath the Eastern Alps down to depths of 150km. If one looks at Figure 19 at depths around 100 to 160km, it is visible that station ARSA is a high-velocity anomaly in the local region of the Eastern Alps. This suggests that the structure beneath the subarray is subjected to the subduction processes in the Eastern Alps.

Dando et al. 2011 conducted a tomographic study based on body waves. They discuss both P and S-wave velocity maps to depths around 800km. As I worked with Rayleigh waves, it only makes sense to compare my shear-wave velocity results with theirs. They imaged the Carpathian-Pannonian region which fully includes the wider Vienna Basin. Looking at 75km depth there are many similarities between our results. The Carpathians are shown to be slow and going towards the Vienna Basin velocities gradually increase. The Bohemian Massif together with the southern part of the Eastern Alps appear to be relatively faster. At greater depths around 200-300km subarray MOA is apparently faster than its surroundings. In Dando et al. 2011 this region of the Eastern Alps is also imaged as a high velocity zone.

Chapter 6

Final remarks

6.1 Conclusions

This thesis deals with phase velocity measurements of Rayleigh wave fundamental mode and their inversion for depth. A new approach for obtaining structural information of a local region is presented. Array measurements are a common technique for measuring phase velocity dispersion curves of surface waves. However, usually individual subarrays are used for obtaining local 1-D structure.

The dense AlpArray network allowed for forming many subarrays over the region of the wider Vienna Basin, located at the edge of the Eastern Alps. Phase velocity dispersion curves are calculated using the array approach. The technique is based on the two-station method combined with beamforming. Waveforms of the fundamental mode are cross-correlated at station pairs and so their propagation time is determined. Using linear regression, the phase velocity and arrival angle of the fundamental mode is obtained. For every subarray, many phase velocity dispersion curves are calculated and then merged. The averaged dispersion curves for each subarray are then inverted for depth and 1-D shear-wave velocity models are obtained. Those provide a quasi 3-D velocity distribution with depth beneath the area of investigation. The obtained results show that the array approach is reliable for distinguishing different tectonic units in the region of the wider Vienna Basin.

6.2 Outlook

While working on the topic of my thesis, new ideas for further research emerged. It would be interesting to investigate different array sizes and compare the results. The phase velocity dispersion curves experience higher wobbles in case of smaller instestation distances. This applies to the arrival angle deviations as well. I would like to investigate whether the merging technique still provides reliable results for curves with higher phase velocity deviations along the whole period range, if smaller array aperture is used.

As mentioned in the chapters above, the two horizontal components of all records were downloaded and pre-processed together with the vertical. This was initially done so that in the future the study can be carried out with Love waves as well. This would allow to further study the well-known discrepancy in the propagation velocities of Love and Rayleigh waves.

Another future topic would be working out a way to estimate the resolution capability of the array method presented. Currently, there is no proper technique developed due to the fact that the idea of "floating" subarrays is relatively new. However, even now, one can still roughly estimate the approximate resolution.

Appendix

A.1 Record plots

In Figure 2 I showed one earthquake recorded on the vertical component. The figure corresponds to Mexico earthquake (2017-09-08) with magnitude 8.2. Here the other 35 events are displayed ordered ascending in time. More details about each earthquakes are listed in Table 3.

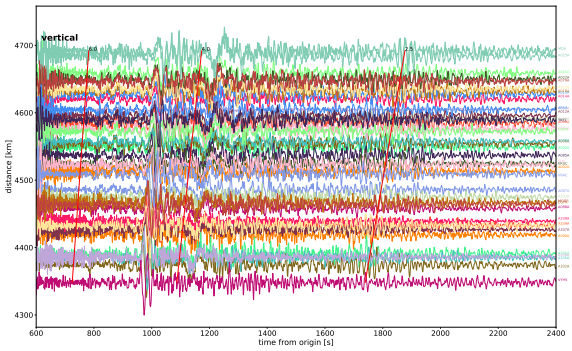

Figure A.1. Afghanistan, M=7.5

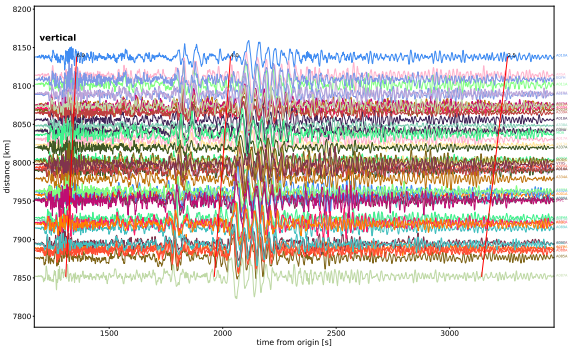

Figure A.2. Alaska, M=7.1

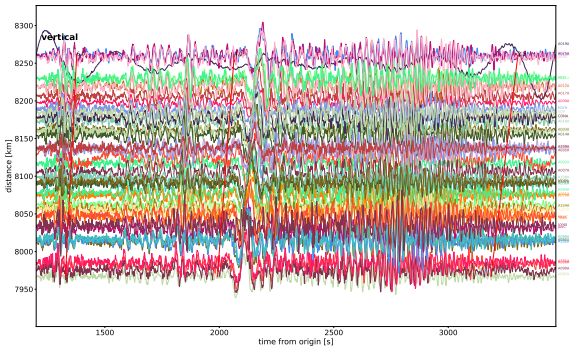

Figure A.3. Kamchatka, M=7.2

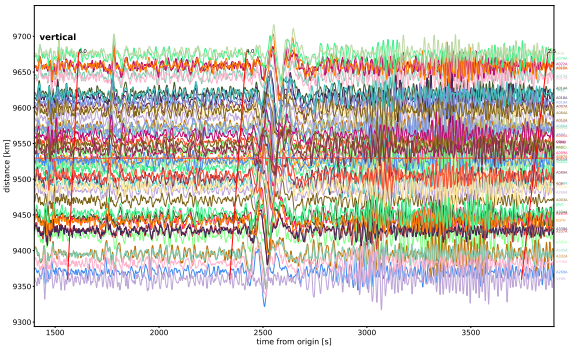

Figure A.4. Sumatra, M=7.8

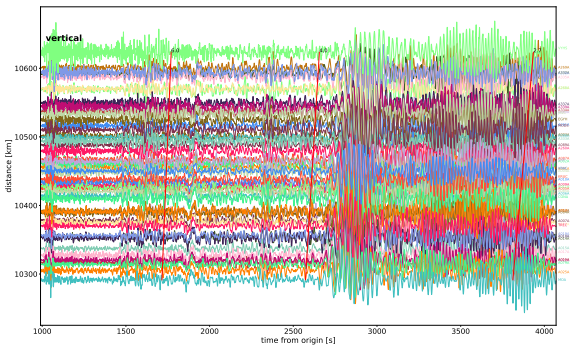

Figure A.5. Ecuador, M=7.8

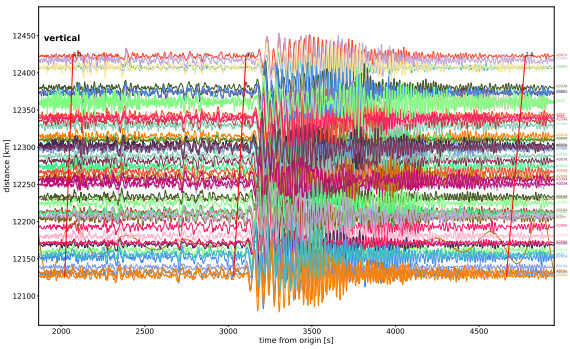

Figure A.6. South Atlantic, M=7.2

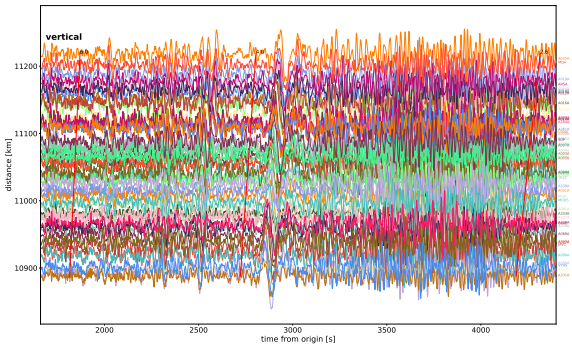

Figure A.7. Mariana, M=7.7

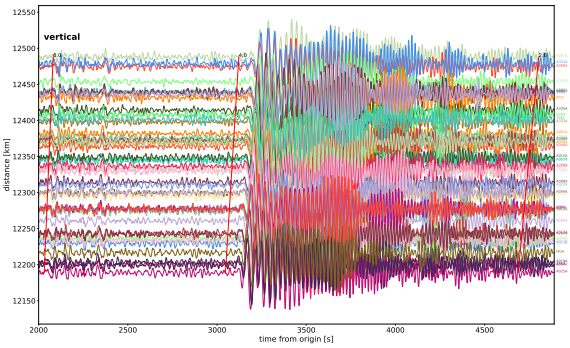

Figure A.8. South Atlantic, M=7.4

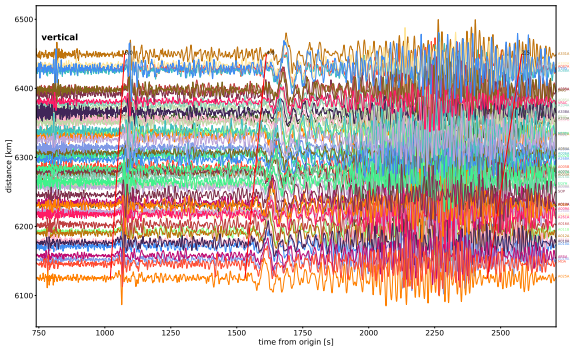

Figure A.9. Ascension, M=7.1

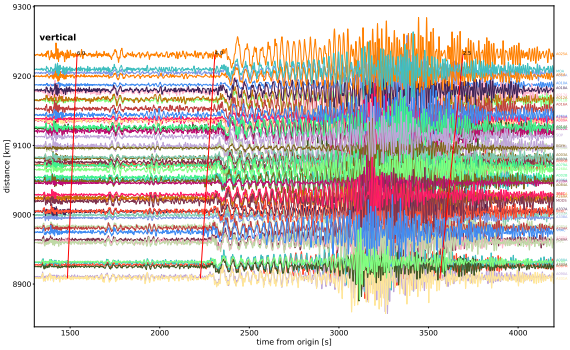

Figure A.10. Japan, M=6.9

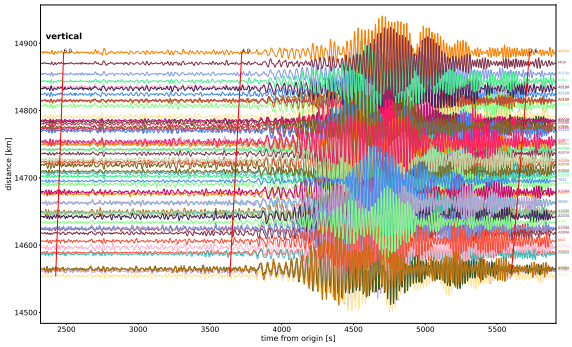

Figure A.11. Solomon, M=7.8

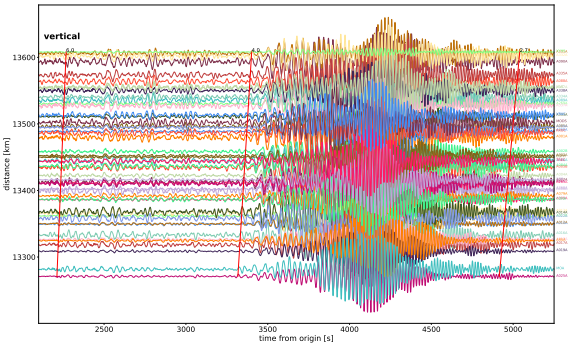

Figure A.12. Chile, M=7.6

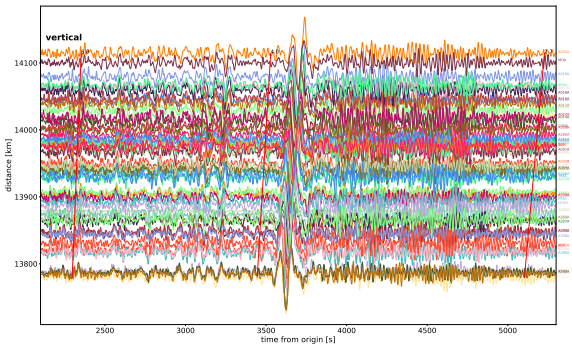

Figure A.13. Papua, M=7.9

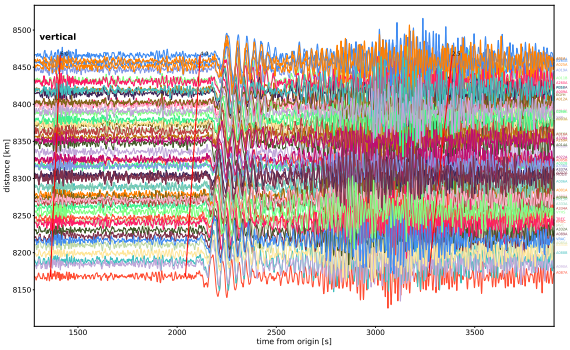

Figure A.14. Komandorskiye, M=7.7

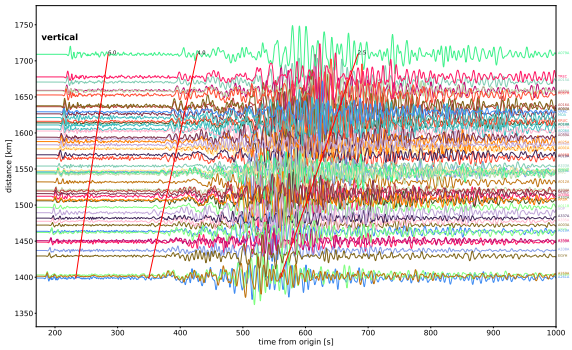

Figure A.15. Kos, M=6.6

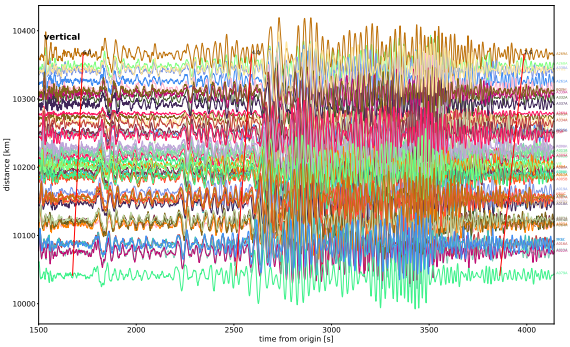

Figure A.16. Mexico, M=7.1

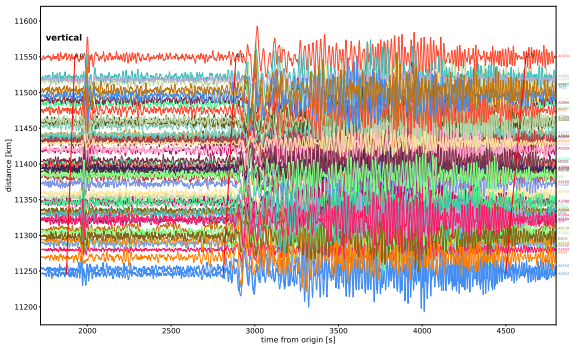

Figure A.17. Bouvet, M=6.7

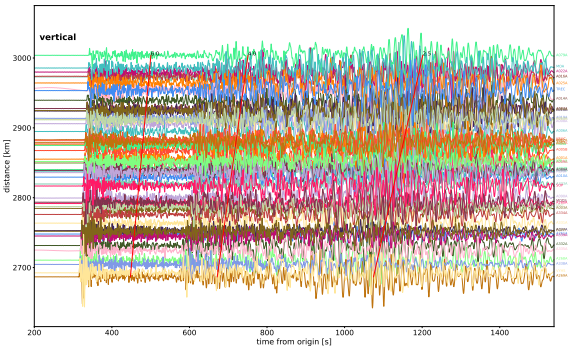

Figure A.18. Iraq, M=7.3

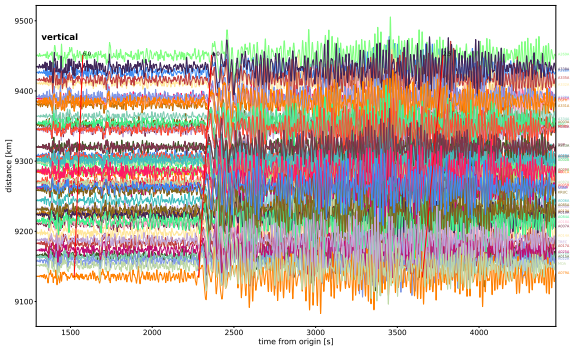

Figure A.19. Honduras, M=7.5

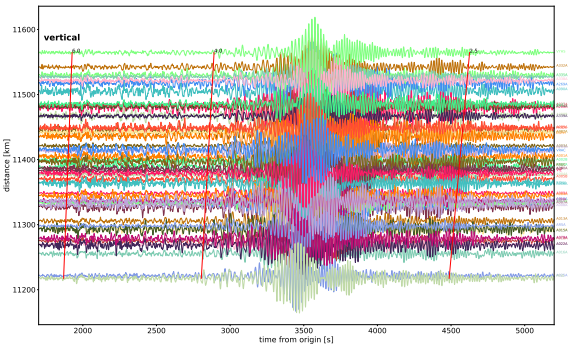

Figure A.20. Peru, M=7.1

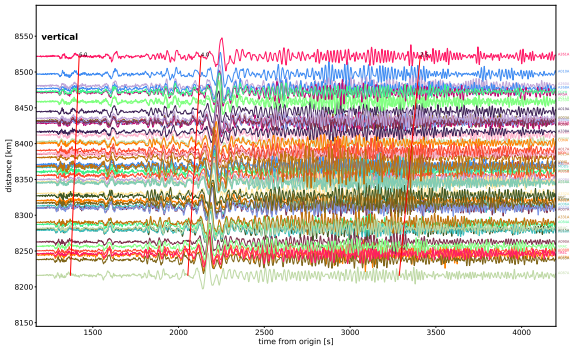

Figure A.21. Alaska, M=7.9

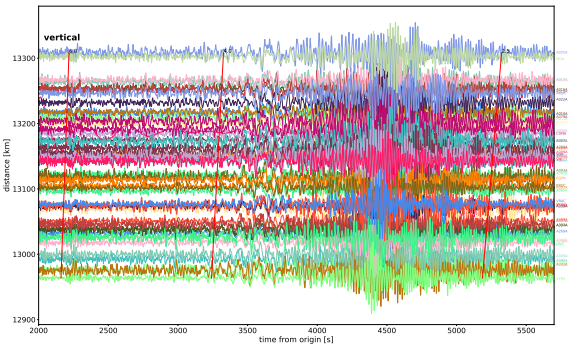

Figure A.22. Papua, M=7.5

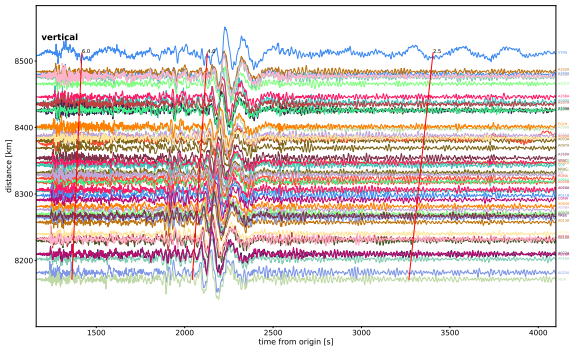

Figure A.23. Venezuela, M=7.3

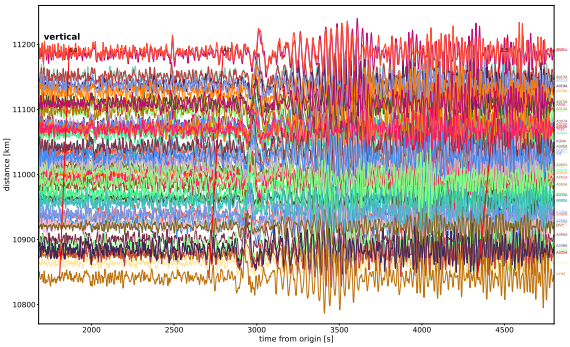

Figure A.24. Indonesia, M=7.5

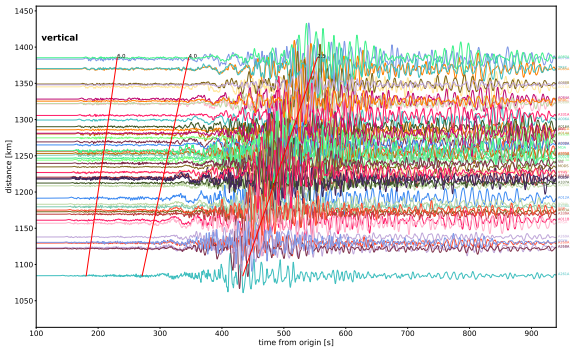

Figure A.25. Greece, M=6.8

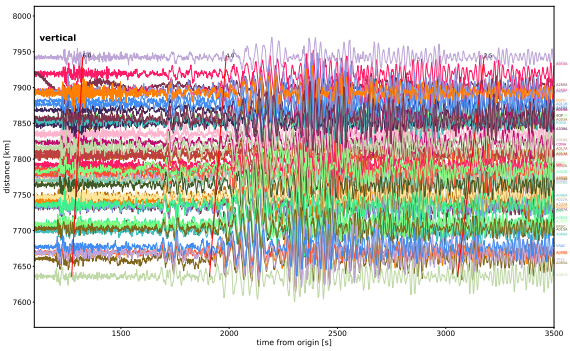

Figure A.26. Alaska, M=7.1

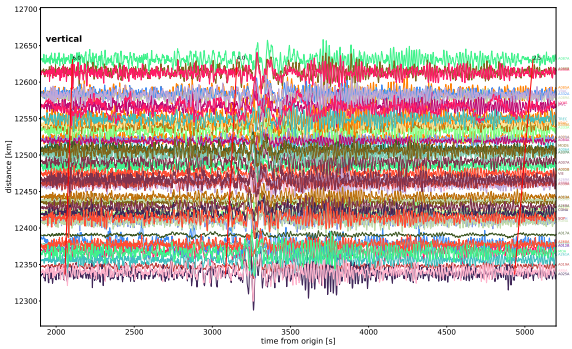

Figure A.27. South Atlantic, M=7.1

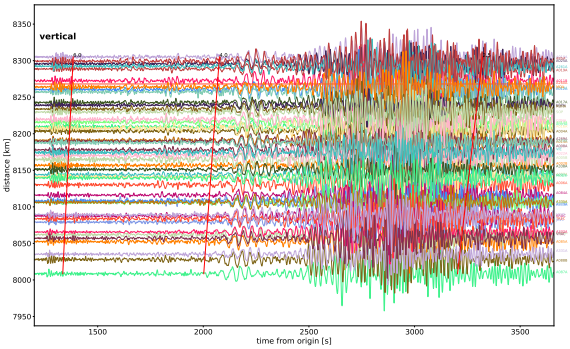

Figure A.28. Komandorskiye, M=7.3

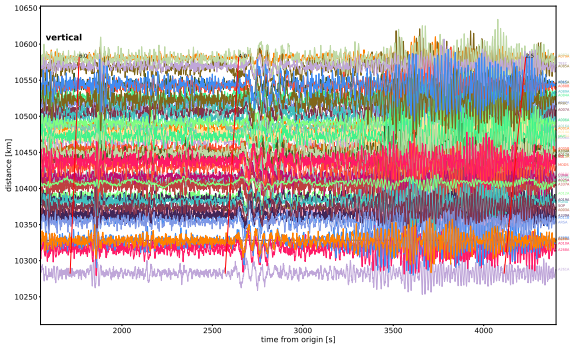

Figure A.29. Prince Edward, M=6.7

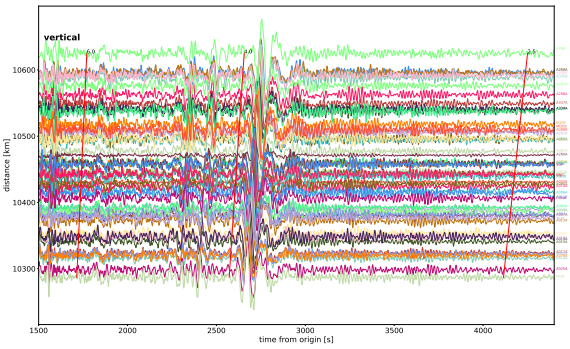

Figure A.30. Ecuador, M=7.5

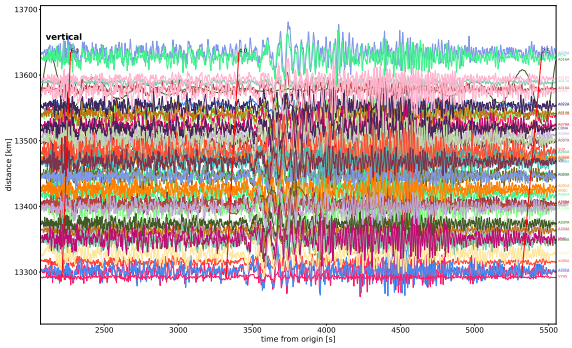

Figure A.31. Papua, M=7.1

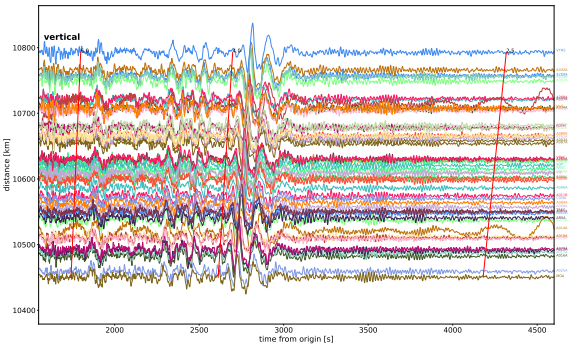

Figure A.32. Peru, M=8.0

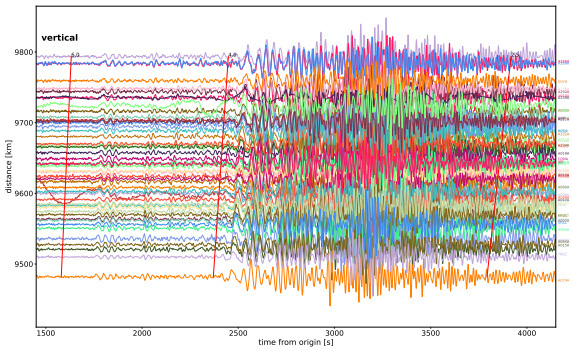

Figure A.33. California, M=7.1

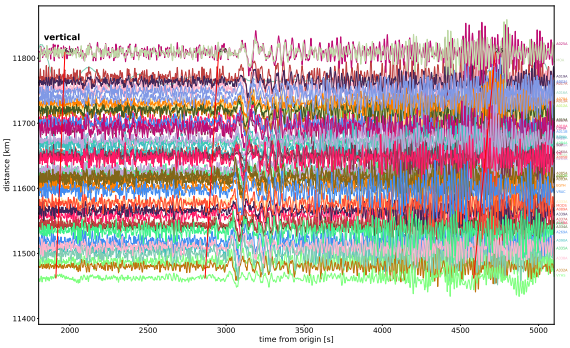

Figure A.34. Indonesia, M=7.2

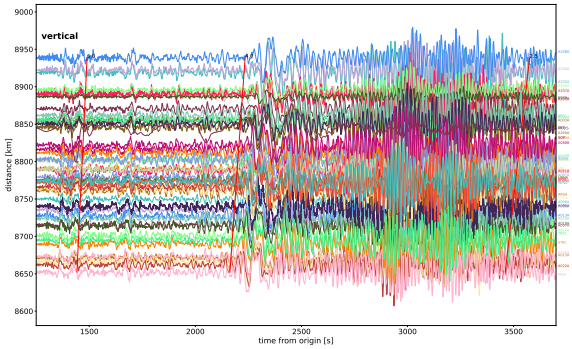

Figure A.35. Jamaica, M=7.7

A.2 Phase velocity dispersion curves

In Figure 13 measured phase velocity dispersion curves from different earthquakes at the subarrays CONA and A339A are displayed. Here I show the results for the rest 46 subarrays. Phase velocity, (arrival) angle deviation and residuals are plotted over the whole period range. Black dotted curve in panel 4 presents the merged curve with its standard deviation at each period. The y-axis ranges are fixed for all figures.

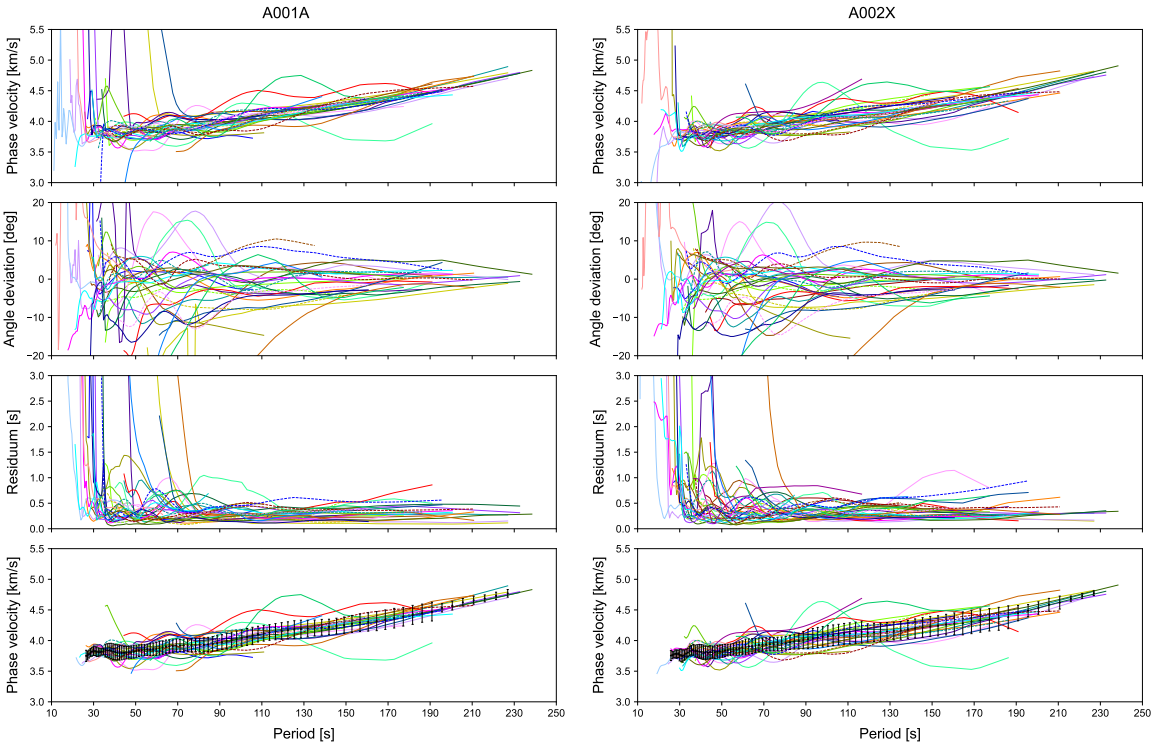
A001A
A002X
Phase velocity [km/s]
Angle deviation [deg]
Residuum [s]
Phase velocity [km/s]
Period [s]

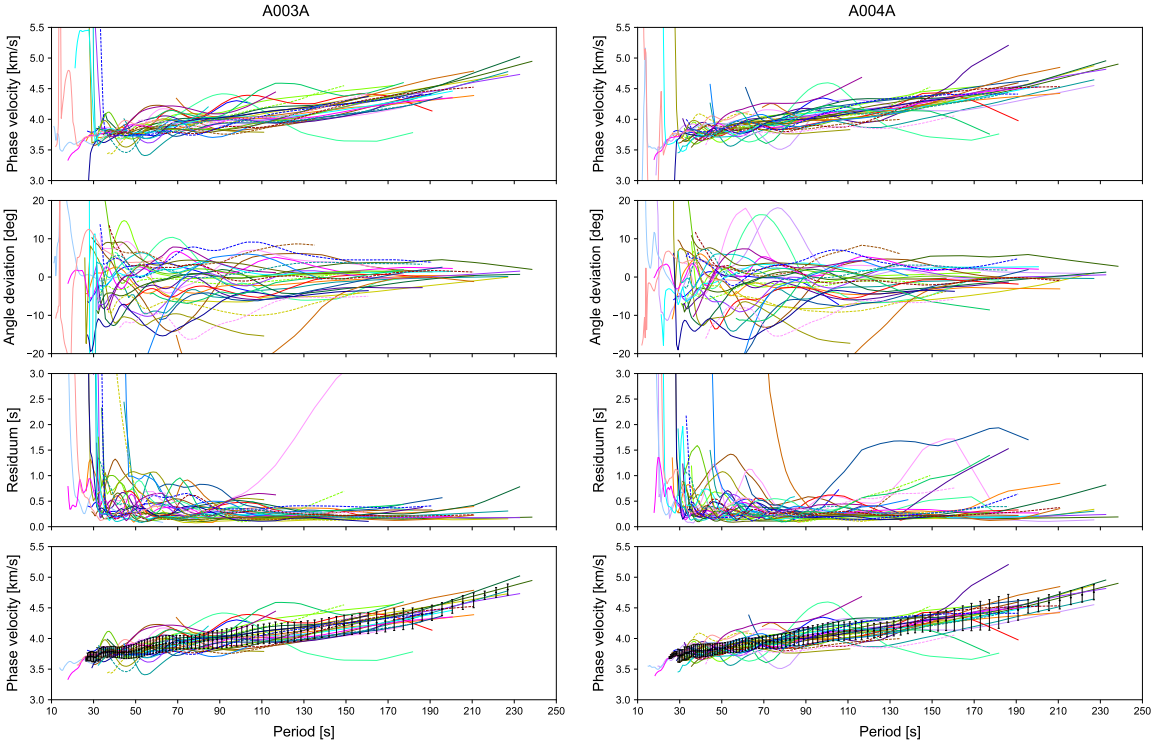
A003A
A004A
Phase velocity [km/s]
Angle deviation [deg]
Residuum [s]
Phase velocity [km/s]
Period [s]

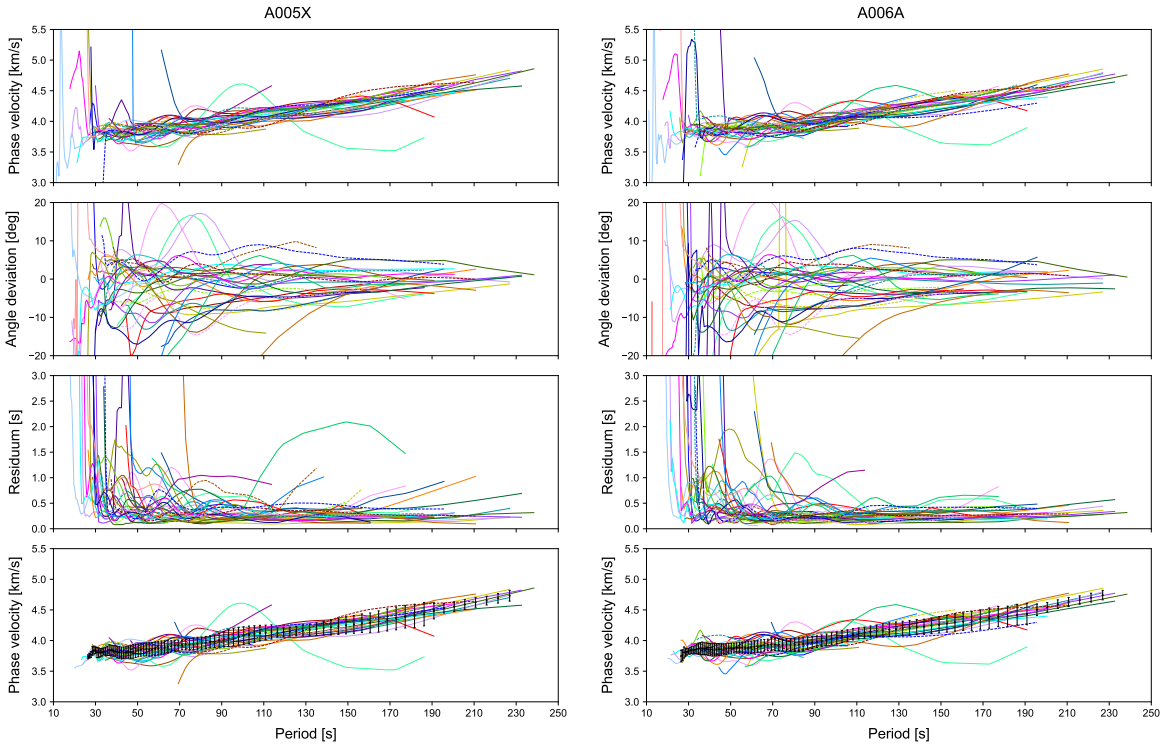
A005X
A006A
Phase velocity [km/s]
Angle deviation [deg]
Residuum [s]
Phase velocity [km/s]
Period [s]

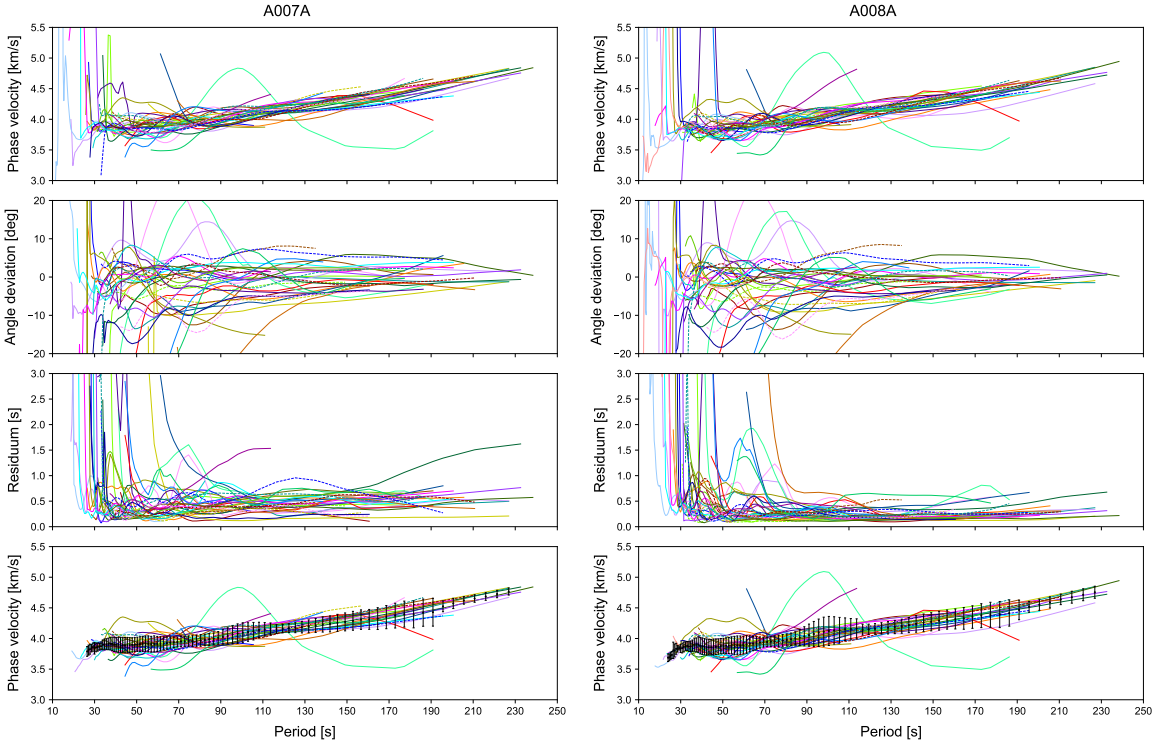
A007A
A008A
Phase velocity [km/s]
Angle deviation [deg]
Residuum [s]
Phase velocity [km/s]
Period [s]

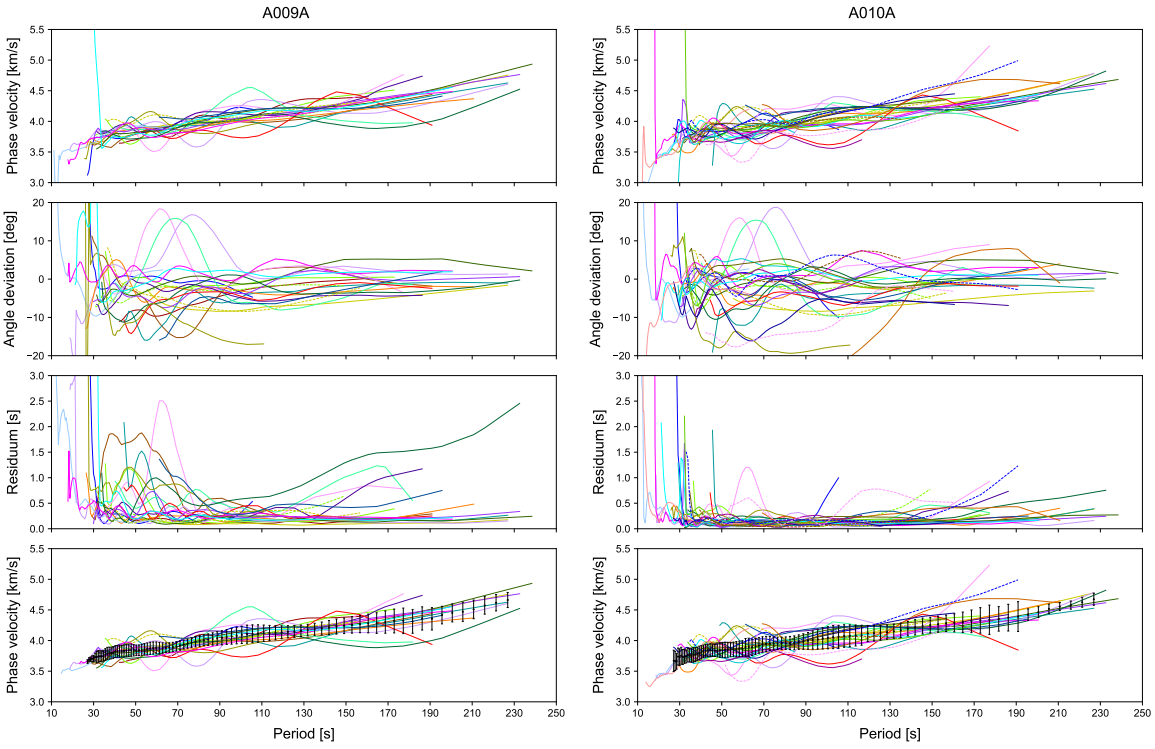
A009A
A010A
Phase velocity [km/s]
Angle deviation [deg]
Residuum [s]
Phase velocity [km/s]
Period [s]

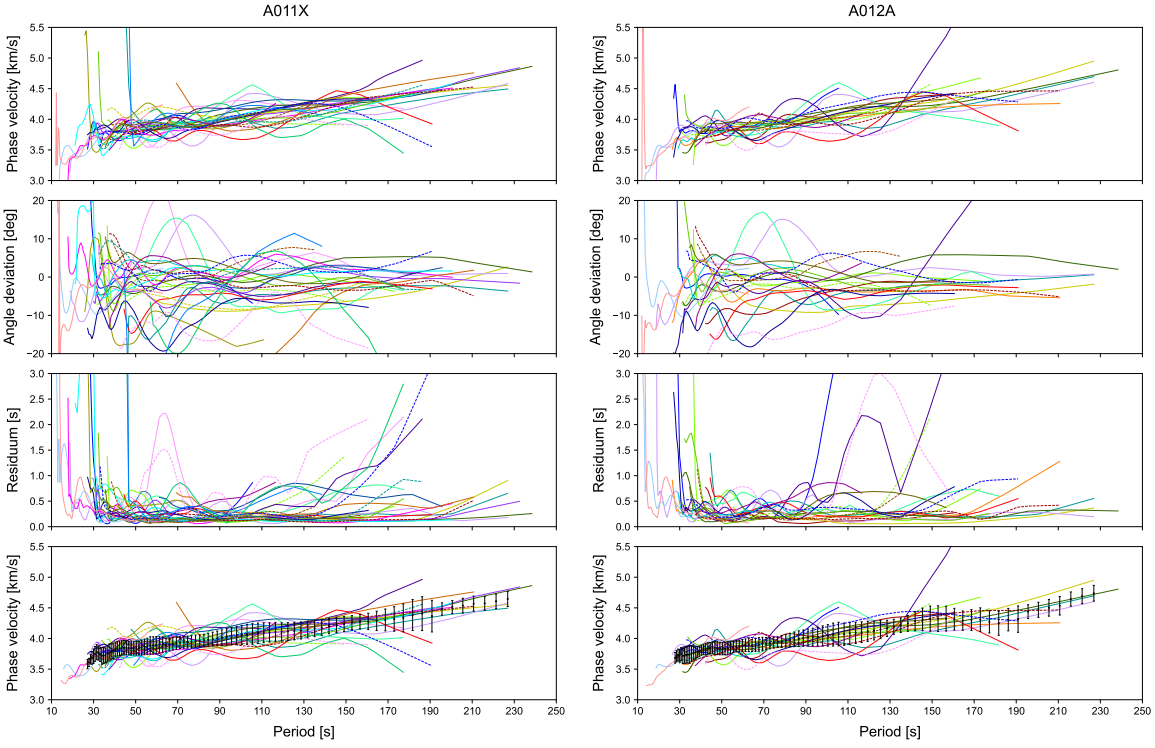
A011X
A012A
Phase velocity [km/s]
Angle deviation [deg]
Residuum [s]
Phase velocity [km/s]
Period [s]

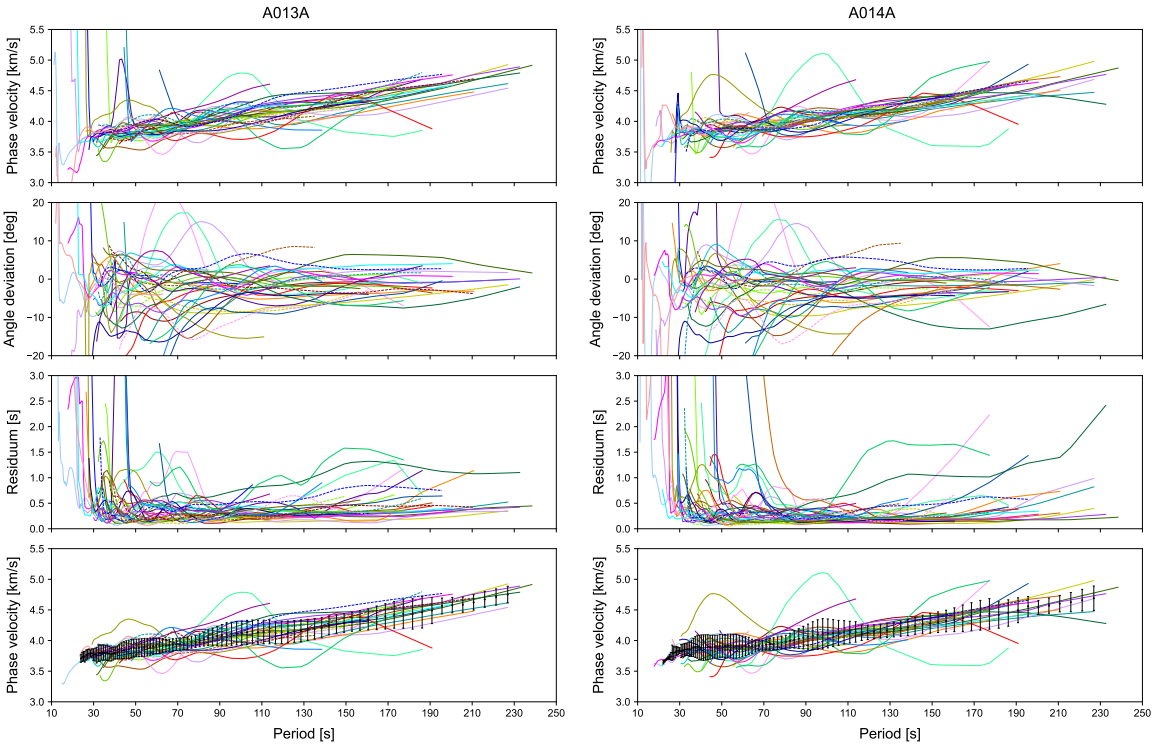
A013A
A014A
Phase velocity [km/s]
Angle deviation [deg]
Residuum [s]
Phase velocity [km/s]
Period [s]

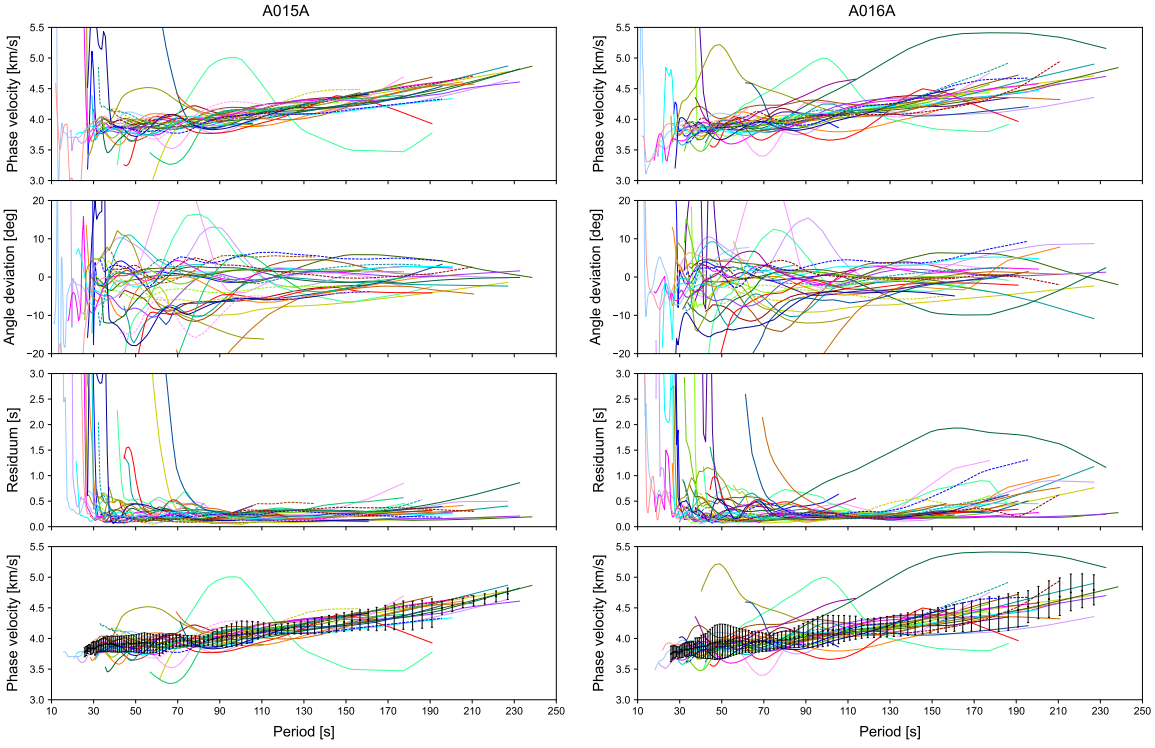
A015A
A016A
Phase velocity [km/s]
Angle deviation [deg]
Residuum [s]
Phase velocity [km/s]
Period [s]

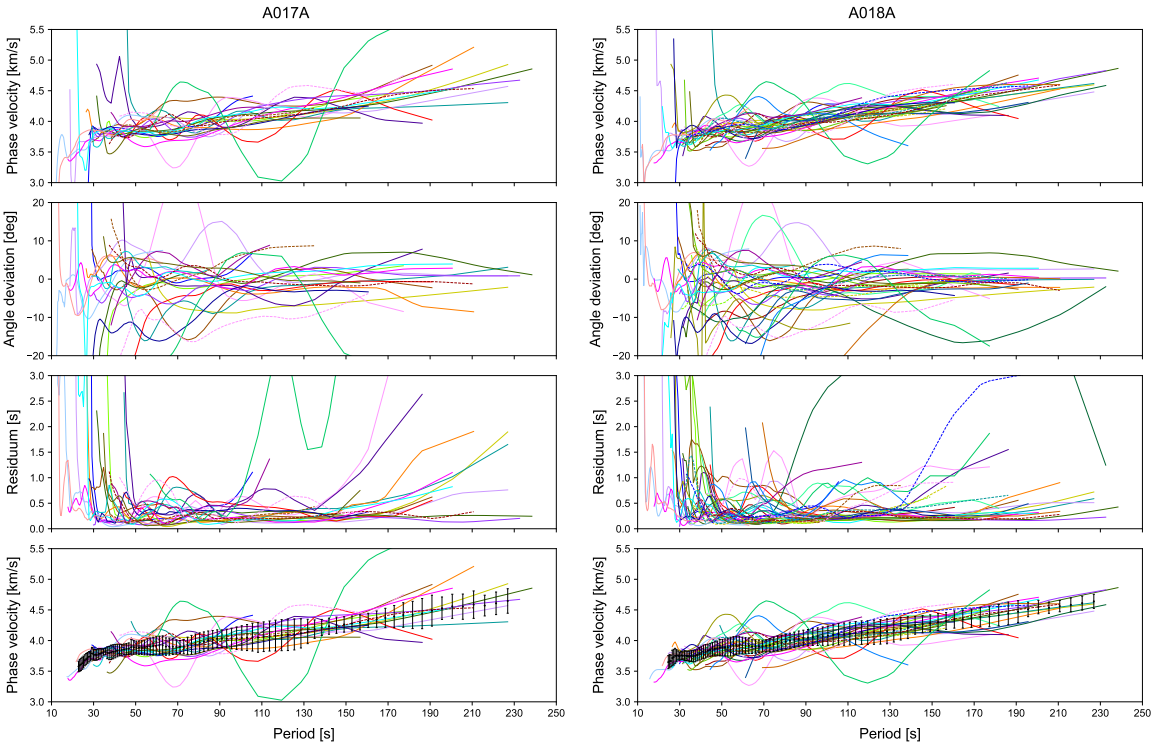
A017A
A018A
Phase velocity [km/s]
Angle deviation [deg]
Residuum [s]
Phase velocity [km/s]
Period [s]

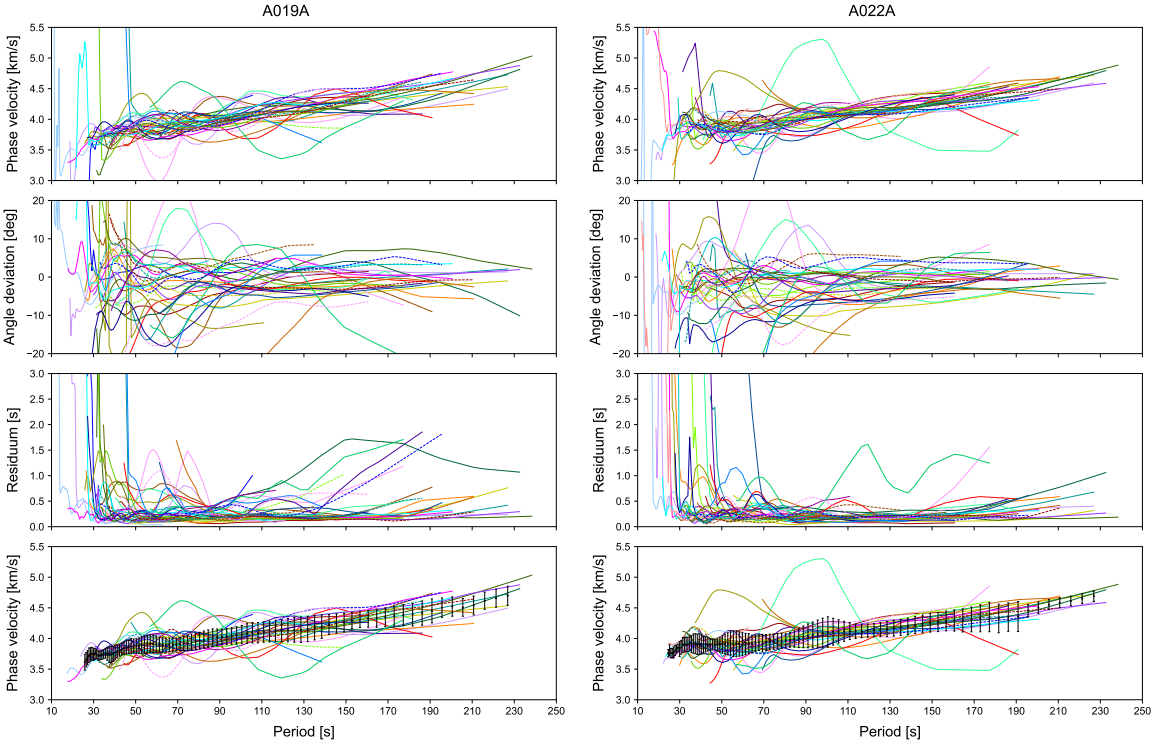
A019A
A022A
Phase velocity [km/s]
Angle deviation [deg]
Residuum [s]
Phase velocity [km/s]
Period [s]

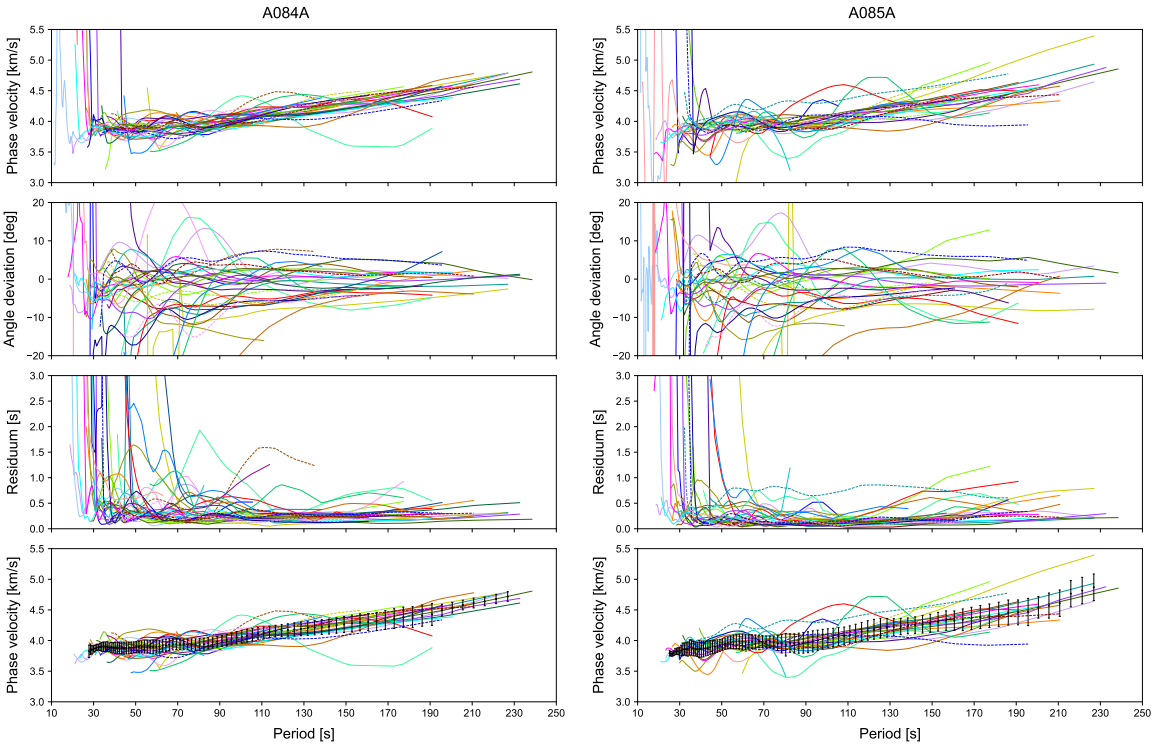
A084A
A085A
Phase velocity [km/s]
Angle deviation [deg]
Residuum [s]
Phase velocity [km/s]
Period [s]

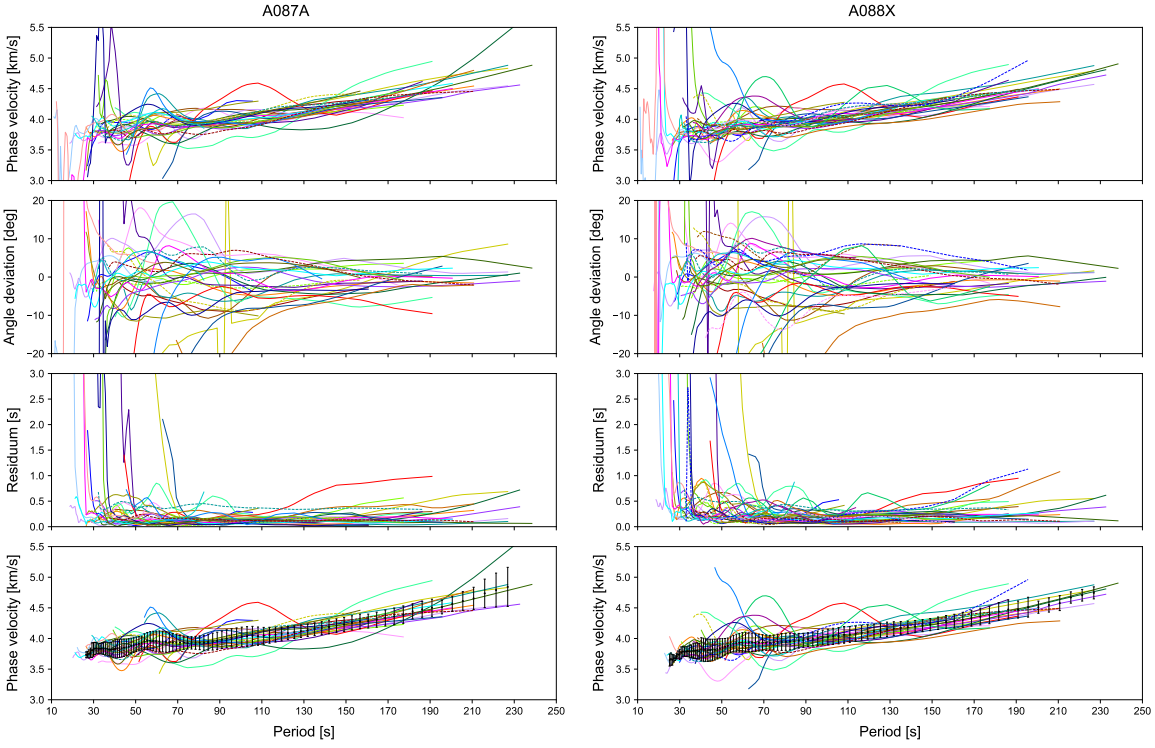
A087A
A088X
Phase velocity [km/s]
Angle deviation [deg]
Residuum [s]
Phase velocity [km/s]
Period [s]

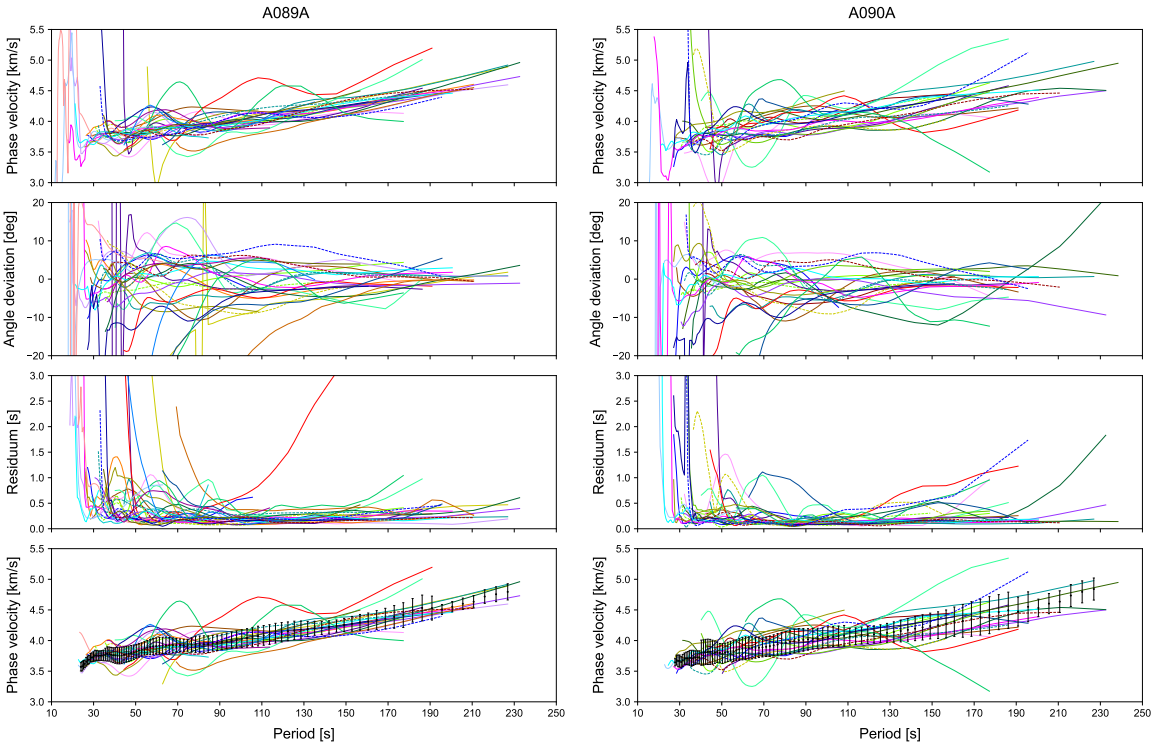
A089A
A090A
Phase velocity [km/s]
Angle deviation [deg]
Residuum [s]
Phase velocity [km/s]
Period [s]

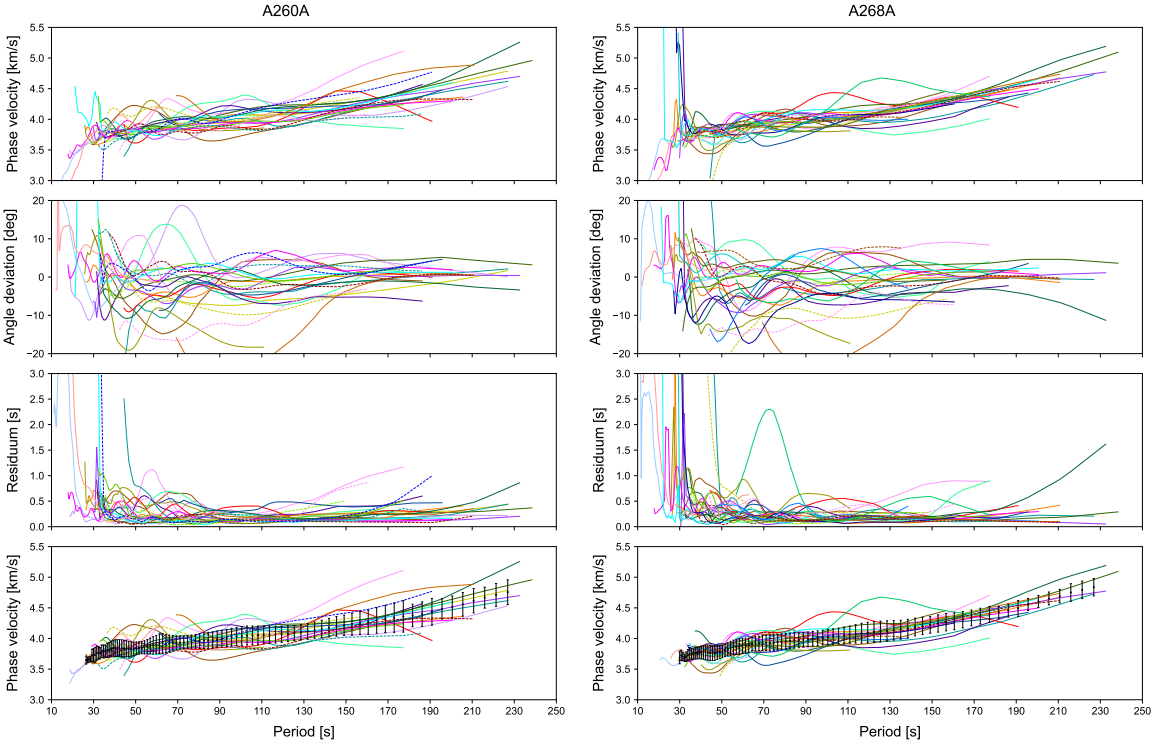
A260A
A268A
Phase velocity [km/s]
Angle deviation [deg]
Residuum [s]
Phase velocity [km/s]
Period [s]

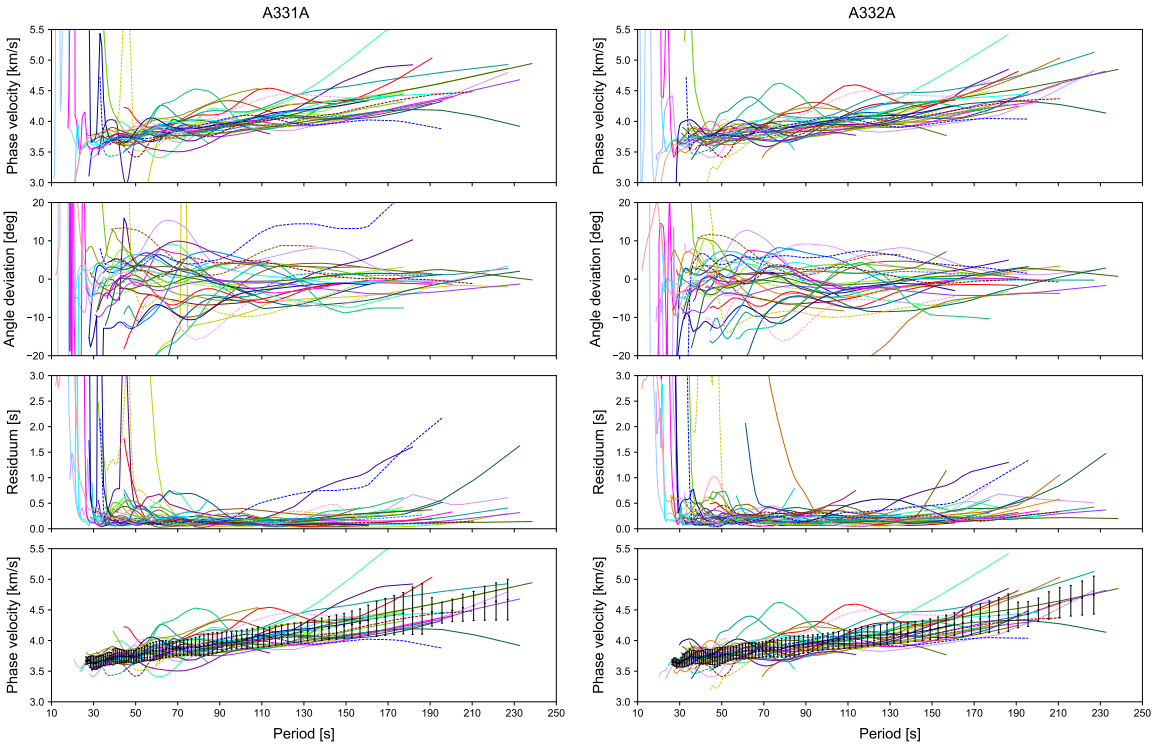
A331A
A332A
Phase velocity [km/s]
Angle deviation [deg]
Residuum [s]
Phase velocity [km/s]
Period [s]

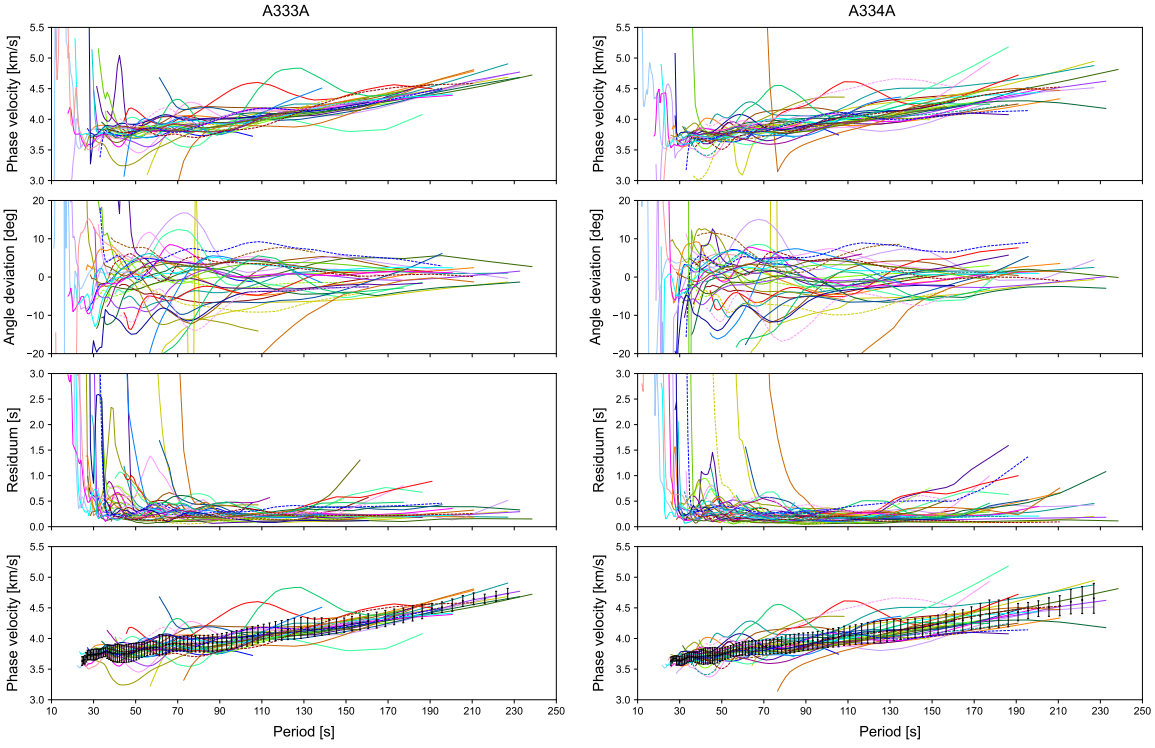
A333A
A334A
Phase velocity [km/s]
Angle deviation [deg]
Residuum [s]
Phase velocity [km/s]
Period [s]

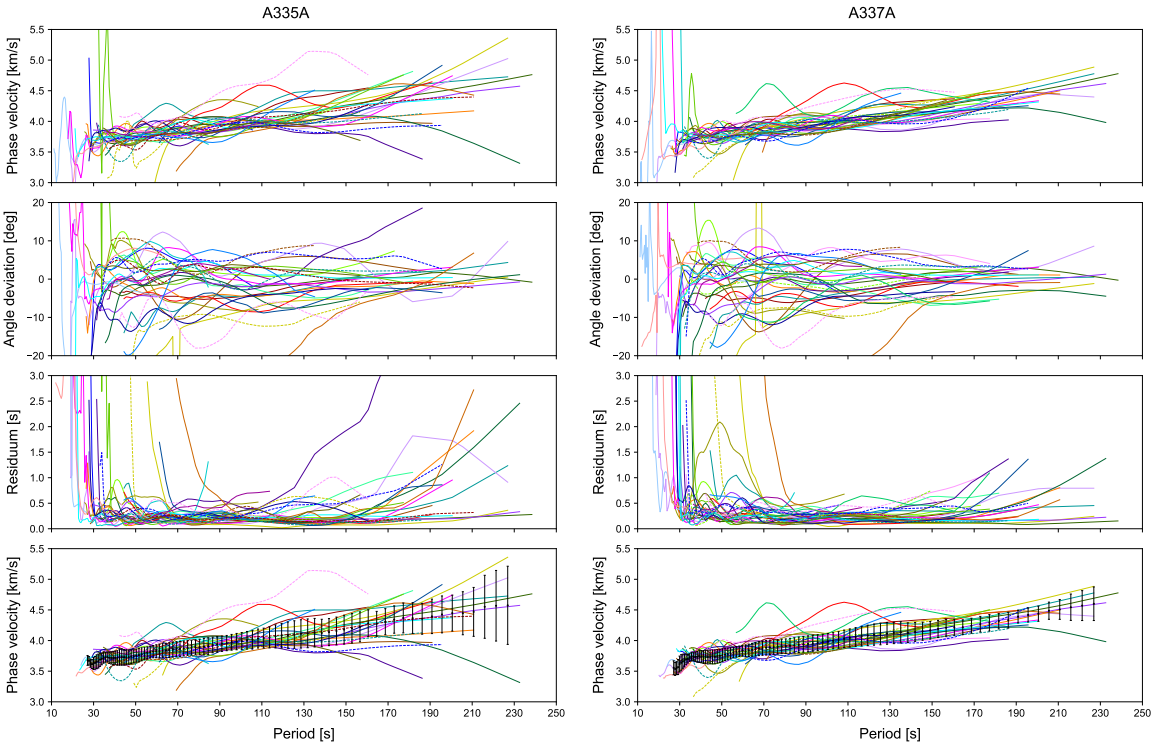
A335A
A337A
Phase velocity [km/s]
Angle deviation [deg]
Residuum [s]
Phase velocity [km/s]
Period [s]

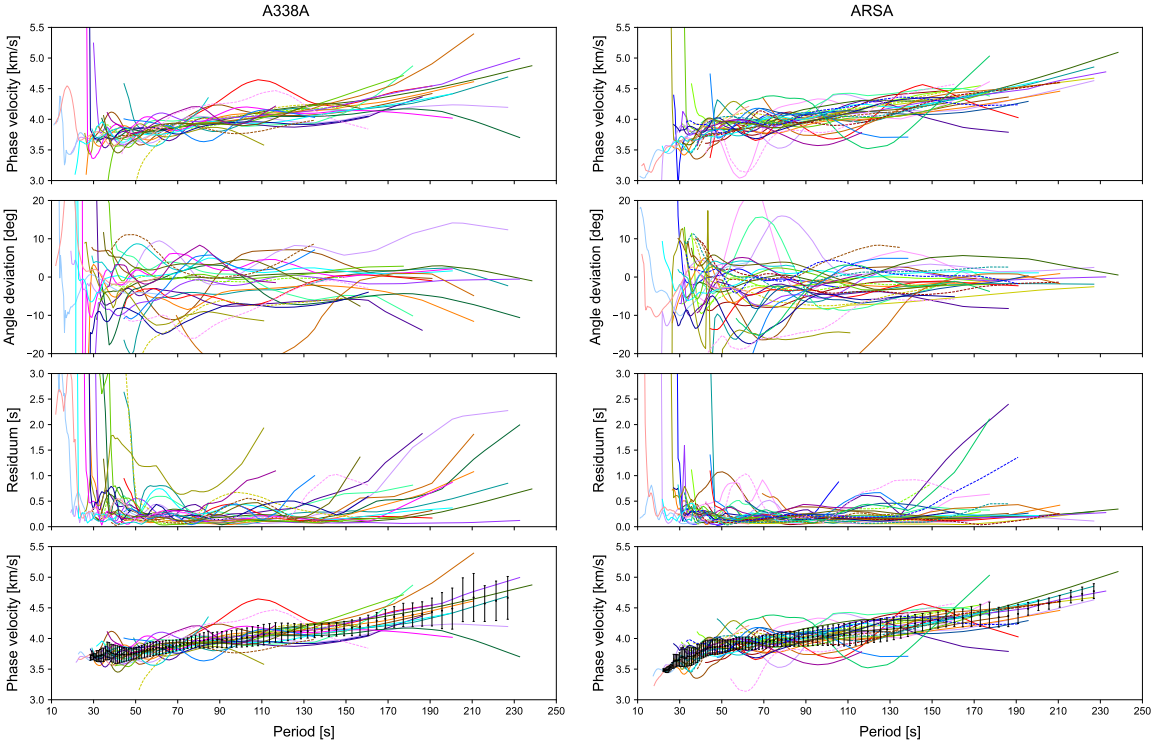
A338A
ARSA
Phase velocity [km/s]
Angle deviation [deg]
Residuum [s]
Phase velocity [km/s]
Period [s]

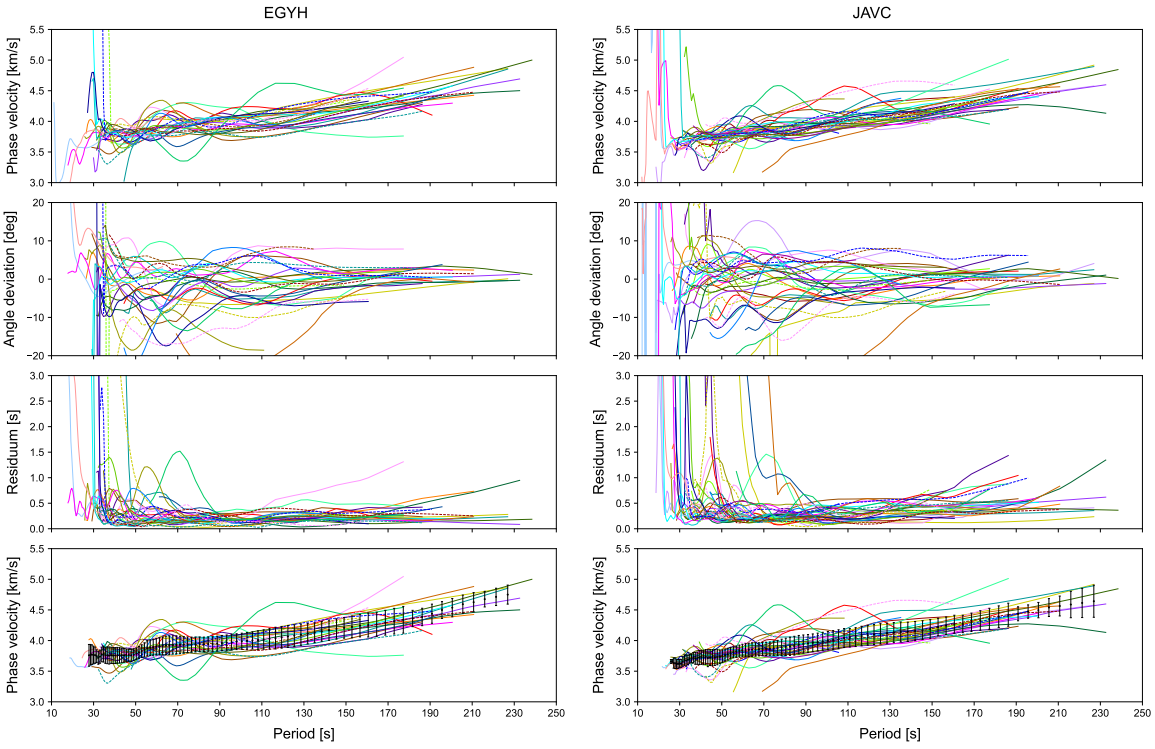
EGYH
JAVC
Phase velocity [km/s]
Angle deviation [deg]
Residuum [s]
Phase velocity [km/s]
Period [s]

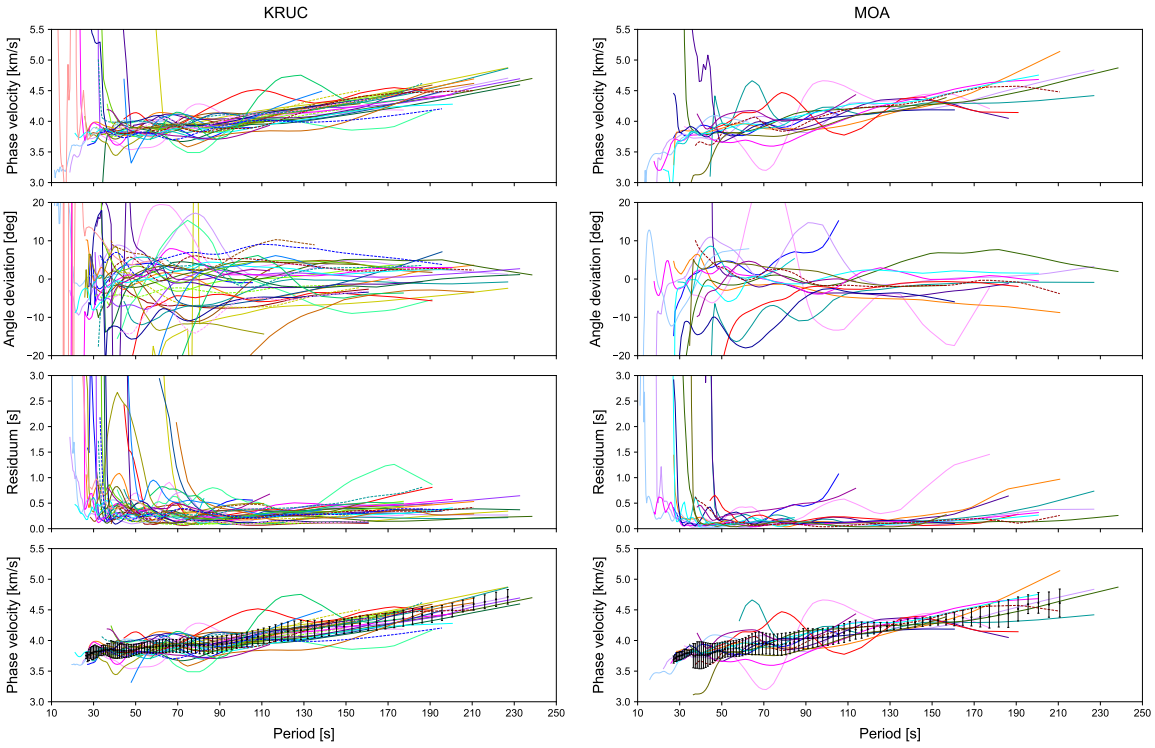
KRUC
MOA
Phase velocity [km/s]
Angle deviation [deg]
Residuum [s]
Phase velocity [km/s]
Period [s]

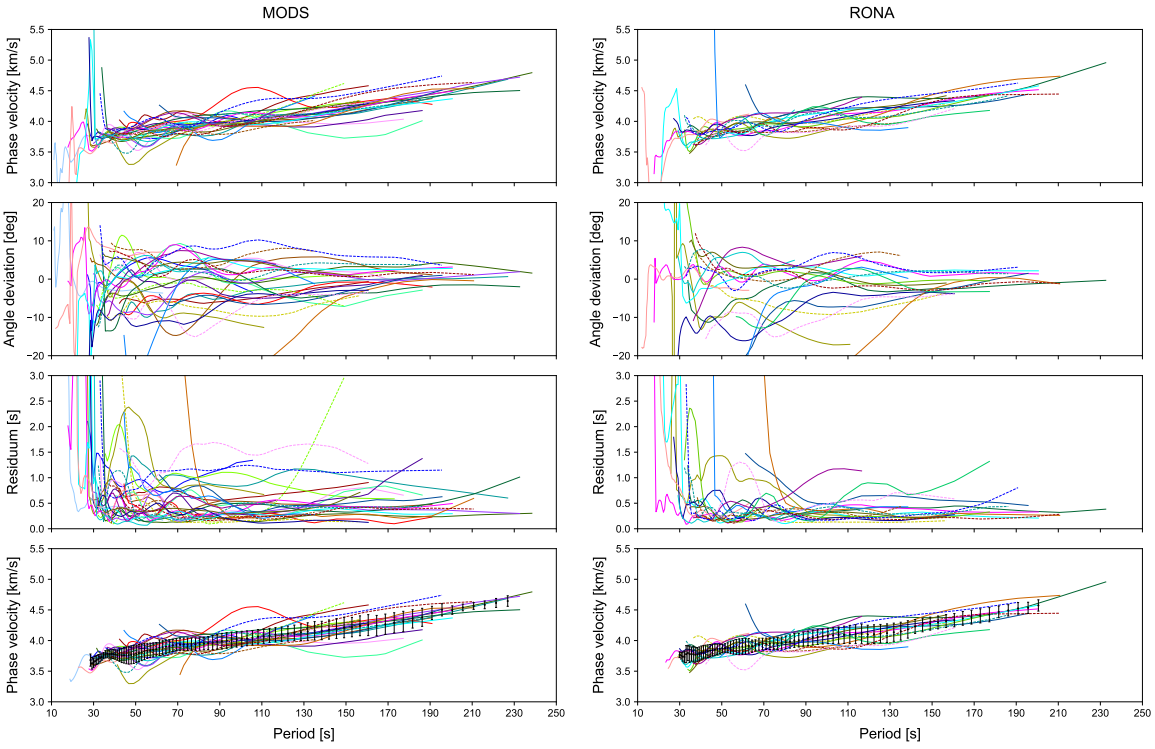
MODS
RONA
Phase velocity [km/s]
Angle deviation [deg]
Residuum [s]
Phase velocity [km/s]
Period [s]

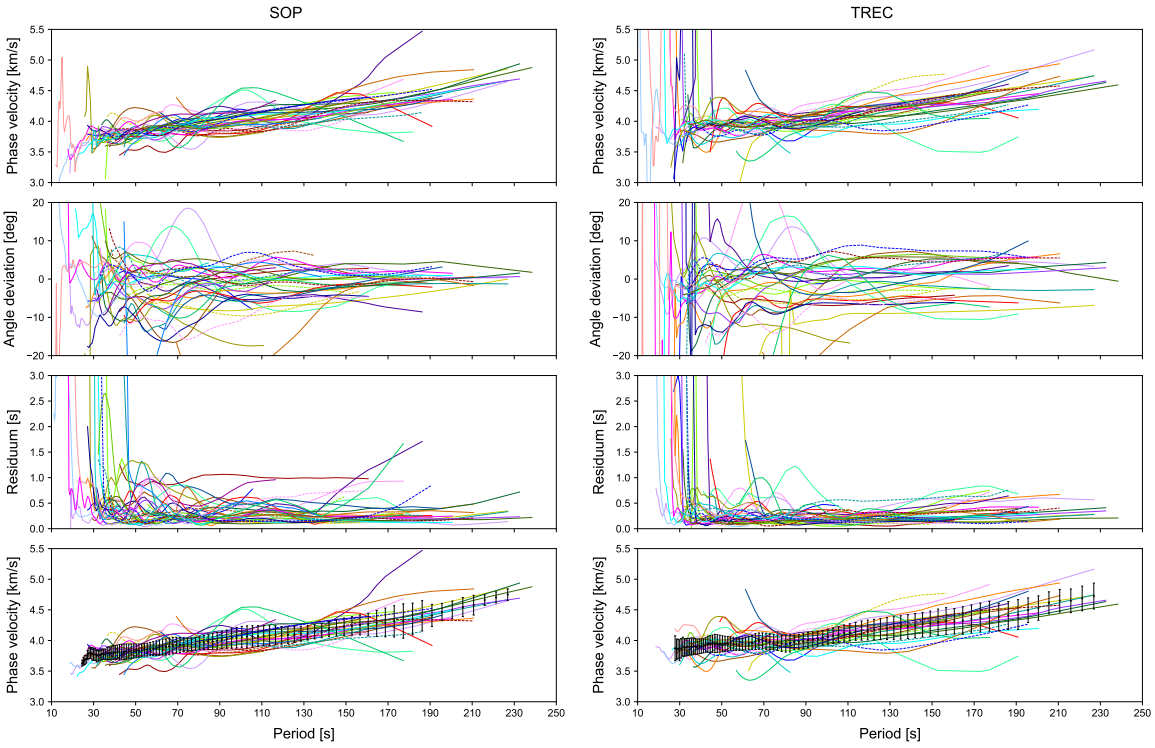
SOP
TREC
Phase velocity [km/s]
Angle deviation [deg]
Residuum [s]
Phase velocity [km/s]
Period [s]

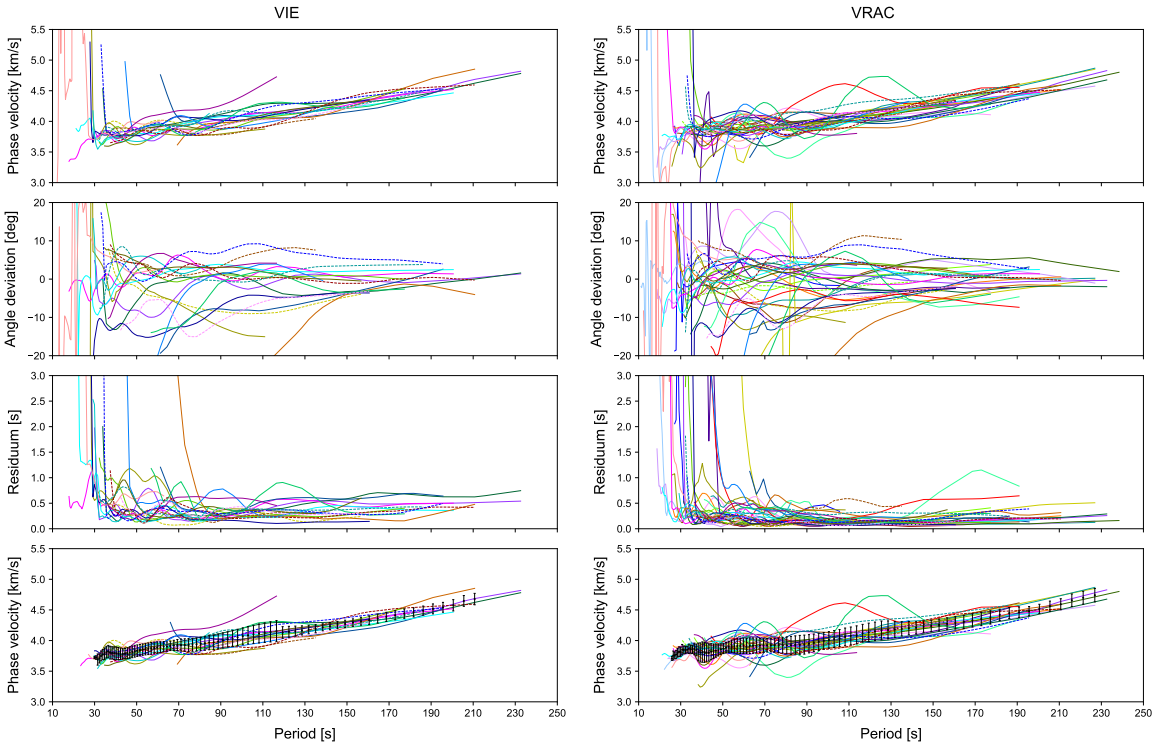

Figure A.36. Measured phase velocity dispersion curves for the rest 46 subarrays.

A.3 Shear-wave velocity at depth

I present the inversion results for all other 46 arrays. Subarrays CONA and A339A were displayed in Figure 18.

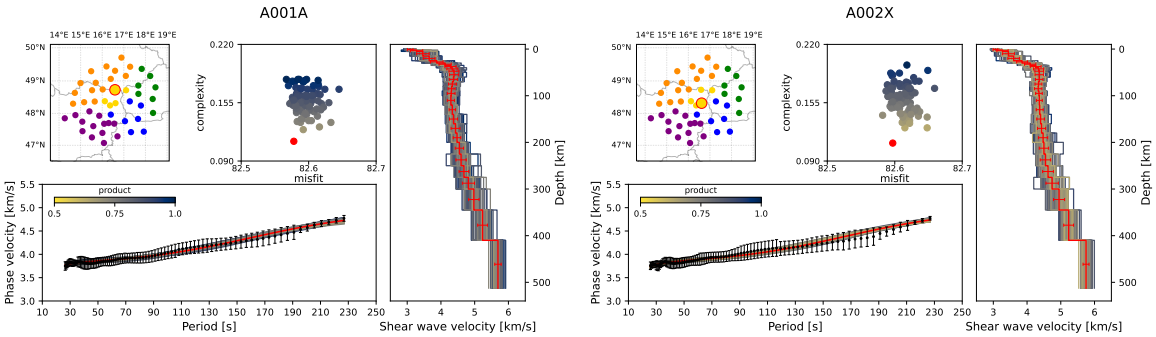

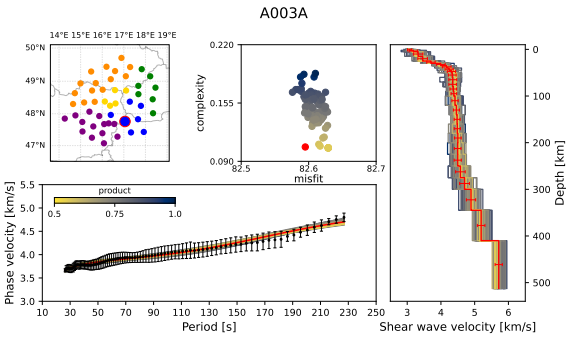
A003A
14°E 15°E 16°E 17°E 18°E 19°E
50°N
49°N
48°N
47°N
complexity
misfit
product
Phase velocity [km/s]
Period [s]
Shear wave velocity [km/s]
Depth [km]

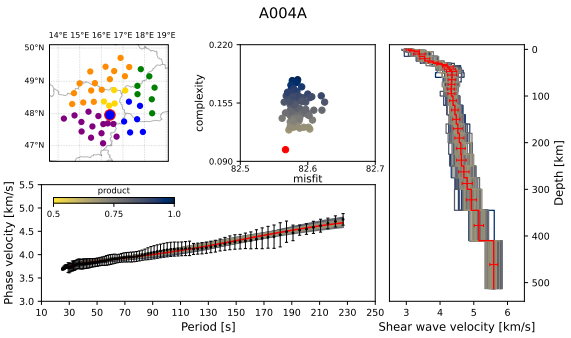
A004A
14°E 15°E 16°E 17°E 18°E 19°E
50°N
49°N
48°N
47°N
complexity
misfit
product
Phase velocity [km/s]
Period [s]
Shear wave velocity [km/s]
Depth [km]

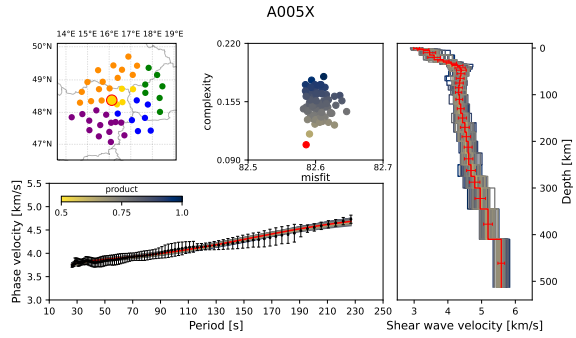
A005X
14°E 15°E 16°E 17°E 18°E 19°E
50°N
49°N
48°N
47°N
complexity
misfit
product
Phase velocity [km/s]
Period [s]
Shear wave velocity [km/s]
Depth [km]

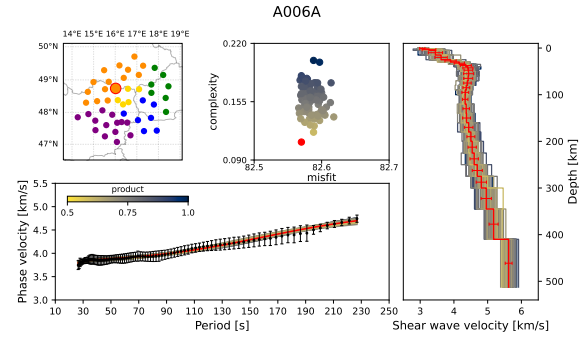
A006A
14°E 15°E 16°E 17°E 18°E 19°E
50°N
49°N
48°N
47°N
complexity
misfit
product
Phase velocity [km/s]
Period [s]
Shear wave velocity [km/s]
Depth [km]

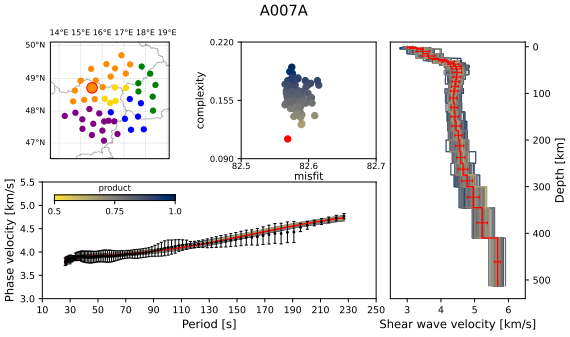
A007A
14°E 15°E 16°E 17°E 18°E 19°E
50°N
49°N
48°N
47°N
complexity
misfit
product
Phase velocity [km/s]
Period [s]
Shear wave velocity [km/s]
Depth [km]

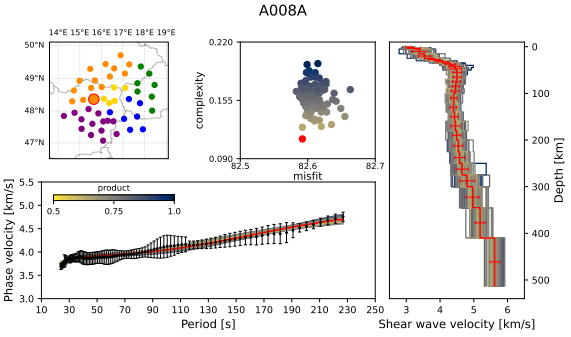
A008A
14°E 15°E 16°E 17°E 18°E 19°E
50°N
49°N
48°N
47°N
complexity
misfit
product
Phase velocity [km/s]
Period [s]
Shear wave velocity [km/s]
Depth [km]

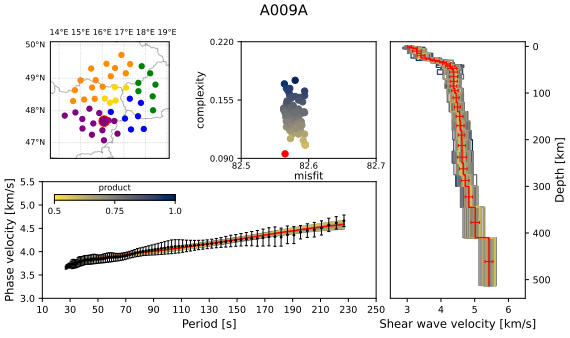
A009A
14°E 15°E 16°E 17°E 18°E 19°E
50°N
49°N
48°N
47°N
complexity
misfit
product
Phase velocity [km/s]
Period [s]
Shear wave velocity [km/s]
Depth [km]

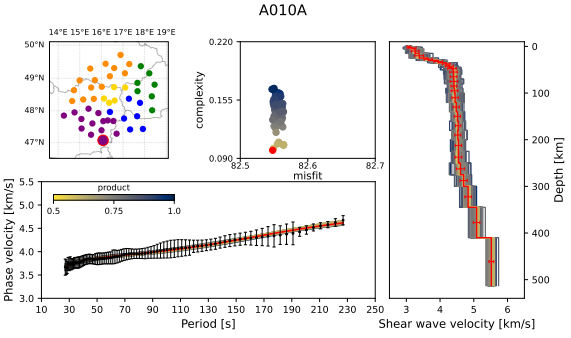
A010A
14°E 15°E 16°E 17°E 18°E 19°E
50°N
49°N
48°N
47°N
complexity
misfit
product
Phase velocity [km/s]
Period [s]
Shear wave velocity [km/s]
Depth [km]

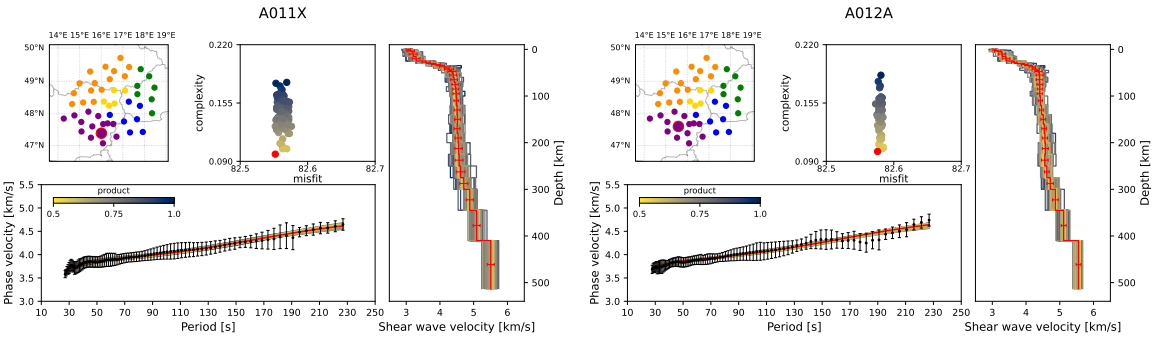
A011X
A012A
14°E 15°E 16°E 17°E 18°E 19°E
50°N
49°N
48°N
47°N
complexity
misfit
product
Phase velocity [km/s]
Period [s]
Shear wave velocity [km/s]
Depth [km]

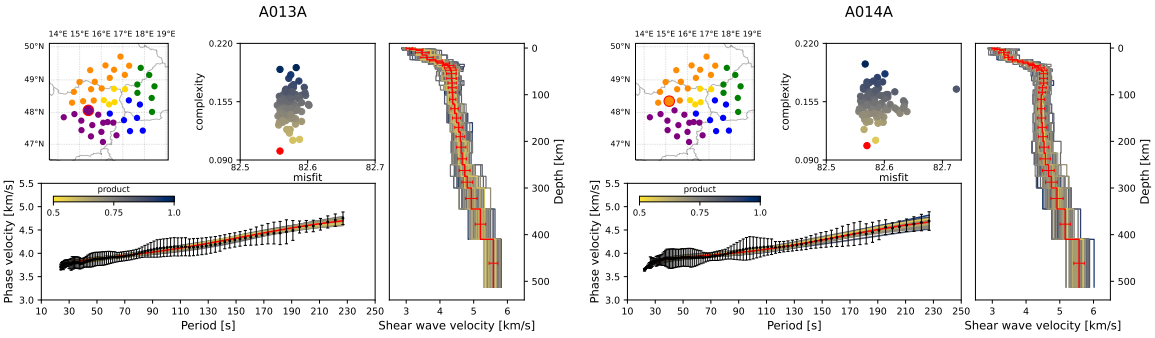
A013A
A014A
14°E 15°E 16°E 17°E 18°E 19°E
50°N
49°N
48°N
47°N
complexity
misfit
product
Phase velocity [km/s]
Period [s]
Shear wave velocity [km/s]
Depth [km]

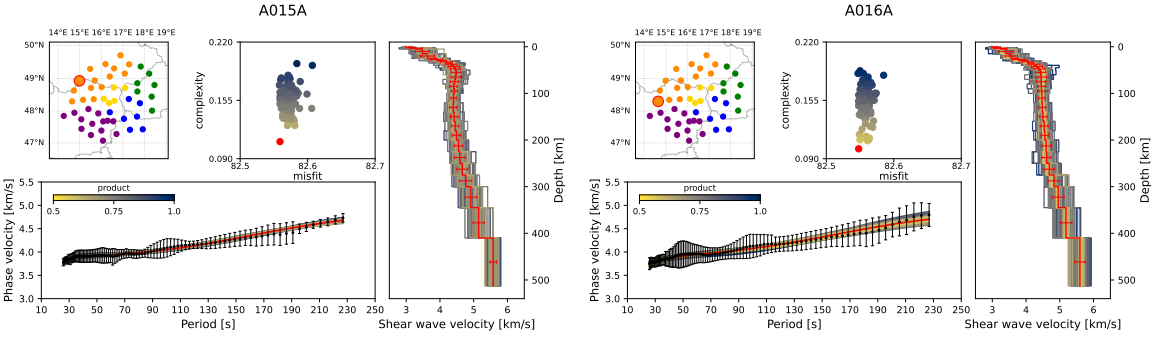
A015A
A016A
14°E 15°E 16°E 17°E 18°E 19°E
50°N
49°N
48°N
47°N
complexity
misfit
product
Phase velocity [km/s]
Period [s]
Shear wave velocity [km/s]
Depth [km]

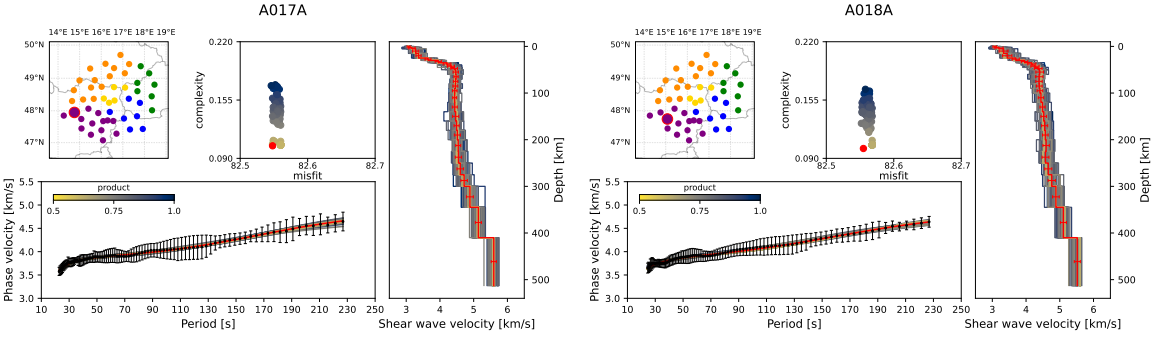
A017A
A018A
14°E 15°E 16°E 17°E 18°E 19°E
50°N
49°N
48°N
47°N
complexity
misfit
product
Phase velocity [km/s]
Period [s]
Shear wave velocity [km/s]
Depth [km]

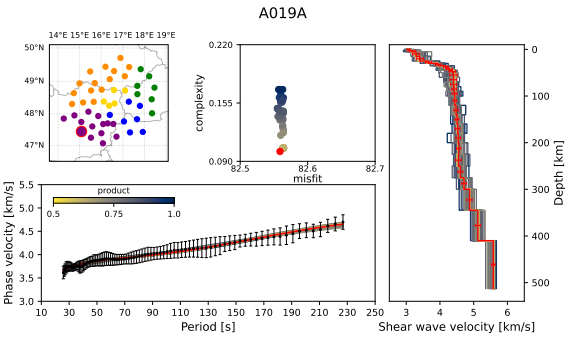
A019A
14°E 15°E 16°E 17°E 18°E 19°E
50°N
49°N
48°N
47°N
complexity
misfit
product
Phase velocity [km/s]
Period [s]
Shear wave velocity [km/s]
Depth [km]

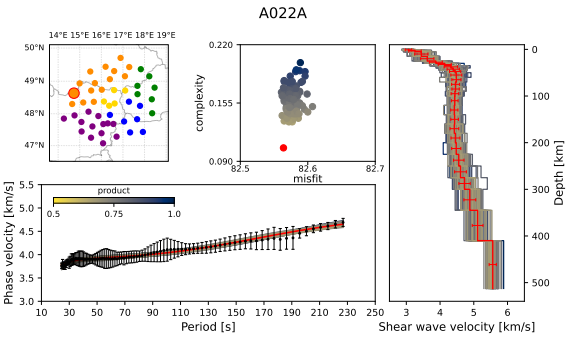
A022A
14°E 15°E 16°E 17°E 18°E 19°E
50°N
49°N
48°N
47°N
complexity
misfit
product
Phase velocity [km/s]
Period [s]
Shear wave velocity [km/s]
Depth [km]

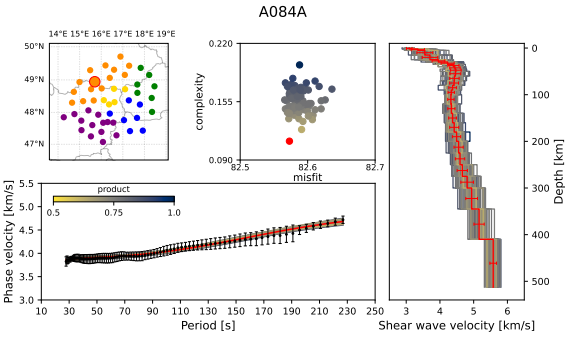
A084A
14°E 15°E 16°E 17°E 18°E 19°E
50°N
49°N
48°N
47°N
complexity
misfit
product
Phase velocity [km/s]
Period [s]
Shear wave velocity [km/s]
Depth [km]

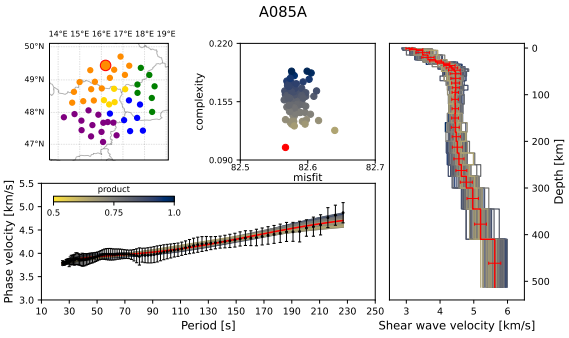
A085A
14°E 15°E 16°E 17°E 18°E 19°E
50°N
49°N
48°N
47°N
complexity
misfit
product
Phase velocity [km/s]
Period [s]
Shear wave velocity [km/s]
Depth [km]

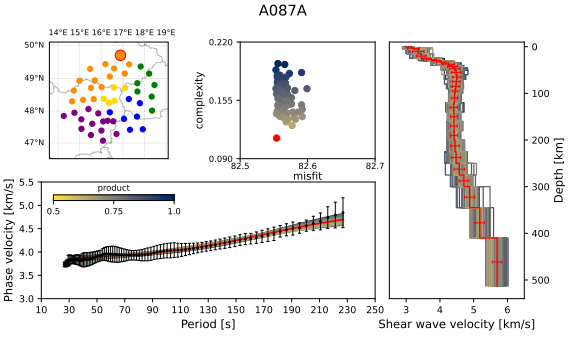
A087A
14°E 15°E 16°E 17°E 18°E 19°E
50°N
49°N
48°N
47°N
complexity
misfit
product
Phase velocity [km/s]
Period [s]
Shear wave velocity [km/s]
Depth [km]

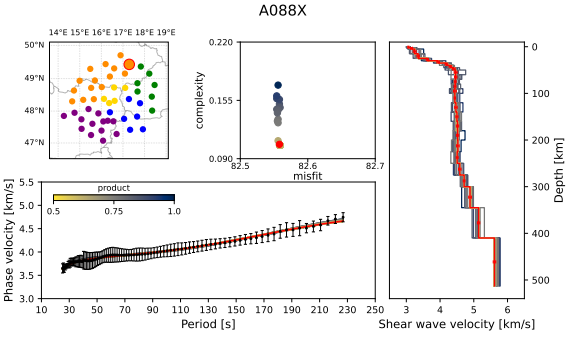
A088X
14°E 15°E 16°E 17°E 18°E 19°E
50°N
49°N
48°N
47°N
complexity
misfit
product
Phase velocity [km/s]
Period [s]
Shear wave velocity [km/s]
Depth [km]

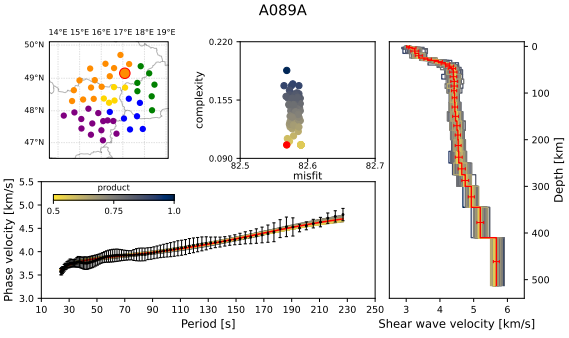
A089A
14°E 15°E 16°E 17°E 18°E 19°E
50°N
49°N
48°N
47°N
complexity
misfit
product
Phase velocity [km/s]
Period [s]
Shear wave velocity [km/s]
Depth [km]

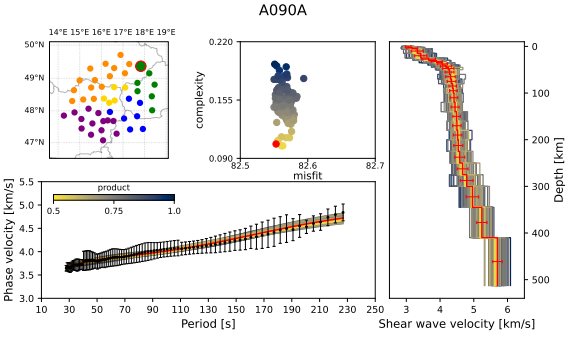
A090A
14°E 15°E 16°E 17°E 18°E 19°E
50°N
49°N
48°N
47°N
complexity
misfit
product
Phase velocity [km/s]
Period [s]
Shear wave velocity [km/s]
Depth [km]

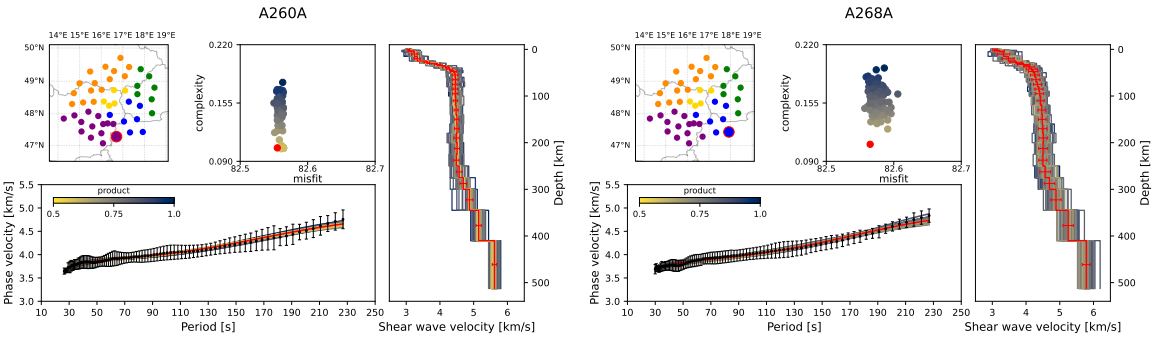
A260A
A268A
14°E 15°E 16°E 17°E 18°E 19°E
50°N
49°N
48°N
47°N
complexity
misfit
product
Phase velocity [km/s]
Period [s]
Shear wave velocity [km/s]
Depth [km]

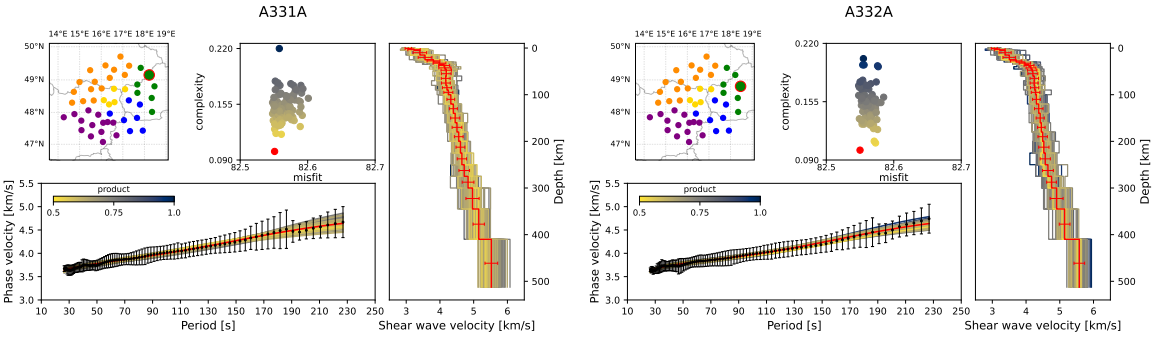
A331A
A332A
14°E 15°E 16°E 17°E 18°E 19°E
50°N
49°N
48°N
47°N
complexity
misfit
product
Phase velocity [km/s]
Period [s]
Shear wave velocity [km/s]
Depth [km]

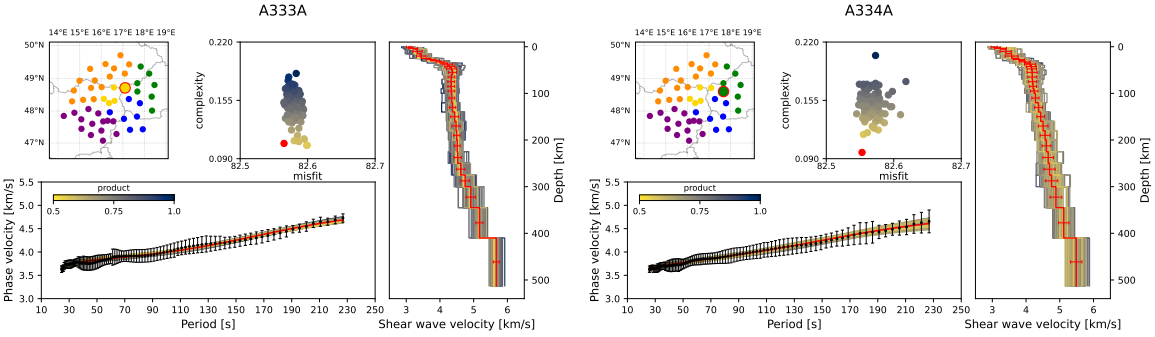
A333A
A334A
14°E 15°E 16°E 17°E 18°E 19°E
50°N
49°N
48°N
47°N
complexity
misfit
product
Phase velocity [km/s]
Period [s]
Shear wave velocity [km/s]
Depth [km]

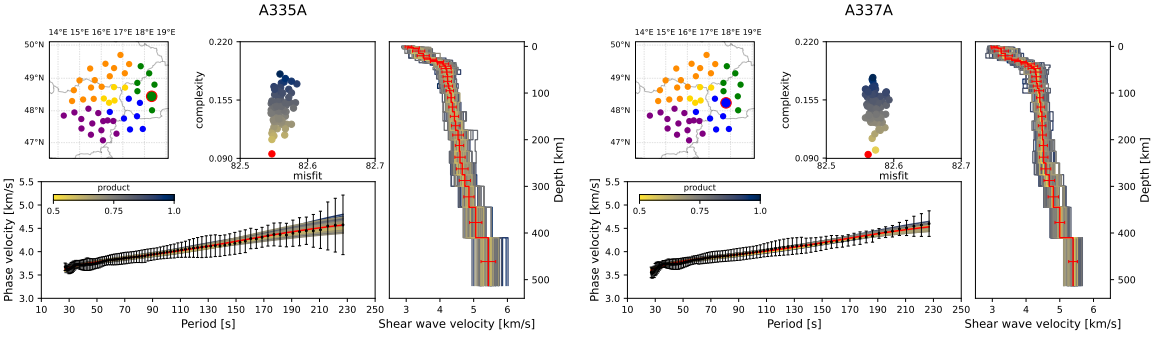
A335A
A337A
14°E 15°E 16°E 17°E 18°E 19°E
50°N
49°N
48°N
47°N
complexity
misfit
product
Phase velocity [km/s]
Period [s]
Shear wave velocity [km/s]
Depth [km]

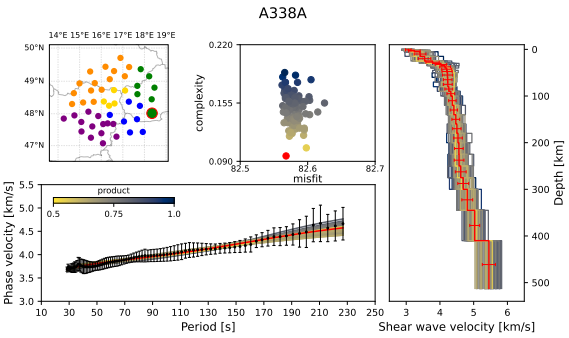
A338A
14°E 15°E 16°E 17°E 18°E 19°E
50°N
49°N
48°N
47°N
complexity
misfit
product
Phase velocity [km/s]
Period [s]
Shear wave velocity [km/s]
Depth [km]

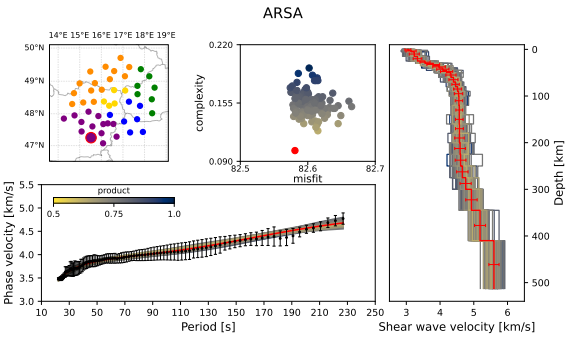
ARSA
14°E 15°E 16°E 17°E 18°E 19°E
50°N
49°N
48°N
47°N
complexity
misfit
product
Phase velocity [km/s]
Period [s]
Shear wave velocity [km/s]
Depth [km]

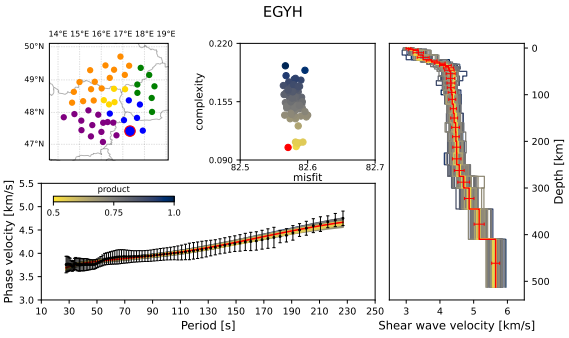
EGYH
14°E 15°E 16°E 17°E 18°E 19°E
50°N
49°N
48°N
47°N
complexity
misfit
product
Phase velocity [km/s]
Period [s]
Shear wave velocity [km/s]
Depth [km]

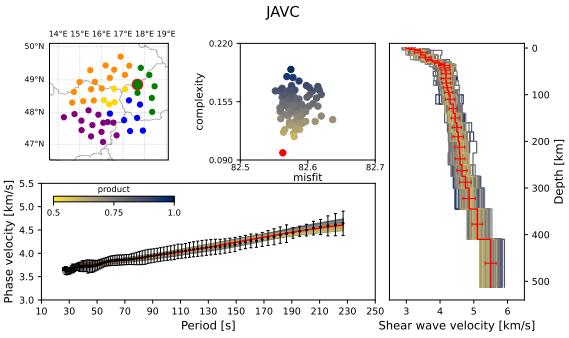
JAVC
14°E 15°E 16°E 17°E 18°E 19°E
50°N
49°N
48°N
47°N
complexity
misfit
product
Phase velocity [km/s]
Period [s]
Shear wave velocity [km/s]
Depth [km]

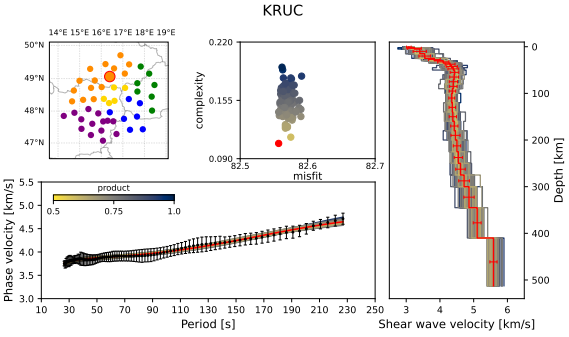
KRUC
14°E 15°E 16°E 17°E 18°E 19°E
50°N
49°N
48°N
47°N
complexity
misfit
product
Phase velocity [km/s]
Period [s]
Shear wave velocity [km/s]
Depth [km]

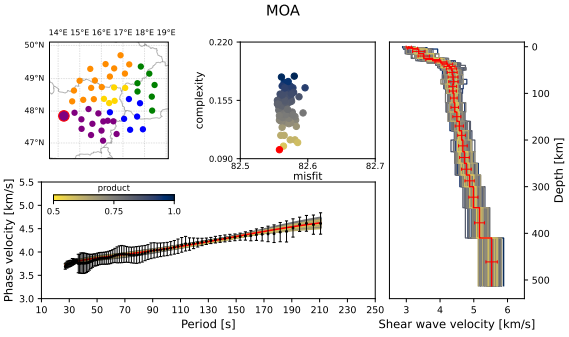
MOA
14°E 15°E 16°E 17°E 18°E 19°E
50°N
49°N
48°N
47°N
complexity
misfit
product
Phase velocity [km/s]
Period [s]
Shear wave velocity [km/s]
Depth [km]

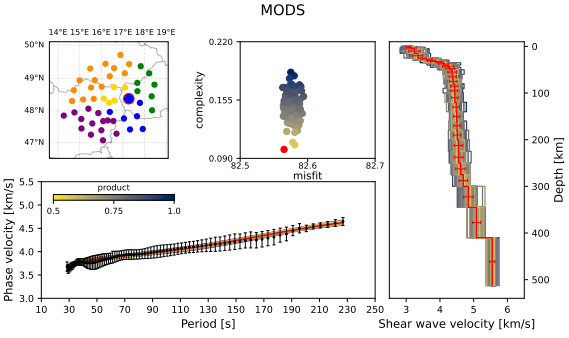
MODS
14°E 15°E 16°E 17°E 18°E 19°E
50°N
49°N
48°N
47°N
complexity
misfit
product
Phase velocity [km/s]
Period [s]
Shear wave velocity [km/s]
Depth [km]

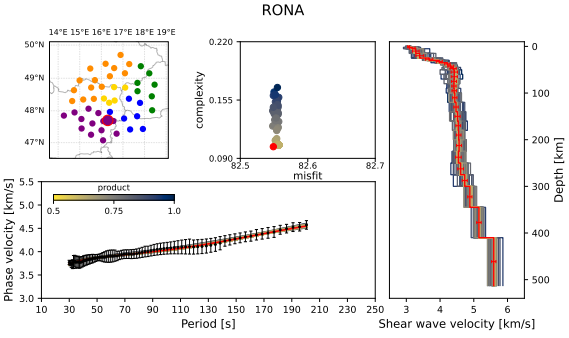
RONA
14°E 15°E 16°E 17°E 18°E 19°E
50°N
49°N
48°N
47°N
complexity
misfit
product
Phase velocity [km/s]
Period [s]
Shear wave velocity [km/s]
Depth [km]

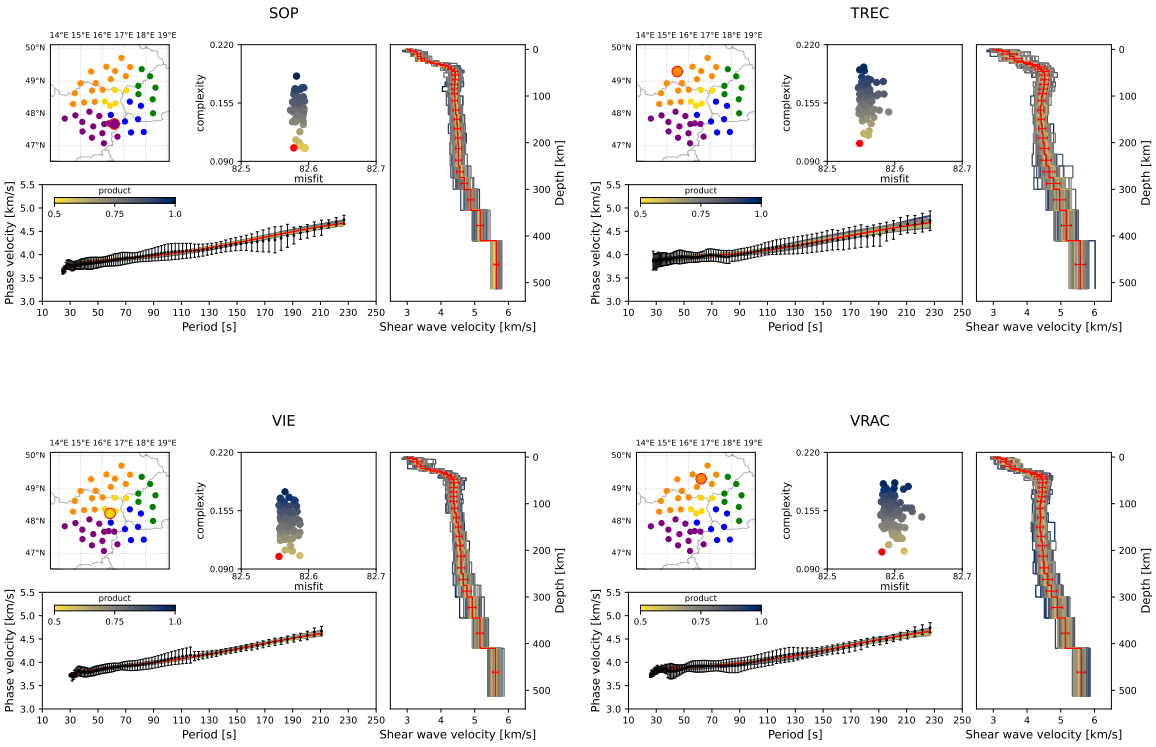

Figure A.37. Inversion results for the rest 46 subarrays.

A.4 Shear-wave velocity maps

Shear-wave velocity maps plotted using a relative scale for each depth were shown in Figure 19. Here, I present the same depth slices with a scale fixed for all layers showing the gradual increase in velocity with depth.

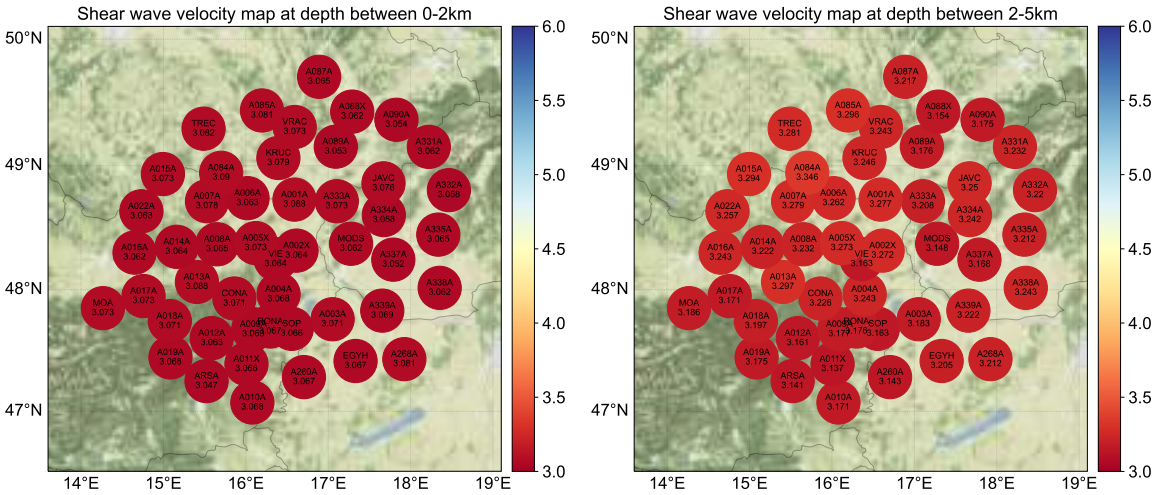

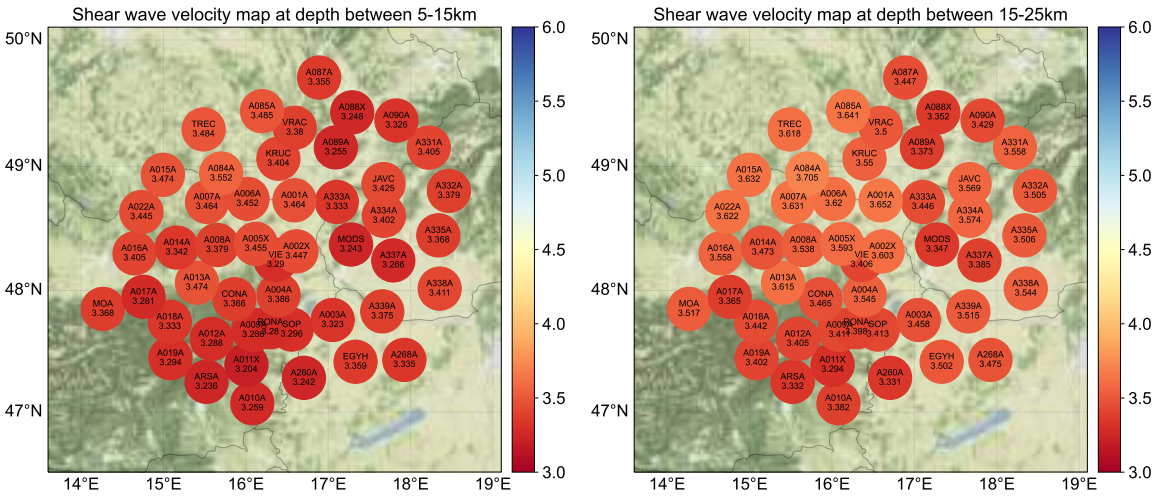
Shear wave velocity map at depth between 5-15km
50°N
49°N
48°N
47°N
14°E
15°E
16°E
17°E
18°E
19°E
6.0
5.5
5.0
4.5
4.0
3.5
3.0

Shear wave velocity map at depth between 15-25km
50°N
49°N
48°N
47°N
14°E
15°E
16°E
17°E
18°E
19°E
6.0
5.5
5.0
4.5
4.0
3.5
3.0

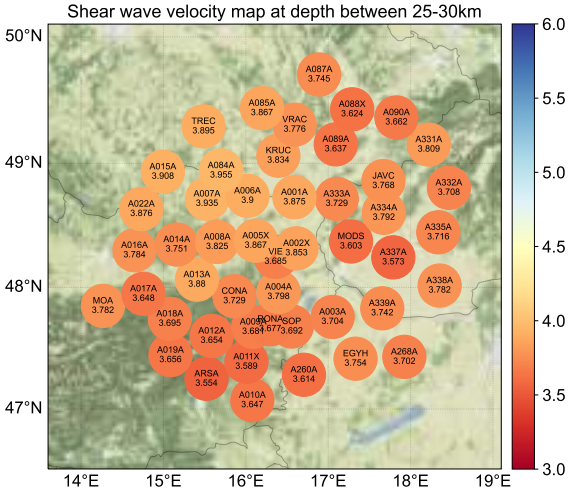
Shear wave velocity map at depth between 25-30km
50°N
49°N
48°N
47°N
14°E
15°E
16°E
17°E
18°E
19°E
6.0
5.5
5.0
4.5
4.0
3.5
3.0

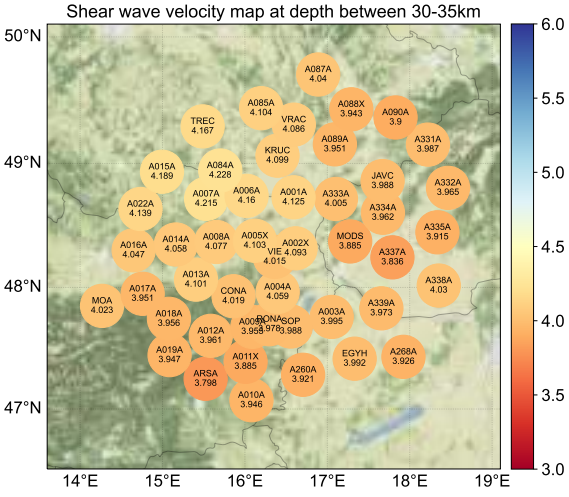
Shear wave velocity map at depth between 30-35km
50°N
49°N
48°N
47°N
14°E
15°E
16°E
17°E
18°E
19°E
6.0
5.5
5.0
4.5
4.0
3.5
3.0

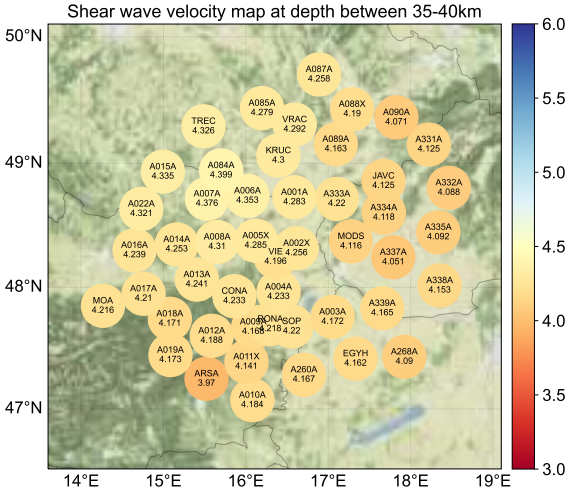
Shear wave velocity map at depth between 35-40km
50°N
49°N
48°N
47°N
14°E
15°E
16°E
17°E
18°E
19°E
6.0
5.5
5.0
4.5
4.0
3.5
3.0

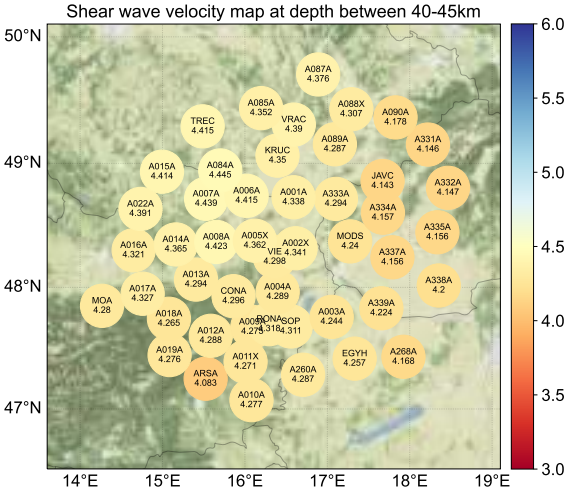
Shear wave velocity map at depth between 40-45km
50°N
49°N
48°N
47°N
14°E
15°E
16°E
17°E
18°E
19°E
6.0
5.5
5.0
4.5
4.0
3.5
3.0

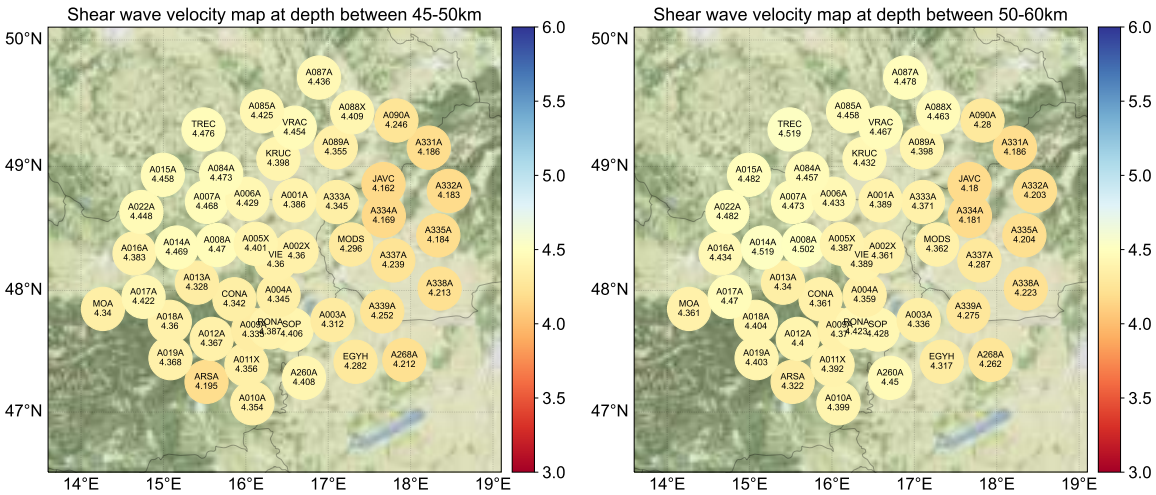
Shear wave velocity map at depth between 45-50km
50°N
49°N
48°N
47°N
14°E
15°E
16°E
17°E
18°E
19°E
6.0
5.5
5.0
4.5
4.0
3.5
3.0

Shear wave velocity map at depth between 50-60km
50°N
49°N
48°N
47°N
14°E
15°E
16°E
17°E
18°E
19°E
6.0
5.5
5.0
4.5
4.0
3.5
3.0

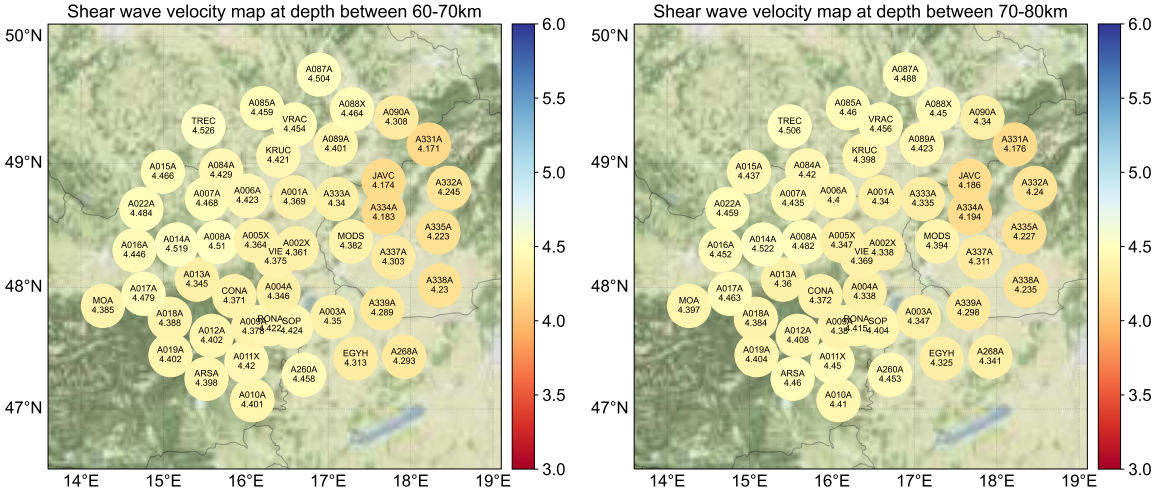
Shear wave velocity map at depth between 60-70km
50°N
49°N
48°N
47°N
14°E
15°E
16°E
17°E
18°E
19°E
6.0
5.5
5.0
4.5
4.0
3.5
3.0

Shear wave velocity map at depth between 70-80km
50°N
49°N
48°N
47°N
14°E
15°E
16°E
17°E
18°E
19°E
6.0
5.5
5.0
4.5
4.0
3.5
3.0

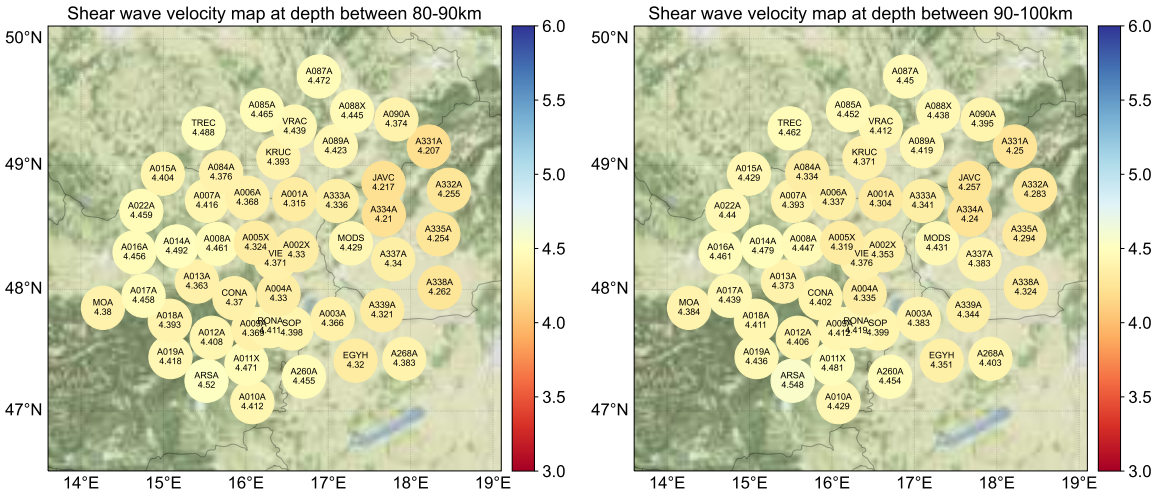
Shear wave velocity map at depth between 80-90km
50°N
49°N
48°N
47°N
14°E
15°E
16°E
17°E
18°E
19°E
6.0
5.5
5.0
4.5
4.0
3.5
3.0

Shear wave velocity map at depth between 90-100km
50°N
49°N
48°N
47°N
14°E
15°E
16°E
17°E
18°E
19°E
6.0
5.5
5.0
4.5
4.0
3.5
3.0

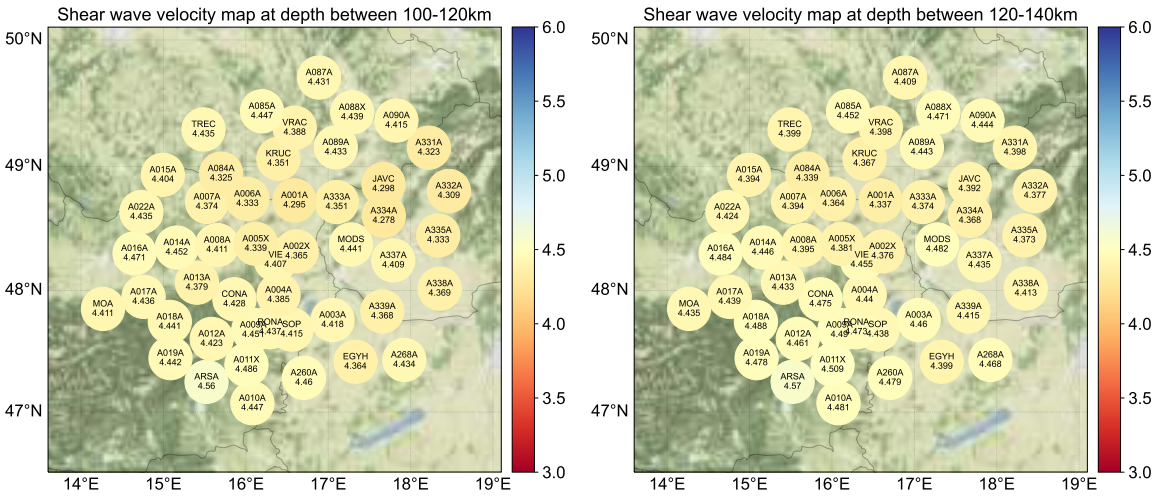
Shear wave velocity map at depth between 100-120km
50°N
49°N
48°N
47°N
14°E
15°E
16°E
17°E
18°E
19°E
6.0
5.5
5.0
4.5
4.0
3.5
3.0
A087A 4.431
A085A 4.447
A088X 4.439
A090A 4.415
TREC 4.435
VRAC 4.388
A331A 4.323
A089A 4.433
KRUC 4.351
A015A 4.404
A084A 4.325
JAVC 4.298
A332A 4.309
A007A 4.374
A006A 4.333
A001A 4.295
A333A 4.351
A334A 4.278
A022A 4.435
A335A 4.333
A016A 4.471
A014A 4.452
A008A 4.411
A005X 4.339
A002X 4.365
MODS 4.441
VIE 4.407
A337A 4.409
A013A 4.379
A338A 4.369
A017A 4.436
CONA 4.428
A004A 4.385
MOA 4.411
A018A 4.441
A003A 4.418
A339A 4.368
A009A 4.451
SONA 4.437
SOP 4.415
A012A 4.423
A019A 4.442
EGYH 4.364
A268A 4.434
A011X 4.486
ARSA 4.56
A260A 4.46
A010A 4.447

Shear wave velocity map at depth between 120-140km
50°N
49°N
48°N
47°N
14°E
15°E
16°E
17°E
18°E
19°E
6.0
5.5
5.0
4.5
4.0
3.5
3.0
A087A 4.409
A085A 4.452
A088X 4.471
A090A 4.444
TREC 4.399
VRAC 4.398
A331A 4.398
A089A 4.443
KRUC 4.367
A015A 4.394
A084A 4.339
JAVC 4.392
A332A 4.377
A007A 4.394
A006A 4.364
A001A 4.337
A333A 4.374
A334A 4.368
A022A 4.424
A335A 4.373
A016A 4.484
A014A 4.446
A008A 4.395
A005X 4.381
A002X 4.376
MODS 4.482
VIE 4.455
A337A 4.435
A013A 4.433
A338A 4.413
A017A 4.439
CONA 4.475
A004A 4.44
MOA 4.435
A018A 4.488
A003A 4.46
A339A 4.415
A009A 4.49
SONA 4.473
SOP 4.438
A012A 4.461
A019A 4.478
EGYH 4.399
A268A 4.468
A011X 4.509
ARSA 4.57
A260A 4.479
A010A 4.481

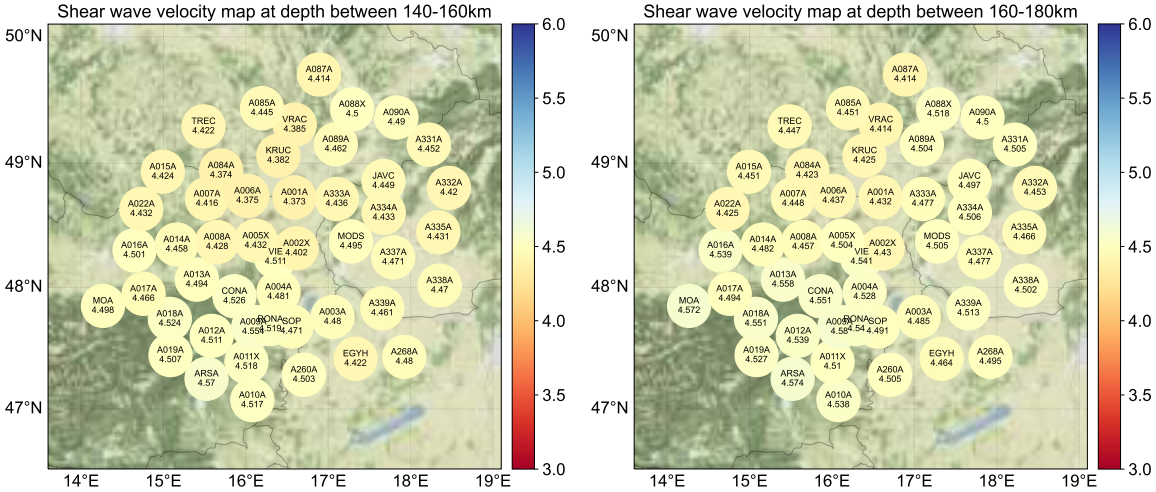
Shear wave velocity map at depth between 140-160km
50°N
49°N
48°N
47°N
14°E
15°E
16°E
17°E
18°E
19°E
6.0
5.5
5.0
4.5
4.0
3.5
3.0
A087A 4.414
A085A 4.445
A088X 4.5
A090A 4.49
TREC 4.422
VRAC 4.385
A331A 4.452
A089A 4.462
KRUC 4.382
A015A 4.424
A084A 4.374
JAVC 4.449
A332A 4.42
A007A 4.416
A006A 4.375
A001A 4.373
A333A 4.436
A334A 4.433
A022A 4.432
A335A 4.431
A016A 4.501
A014A 4.458
A008A 4.428
A005X 4.432
A002X 4.402
MODS 4.495
VIE 4.511
A337A 4.471
A013A 4.494
A338A 4.47
A017A 4.466
CONA 4.526
A004A 4.481
MOA 4.498
A018A 4.524
A003A 4.48
A339A 4.461
A009A 4.554
SONA 4.519
SOP 4.471
A012A 4.511
A019A 4.507
EGYH 4.422
A268A 4.48
A011X 4.518
ARSA 4.57
A260A 4.503
A010A 4.517

Shear wave velocity map at depth between 160-180km
50°N
49°N
48°N
47°N
14°E
15°E
16°E
17°E
18°E
19°E
6.0
5.5
5.0
4.5
4.0
3.5
3.0
A087A 4.414
A085A 4.451
A088X 4.518
A090A 4.5
TREC 4.447
VRAC 4.414
A331A 4.505
A089A 4.504
KRUC 4.425
A015A 4.451
A084A 4.423
JAVC 4.497
A332A 4.453
A007A 4.448
A006A 4.437
A001A 4.432
A333A 4.477
A334A 4.506
A022A 4.425
A335A 4.466
A016A 4.539
A014A 4.482
A008A 4.457
A005X 4.504
A002X 4.43
MODS 4.505
VIE 4.541
A337A 4.477
A013A 4.558
A338A 4.502
A017A 4.494
CONA 4.551
A004A 4.528
MOA 4.572
A018A 4.551
A003A 4.485
A339A 4.513
A009A 4.58
SONA 4.54
SOP 4.491
A012A 4.539
A019A 4.527
EGYH 4.464
A268A 4.495
A011X 4.51
ARSA 4.574
A260A 4.505
A010A 4.538

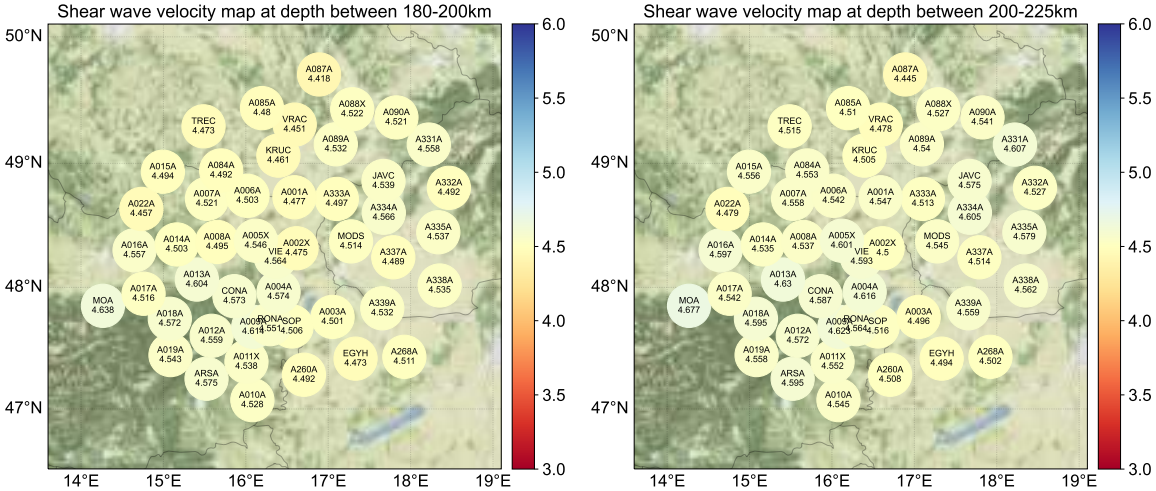
Shear wave velocity map at depth between 180-200km
50°N
49°N
48°N
47°N
14°E
15°E
16°E
17°E
18°E
19°E
6.0
5.5
5.0
4.5
4.0
3.5
3.0
A087A 4.418
A085A 4.48
A088X 4.522
A090A 4.521
TREC 4.473
VRAC 4.451
A331A 4.558
A089A 4.532
KRUC 4.461
A015A 4.494
A084A 4.492
JAVC 4.539
A332A 4.492
A007A 4.521
A006A 4.503
A001A 4.477
A333A 4.497
A334A 4.566
A022A 4.457
A335A 4.537
A016A 4.557
A014A 4.503
A008A 4.495
A005X 4.546
A002X 4.475
MODS 4.514
VIE 4.564
A337A 4.489
A013A 4.604
A338A 4.535
A017A 4.516
CONA 4.573
A004A 4.574
MOA 4.638
A018A 4.572
A003A 4.501
A339A 4.532
A009A 4.614
SONA 4.551
SOP 4.506
A012A 4.559
A019A 4.543
EGYH 4.473
A268A 4.511
A011X 4.538
ARSA 4.575
A260A 4.492
A010A 4.528

Shear wave velocity map at depth between 200-225km
50°N
49°N
48°N
47°N
14°E
15°E
16°E
17°E
18°E
19°E
6.0
5.5
5.0
4.5
4.0
3.5
3.0
A087A 4.445
A085A 4.51
A088X 4.527
A090A 4.541
TREC 4.515
VRAC 4.478
A331A 4.607
A089A 4.54
KRUC 4.505
A015A 4.556
A084A 4.553
JAVC 4.575
A332A 4.527
A007A 4.558
A006A 4.542
A001A 4.547
A333A 4.513
A334A 4.605
A022A 4.479
A335A 4.579
A016A 4.597
A014A 4.535
A008A 4.537
A005X 4.601
A002X 4.5
MODS 4.545
VIE 4.593
A337A 4.514
A013A 4.63
A338A 4.562
A017A 4.542
CONA 4.587
A004A 4.616
MOA 4.677
A018A 4.595
A003A 4.496
A339A 4.559
A009A 4.625
SONA 4.564
SOP 4.516
A012A 4.572
A019A 4.558
EGYH 4.494
A268A 4.502
A011X 4.552
ARSA 4.595
A260A 4.508
A010A 4.545

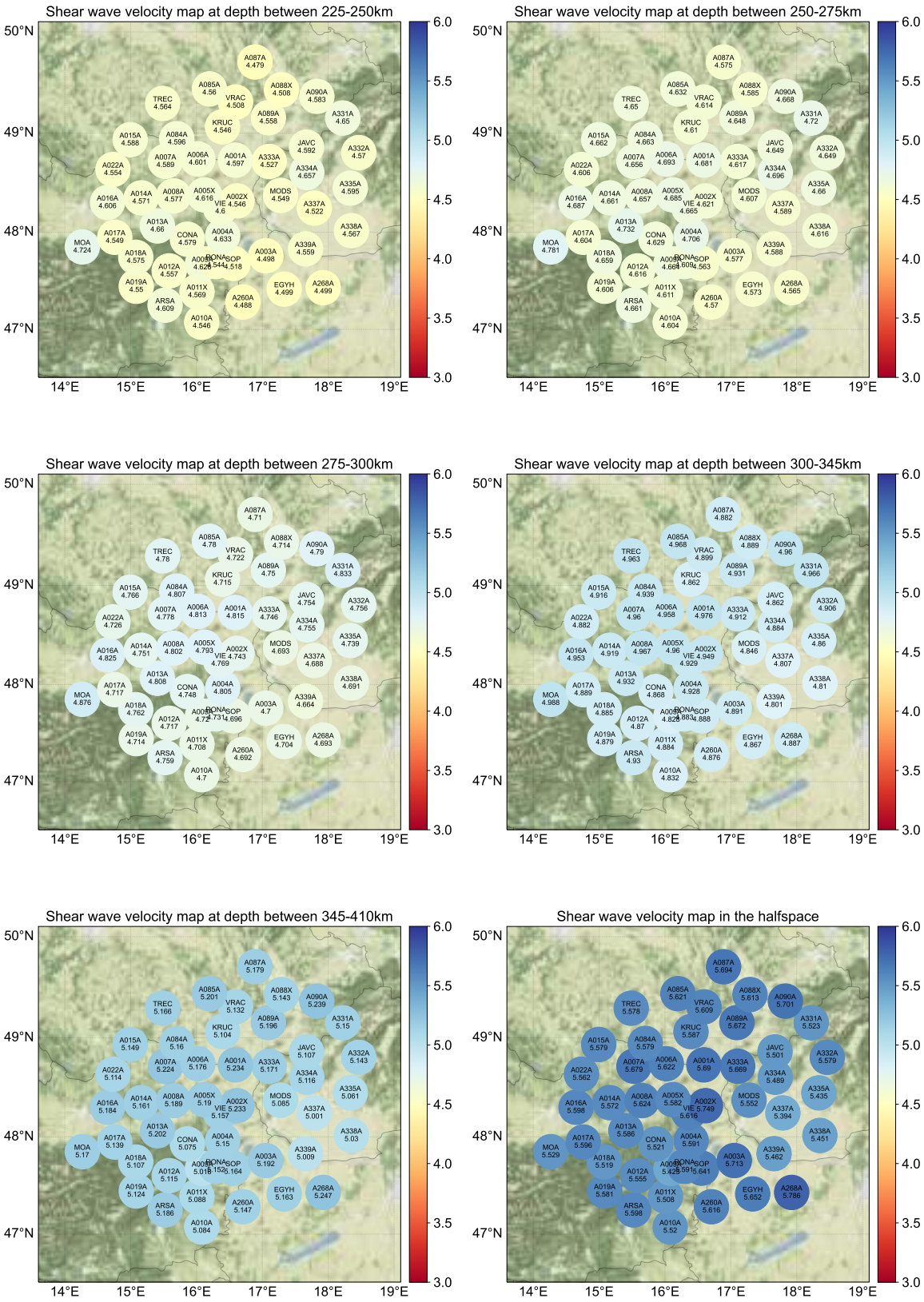

Figure A.38. Shear-wave velocity maps with fixed scale at all depths.

A.5 Acknowledgments to the AlpArray community

We acknowledge the operation of the Z3 - AlpArray Seismic Network 2015, see also Hetényi et al. 2018, and the permanent seismic networks used in this study: CZ - Institute Of Geophysics, A. O. S. O. T. C. R. 1973, HU - Kövesligethy Radó Seismological Observatory (Geodetic And Geophysical Institute, Research Centre For Astronomy And Earth Sciences, Hungarian Academy Of Sciences (MTA CSFK GGI KRSZO)) 1992, OE - ZAMG-Zentralanstalt Für Meterologie Und Geodynamik 1987,SK - ESI SAS (Earth Science Institute Of The Slovak Academy Of Sciences) 2004. The data from the permanent networks can be freely accessed by the ORFEUS/EIDA (European Integrated Data Archive) repository. The data from the AlpArray temporary seismic stations (Z3) can be accessed the same way after being open to the AlpArray Working Group (1. April 2020) and to the general public (1. April 2022).

The authors would like to thank the AlpArray Seismic Network Team for the station maintenance and data collection: György HETÉNYI, Rafael ABREU, Ivo ALLEGRETTI, Maria-Theresia APOLONER, Coralie AUBERT, Simon BESANÇON, Maxime BÈS DE BERC, Götz BOKELMANN, Didier BRUNEL, Marco CAPELLO, Martina ČARMAN, Adriano CAVALIERE, Jérôme CHÈZE, Claudio CHIARABBA, John CLINTON, Glenn COUGOULAT, Wayne C. CRAWFORD, Luigia CRISTIANO, Tibor CZIFRA, Ezio D'ALEMA, Stefania DANESI, Romuald DANIEL, Anke DANNOWSKI, Iva DASOVIĆ, Anne DESCHAMPS, Jean-Xavier DESSA, Cécile DOUBRE, Sven EGDORF, ETHZ-SED Electronics Lab, Tomislav FIKET, Kasper FISCHER, Wolfgang FRIEDERICH, Florian FUCHS, Sigward FUNKE, Domenico GIARDINI, Aladino GOVONI, Zoltán GRÁCZER, Gidera GRÖSCHL, Stefan HEIMERS, Ben HEIT, Davorka HERAK, Marijan HERAK, Johann HUBER, Dejan JARIĆ, Petr JEDLIČKA, Yan JIA, Hélène JUND, Edi KISSLING, Stefan KLINGEN, Bernhard KLOTZ, Petr KOLÍNSKÝ, Heidrun KOPP, Michael KORN, Josef KOTEK, Lothar KÜHNE, Krešo KUK, Dietrich LANGE, Jürgen LOOS, Sara LOVATI, Deny MALENGROS, Lucia MARGHERITI, Christophe MARON, Xavier MARTIN, Marco MASSA, Francesco MAZZARINI, Thomas MEIER, Laurent MÉTRAL, Irene MOLINARI, Milena MORETTI, Anna NARDI, Jurij PAHOR, Anne PAUL, Catherine PÉQUEGNAT, Daniel PETERSEN, Damiano PESARESI, Davide PICCININI, Claudia PIROMALLO, Thomas PLENEFISCH, Jaroslava PLOMEROVÁ, Silvia PONDRELLI, Snježan PREVOLNIK, Roman RACINE, Marc RÉGNIER, Miriam REISS, Joachim RITTER, Georg RÜMPKER, Simone SALIMBENI, Marco SANTULIN, Werner SCHERER, Sven SCHIPPKUS, Detlef SCHULTE-KORTNACK, Vesna ŠIPKA, Stefano SOLARINO, Daniele SPALLAROSSA, Kathrin SPIEKER, Josip STIPČEVIĆ, Angelo STROLLO, Bálint SÜLE, Gyöngyvér SZANYI, Eszter SZŰCS, Christine THOMAS, Martin THORWART, Frederik TILMANN, Stefan UEDING, Massimiliano VALLOCCHIA, Luděk VECSEY, René VOIGT, Joachim WASSERMANN, Zoltán WÉBER, Christian WEIDLE, Viktor WESZTERGOM, Gauthier WEYLAND, Stefan WIEMER, Felix WOLF, David WOLYNIEC, Thomas ZIEKE, Mladen ŽIVČIĆ and Helena ŽLEBČÍKOVÁ.

Bibliography

Behm, M., N. Nakata, and G. Bokelmann (Aug. 2016). "Regional ambient noise tomography in the Eastern Alps of Europe". In: *Pure and Applied Geophysics* 173.8, pp. 2813–2840. ISSN: 1420-9136. DOI: 10.1007/s00024-016-1314-z.

Belinić, T., P. Kolínský, and J. Stipčević (2021). "Shear-wave velocity structure beneath the Dinarides from the inversion of Rayleigh-wave dispersion". In: *Earth and Planetary Science Letters* 555, p. 116686. ISSN: 0012-821X. DOI: https://doi.org/10.1016/j.epsl.2020.116686.

Bokelmann, G., E. Qorbani, and I. Bianchi (2013). "Seismic anisotropy and large-scale deformation of the Eastern Alps". In: *Earth and Planetary Science Letters* 383, pp. 1–6.

Cotte, N. and H. A. Pedersen (2002). "Sharp contrast in lithospheric structure across the Sorgenfrei–Tornquist Zone as inferred by Rayleigh wave analysis of TOR1 project data". In: *Tectonophysics* 360.1. Geophysical Investigations og the Trans-European Suture Zone II, pp. 75–88. ISSN: 0040-1951. DOI: https://doi.org/10.1016/S0040-1951(02)00348-7.

Cotte, N., H. A. Pedersen, M. Campillo, V. Farra, and Y. Cansi (Sept. 2000). "Off-great-circle propagation of intermediate-period surface waves observed on a dense array in the French Alps". In: *Geophysical Journal International* 142.3, pp. 825–840. ISSN: 0956-540X. DOI: 10.1046/j.1365-246x.2000.00187.x.

CZ - Institute Of Geophysics, A. O. S. O. T. C. R. (1973). "*Czech Regional Seismic Network*. International Federation of Digital Seismograph Networks". In: DOI: https://doi.org/10.7914/SN/CZ.

Dando, B. D. E., G. W. Stuart, G. A. Houseman, E. Hegedüs, E. Brückl, and S. Radovanović (July 2011). "Teleseismic tomography of the mantle in the Carpathian-Pannonian region of central Europe". In: *Geophysical Journal International* 186.1, pp. 11–31. ISSN: 0956-540X. DOI: 10.1111/j.1365-246X.2011.04998.x.

Foster, A., G. Ekström, and V. Hjörleifsdóttir (2014). "Arrival-angle anomalies across the USArray Transportable Array". In: *Earth and Planetary Science Letters* 402. Special issue on USArray science, pp. 58–68. ISSN: 0012-821X. DOI: https://doi.org/10.1016/j.epsl.2013.12.046.

Fuchs, F., P. Kolínský, G. Gröschl, M.-T. Apoloner, E. Qorbani, F. Schneider, and G. Bokelmann (2015). "Site selection for a countrywide temporary network in Austria: noise analysis and preliminary performance". In: *Advances in Geosciences* 41, pp. 25–33. DOI: 10.5194/adgeo-41-25-2015.

Fuchs, F., P. Kolínský, G. Gröschl, G. Bokelmann, and the AlpArray Working Group (2016). "AlpArray in Austria and Slovakia: technical realization, site description and noise characterization". In: *Advances in Geosciences* 43, pp. 1–13. DOI: 10.5194/adgeo-43-1-2016.

Hetényi, G., I. Molinari, J. Clinton, G. Bokelmann, I. Bondár, W. C. Crawford, J.-X. Dessa, C. Doubre, W. Friederich, F. Fuchs, et al. (2018). "The AlpArray Seismic Network: A large-scale European experiment to image the Alpine orogen". In: *Surveys in Geophysics*, pp. 1–25.

Hetényi, G., G. W. Stuart, G. A. Houseman, F. Horváth, E. Hegedűs, and E. Brückl (2009). "Anomalously deep mantle transition zone below Central Europe: Evidence of lithospheric instability". In: *Geophysical Research Letters* 36.21. DOI: https://doi.org/10.1029/2009GL040171.

HU - Kövesligethy Radó Seismological Observatory (Geodetic And Geophysical Institute, Research Centre For Astronomy And Earth Sciences, Hungarian Academy Of Sciences (MTA CSFK GGI KRSZO)) (1992). "*Hungarian National Seismological Network*. Deutsches GeoForschungsZentrum GFZ". In: DOI: https://doi.org/10.14470/UH028726.

Hua, Y., D. Zhao, and Y. Xu (2017). "P wave anisotropic tomography of the Alps". In: *Journal of Geophysical Research: Solid Earth* 122.6, pp. 4509–4528. DOI: 10.1002/2016JB013831.

Kästle, E. D., C. Rosenberg, L. Boschi, N. Bellahsen, T. Meier, and A. El-Sharkawy (Mar. 2020). "Slab break-offs in the Alpine subduction zone". In: *International Journal of Earth Sciences* 109.2, pp. 587–603. ISSN: 1437-3262. DOI: 10.1007/s00531-020-01821-z.

Kästle, E. D., A. El-Sharkawy, L. Boschi, T. Meier, C. Rosenberg, N. Bellahsen, L. Cristiano, and C. Weidle (2018). "Surface Wave Tomography of the Alps Using Ambient-Noise and Earthquake Phase Velocity Measurements". In: *Journal of Geophysical Research: Solid Earth* 123.2, pp. 1770–1792. DOI: 10.1002/2017JB014698.

Kissling, E. (1993). "Deep structure of the Alps—what do we really know?" In: *Physics of the Earth and Planetary Interiors* 79.1, pp. 87–112. ISSN: 0031-9201. DOI: https://doi.org/10.1016/0031-9201(93)90144-X.

Kissling, E., S. M. Schmid, R. Lippitsch, J. Ansorge, and B. Fügenschuh (2006). "Lithosphere structure and tectonic evolution of the Alpine arc: new evidence from high-resolution teleseismic tomography". In: *Geological Society, London, Memoirs* 32.1, pp. 129–145. ISSN: 0435-4052. DOI: 10.1144/GSL.MEM.2006.032.01.08.

Kolínský, P., G. Bokelmann, and the AlpArray Working Group (Feb. 2019). "Arrival angles of teleseismic fundamental mode Rayleigh waves across the AlpArray". In: *Geophysical Journal International* 218.1, pp. 115–144. ISSN: 0956-540X. DOI: 10.1093/gji/ggz081.

Kolínský, P., G. Bokelmann, and the AlpArray Working Group (Oct. 2020a). "On the wobbles of phase-velocity dispersion curves". In: *Geophysical Journal International* 224.3, pp. 1477–1504. ISSN: 0956-540X. DOI: 10.1093/gji/ggaa487.

Kolínský, P., J. Málek, and J. Brokešová (Jan. 2011). "Shear wave crustal velocity model of the Western Bohemian Massif from Love wave phase velocity dispersion". In: *Journal of Seismology* 15.1, pp. 81–104. ISSN: 1573-157X. DOI: 10.1007/s10950-010-9209-4.

Kolínský, P., F. M. Schneider, and G. Bokelmann (2020b). "Surface wave diffraction pattern recorded on AlpArray: Cameroon Volcanic Line case study". In: *Journal of Geophysical Research: Solid Earth* 125.7. e2019JB019102 2019JB019102, e2019JB019102. DOI: https://doi.org/10.1029/2019JB019102.

Kolínský, P., J. Valenta, and J. Málek (July 2014). "Velocity model of the Hronov-Poříčí Fault Zone from Rayleigh wave dispersion". In: *Journal of Seismology* 18.3, pp. 617–635. ISSN: 1573-157X. DOI: 10.1007/s10950-014-9433-4.

Lippitsch, R., E. Kissling, and J. Ansorge (2003). "Upper mantle structure beneath the Alpine orogen from high-resolution teleseismic tomography". In: *Journal of Geophysical Research: Solid Earth* 108.B8. DOI: 10.1029/2002JB002016.

Love, A. E. H. (1911). *Some problems of geodynamics, Cambridge University Press, Cambridge, 180 pp.*

Lyu, Ch., H. A. Pedersen, A. Paul, L. Zhao, S. Solarino, and CIFALPS Working Group (Apr. 2017). "Shear wave velocities in the upper mantle of the Western Alps: new constraints using array analysis of seismic surface waves". In: *Geophysical Journal International* 210.1, pp. 321–331. ISSN: 0956-540X. DOI: 10.1093/gji/ggx166.

Málek, J., B. Růžek, and P. Kolář (Oct. 2007). "Isometric method: Efficient tool for solving non-linear inverse problems". In: *Studia Geophysica et Geodaetica* 51.4, pp. 469–490. ISSN: 1573-1626. DOI: 10.1007/s11200-007-0028-1.

Maupin, V. (May 2011). "Upper-mantle structure in southern Norway from beamforming of Rayleigh wave data presenting multipathing". In: *Geophysical Journal International* 185.2, pp. 985–1002. ISSN: 0956-540X. DOI: 10.1111/j.1365-246X.2011.04989.x.

OE - ZAMG-Zentralanstalt Für Meterologie Und Geodynamik (1987). "*Austrian Seismic Network*. International Federation of Digital Seismograph Networks". In: DOI: https://doi.org/10.7914/SN/OE.

Oldham, R. D. (1900). "On the propagation of earthquake motion to great distances". In: *Philosophical Transactions of the Royal Society of London. Series A, Containing Papers of a Mathematical or Physical Character* 194.252-261, pp. 135–174. DOI: 10.1098/rsta.1900.0015.

Pedersen, H. A., P. Boué, P. Poli, and A. Colombi (Oct. 2015). "Arrival angle anomalies of Rayleigh waves observed at a broadband array: a systematic study based on earthquake data, full waveform simulations and noise correlations". In: *Geophysical Journal International* 203.3, pp. 1626–1641. DOI: 10.1093/gji/ggv382.

Pedersen, H. A., O. Coutant, A. Deschamps, M. Soulage, and N. Cotte (Sept. 2003). "Measuring surface wave phase velocities beneath small broad-band arrays: tests of an improved algorithm and application to the French Alps". In: *Geophysical Journal International* 154.3, pp. 903–912. ISSN: 0956-540X. DOI: 10.1046/j.1365-246X.2003.02013.x.

Petrescu, L., S. Pondrelli, S. Salimbeni, M. Faccenda, and the AlpArray Working Group (June 2020a). "Mantle flow below the central and greater Alpine region: insights from SKS anisotropy analysis at AlpArray and permanent stations". In: *Solid Earth Discuss* 1.1, pp. 1009–1033.

Petrescu, L., G. Stuart, G. Houseman, and I. Bastow (Jan. 2020b). "Upper mantle deformation signatures of craton–orogen interaction in the Carpathian–Pannonian region from SKS anisotropy analysis". In: *Geophysical Journal International* 220.3, pp. 2105–2118.

Piromallo, C. and A. Morelli (2003). "P wave tomography of the mantle under the Alpine-Mediterranean area". In: *Journal of Geophysical Research: Solid Earth* 108.B2. DOI: https://doi.org/10.1029/2002JB001757.

Proskuryakova, T.A., O. Novotny, and E.V. Voronina (1981). *Studies of the Earth's structure by surface wave method (Central Europe)*.

Qorbani, E., I. Bianchi, and G. Bokelmann (2015). "Slab detachment under the Eastern Alps seen by seismic anisotropy". In: *Earth and Planetary Science Letters* 409, pp. 96–108.

Qorbani, E., G. Bokelmann, I. Kovács, F. Horváth, and G. Falus (2016). "Deformation in the asthenospheric mantle beneath the Carpathian-Pannonian Region". In: *Journal of Geophysical Research: Solid Earth* 121.9, pp. 6644–6657. DOI: 10.1002/2015JB012604.

Qorbani, E., D. Zigone, M. R. Handy, G. Bokelmann, and AlpArray-EASI working group (2020). "Crustal structures beneath the Eastern and Southern Alps from ambient noise tomography". In: *Solid Earth* 11.5, pp. 1947–1968. DOI: 10.5194/se-11-1947-2020.

Rayleigh, J. W. S. (1885). "On waves propagated along the plane surface of an elastic solid". In: *Proceedings of the London Mathematical Society* s1-17.1, pp. 4–11. DOI: https://doi.org/10.1112/plms/s1-17.1.4.

Schippkus, S., D. Zigone, G. Bokelmann, and the AlpArray Working Group (June 2018). "Ambient-noise tomography of the wider Vienna Basin region". In: *Geophysical Journal International* 215.1, pp. 102–117. ISSN: 0956-540X. DOI: 10.1093/gji/ggy259.

Schippkus, S., D. Zigone, G. Bokelmann, and AlpArray Working Group (Dec. 2020). "Azimuthal anisotropy in the wider Vienna basin region: a proxy for the present-day stress field and deformation". In: *Geophysical Journal International* 220.3, pp. 2056–2067. DOI: 10.1093/gji/ggz565.

Schivardi, R. and A. Morelli (Apr. 2011). "EPmantle: a 3-D transversely isotropic model of the upper mantle under the European Plate". In: *Geophysical Journal International* 185.1, pp. 469–484. ISSN: 0956-540X. DOI: 10.1111/j.1365-246X.2011.04953.x.

El-Sharkawy, A., T. Meier, S. Lebedev, J. H. Behrmann, M. Hamada, L. Cristiano, C. Weidle, and D. Köhn (2020). "The slab puzzle of the Alpine-Mediterranean region: Insights from a new, high-resolution, shear wave velocity model of the upper mantle". In: *Geochemistry, Geophysics, Geosystems* 21.8. e2020GC008993 10.1029/2020GC008993, e2020GC008993. DOI: https://doi.org/10.1029/2020GC008993.

SK - ESI SAS (Earth Science Institute Of The Slovak Academy Of Sciences) (2004). "*National Network of Seismic Stations of Slovakia*. Deutsches GeoForschungsZentrum GFZ". In: DOI: https://doi.org/10.14470/FX099882.

Soergel, D., H. A. Pedersen, L. Stehly, L. Margerin, A. Paul, and AlpArray Working Group (Oct. 2019). "Coda-Q in the 2.5–20 s period band from seismic noise: application to the greater Alpine area". In: *Geophysical Journal International* 220.1, pp. 202–217. ISSN: 0956-540X. DOI: 10.1093/gji/ggz443.

Szanyi, G., Z. Gráczer, B. Balázs, and I. J. Kovács (2021). "The transition zone between the Eastern Alps and the Pannonian basin imaged by ambient noise tomography". In: *Tectonophysics* 805, p. 228770. ISSN: 0040-1951. DOI: https://doi.org/10.1016/j.tecto.2021.228770.

Szanyi, G., Z. Gráczer, and E. Győri (June 2013). "Ambient seismic noise Rayleigh wave tomography for the Pannonian basin". In: *Acta Geodaetica et Geophysica* 48.2, pp. 209–220. ISSN: 2213-5820. DOI: 10.1007/s40328-013-0019-3.

Z3 - AlpArray Seismic Network (2015). "*AlpArray Seismic Network (AASN) temporary component*. AlpArray Working Group". In: DOI: https://doi.org/10.12686/alparray/z3_2015.

Zhao, L., A. Paul, M. G. Malusà, X. Xu, T. Zheng, S. Solarino, S. Guillot, S. Schwartz, T. Dumont, S. Salimbeni, C. Aubert, S. Pondrelli, Q. Wang, and R. Zhu (2016). "Continuity of the Alpine slab unraveled by high-resolution P wave tomography". In: *Journal of Geophysical Research: Solid Earth* 121.12, pp. 8720–8737. DOI: 10.1002/2016JB013310.